

Master Thesis Project

PIV Experimental Comparison of Vertical-Axis Wind Turbine Wake with Theoretical Models

Yugandhar Vijaykumar Patil



Delft University of Technology

Dedicated to - 

Poonam Vilasrao Patil

Vijaykumar Lalasao Patil

" ज्ञान ग्रहण करण्यासाठी आधी निसर्गाशी एकरूप होणं गरजेचं आहे. त्याचबरोबर स्वतः शी संवादही महत्त्वाचा, स्वतः शी केलेला संवाद हा ज्ञानाच्या कक्षा रुंदावत असतो. कोणतंही ज्ञान अंतिम नाही. चिकित्सक वृत्तीनं ज्ञानग्रहण केलं, तर जरासं ज्ञानही जीवनात प्रकाश बनून जीवन तेजोमय करतं "

 -दशग्रीवा 

Master Thesis Project

PIV Experimental Comparison of Vertical-Axis Wind Turbine Wake with Theoretical Models

by

Yugandhar Vijaykumar Patil

**In partial fulfillment of the requirements for the degree of Master of Science in Sustainable
Energy Technology at Delft University of Technology**

Student Number:	5122821
Professor supervisor:	Dr.ir. Carlos Simão Ferreira
PhD supervisor:	Ir.Ming Huang
Institution:	Delft University of Technology
Project Duration:	December, 2020 - November, 2021

**Faculty of Aerospace Engineering (AE) and Electrical Engineering, Mathematics, and
Computer Science (EEMCS) , Delft**

An electronic version of this thesis is available at <http://repository.tudelft.nl/>
Cover Image: Experimental campaign OJF May 18, 2021

Abstract

Vertical Axis Wind Turbine (VAWT) operation is characterized by complex and unsteady three-dimensional fluid dynamics, which presents considerable challenges. One of the crucial points to understand is the complex interaction between rotor, inflow, and wake systems. If we can demonstrate its effectiveness in the complex flow/inflow conditions, it will be of great importance.

To investigate the wake/wind aerodynamics, validate state-of-the-art VAWT wake models, a high-fidelity experimental measurement in the domain of VAWT wakes is needed. Computational fluid dynamics (CFD) models for complex wind interactions are far from being feasible. These models are highly time-consuming and computationally expensive, and their cost prohibits the simulation of complex flow configurations. This is usually overcome through the implementation of simple and computationally inexpensive analytical wake models, where the flow conditions are solved through simple analytical expressions and only over specific points of interest. The aim of the work is to realize and validate a simple and efficient analytical wake model (Abkar, 2019 [1]), (Bastankhah & Porté-Agel, 2014 [6]) for prediction of the wind velocity profile downwind of a VAWT turbine: The best by comparing the modeling results with a set of particle image velocimetry (PIV) measurements of the wakes of an in-house designed VAWT are used as a high-fidelity reference.

The present work evaluates and quantifies the influence of the wake deflection produced by the pitch angles of the blades on the scaled VAWT turbine. It reproduces the main phenomena involved in the flow pattern and identifies the general structure of the resulting wake that occurs: under the influence of pitching the blades on the upstream turbine. The configuration consists of a VAWT aligned in the direction of the incoming flow: With a class of cases for different configurations of the turbine are studied for example - deflection of wake through zero pitch, positive 10 degrees pitch, Negative 10 degrees pitch angles (Mendoza et al, 2019 [31]). The available power distribution over other hypothetical downwind turbines due to the influence of wake deflection by the upstream turbine is studied and reported. These interactions are measured with the help of large-scale PIV experiments in OJF, TU Delft. Also, an efficacious force balance system for the VAWT rotor is studied, designed, and fabricated (in-house) to calculate the accurate lift and drag forces on the VAWT structure.

The stereo particle image velocimetry results are compared with two theoretical works Jensen wake model, [20] and Gaussian-based wake model Abkar [1] and CFD simulations by Huang et al [17]. The study shows a wake shift towards the windward side (cross-flow width), Negative-Y direction. For all the pitch cases, maximum for the positive pitch angle and least for a negative pitch angle. The wake shift in the negative-Y direction can be caused by uneven distribution of forces on the rotor structure during rotation. The theoretical models especially the Gaussian-based wake model represent the wake deficit in close agreement to the experimental results but fails to account for wake shift and change in wake structure. The CFD simulations reproduce the 3D wake structures consistent with the experiment results but show an early recovery in the wake. The wake recovery with downwind available power is found higher with a positive pitch angle and least with the negative pitch. A study of in-plane velocity vectors indicates crosswind force introducing crosswind momentum to the flow and as a result would give rise to the CVPs, also according to a study by Rolin, F. Porté-Agel [37]. The theoretical models do not account for any of these structural changes in wake and the deflections in them. Furthermore, the suitability of these experimental references is used to verify the CFD simulations and analytical models range of the fidelity.

Acknowledgement

Going through this remarkable journey of my master thesis during the challenging times of the COVID-19 pandemic, tested my stamina. However, it gave me a sense of gratification and the realization of the passion for wind energy. This journey taught me many life lessons, that I would carry forward. The frame work of this beautiful thesis would not have been possible without the help and support of the people around me.

The person who deserves the most of my acknowledgment is Dr.ir. Carlos Simão Ferreira, whose understanding and flexibility made sure that the thesis came to a successful completion. I want to thank Ir. Ming Huang, who went through the same elegant framework when doing his own PhD. I want to emphasize on the fact that without him, it would not have been possible to accomplish the goals of this project. His help during the whole thesis and the experiment phase of thesis was priceless.

Moreover, this journey wouldn't have been possible without the emotional and financial support from my loving aai and baba, Poonam Vilasrao Patil, Vijaykumar Lalasao Patil whom I dedicate this master thesis to. I have been blessed with my sister Aishwarya Patil, and my brothers, Yashdeep Patil, Harshwrddhan Patil who loved and supported me through this remarkable journey of masters.

Furthermore, my gratitude extends to my friends who became my family, my lovely Eleftheria Givizini you supported, encouraged; and even witnessed the birth of this thesis, Arvind Sanjivan who sheltered me through my rough times, Rishikesh Joshi my go-to mentor and and my firm reason for masters, Niki-foros Paraskevopoulos who never let the stress of the thesis to creep into me, Sadhna Jagannathan for making me cheerful and happy in gloomy times. Ozal Yilmaz for his exceptional job of mentoring me and having a good laugh. You people provided me with resources so that my ideas would not be limited. You have changed my mind; you invested in me; you were patient and listened to me, receptive to what I was trying to teach you, and with that I learned so much. Thank you all for believing in me.

Last but not least, I wanna thank me, I wanna thank me for believing in me, I wanna thank me for doing all this hard work, I wanna thank me for, for never quitting, I wanna thank me for always being a giver and trying to give more than I receive, I wanna thank me for trying do more right than wrong, I wanna thank me for just being me at all times, I wanna thank me for going through all the tough and broke times and make it worth.

*Yugandhar Vijaykumar Patil
Delft, November 2021*

Contents

Abstract	i
Acknowledgement	ii
Nomenclature	v
List of Figures	vii
List of Tables	x
1 Introduction	1
1.1 Background	1
1.2 The motivation of the study	2
1.3 Aim and Hypothesis	2
1.4 Research Questions	3
1.5 Report Outline	4
2 Literature Review	5
2.1 Turbine Wake	5
2.1.1 Near Wakes	5
2.1.2 Far Wakes	5
2.2 State-of-the-art & historical development of turbine wake models	6
2.2.1 CFD Models	6
2.2.2 Field Models	6
2.2.3 Actuator line Model	6
2.2.4 Kinematic Models	6
2.2.5 Jensen	7
2.2.6 Frandsen Model	9
2.2.7 Jensen-Gaussian	10
2.2.8 Bastankhah and Porté-Agel Model	11
2.2.9 Self-Similar Gaussian Distribution for VAWT	14
2.3 A Survey on Simulating and Measuring the Wake of VAWTs	15
3 Experiment apparatus and setup	17
3.1 Open Jet Facility	17
3.2 Force Balance	18
3.2.1 Design	18
3.2.2 Fabrication and Assembly	19
3.2.3 Alignment and Installation	21
3.3 H-type Vertical Axis Wind Turbine	21
3.3.1 Design	22
3.3.2 Fabrication and Assembly	22
3.4 Particle Image Velocimetry	24
3.5 Experiment Setup	26
3.5.1 PIV Setup	27
3.6 Measurement Techniques	29
3.6.1 Force Balance	29
3.6.2 Data Acquisition System	30
3.6.3 Phase-locked Acquisition for Wake Synchronisation	30
3.6.4 Velocity Stream Measurements	32
3.7 Post-processing of the Time Averaged Wake Flow	33

4	Results, comparison, and discussion	35
4.1	Realisation of Theoretical Wake Models and CFD Simulations with Experimental Results	35
4.2	Experimental Validation of Wake Models and CFD simulations	43
4.3	Available Power for Hypothetical Downwind Turbines	64
5	Summary, Conclusions, and Future Work	67
5.1	Summary and Conclusion	67
5.2	Future Scope	68
	References	72
A	Appendix-A	73
A.1	Wake superposition Methods	73
A.1.1	Simple Empirical Wake Superposition Methods	73
A.1.2	Theoretical Wake Superposition Method based on Law of Conservation of Momentum	74
A.2	Determination of the Synchronisation System Delay	75
A.3	Experiment Planned Cases	76
A.4	Force measurement by Force Balance System for Pitch Angle Case	80
A.5	VAWT Cover Specifications	80
A.6	Blue Table Attachment Specifications	82
A.7	Guidance for Transverse System	83

Nomenclature

Abbreviations

Abbreviation	Definition
AC	Actuator Cylinder
AEP	Annual Energy Production
ALM	Actuator Line Model
VAWT	Vertical Axis Wind Turbines
HAWT	Horizontal Axis Wind Turbine
CFD	Computational Fluid Dynamics
CAD	Computer-Aided Design
CMOS	Complementary Metal-Oxide-Semiconductor
cv	control volume
DNS	Direct Numerical Simulation
NS	Navier-Stokes
DES	Detached Eddy Simulation
KM	Kinematic Models
FOV	Field of view
IW	Interrogation window
$v_{h,free}$	Friction Free Velocity
LES	Large Eddy Simulation
PIV	Particle Image Velocimetry
ppp	particle per pixel
RANS	Reynolds-Averaged Navier-Stokes equations
RHS	Right-Hand-Side
Std	Standard Deviation
s	Dimensionless Distance Downwind Rotor

Symbols

Symbol	Definition	Unit
α	Angle of attack	degrees ($^{\circ}$)
α_i	Incidence angle	degrees ($^{\circ}$)
Θ	Azimuth angle	degrees ($^{\circ}$)
U	Velocity	m/s
U_{∞}	Free stream Velocity	m/s
ρ	Density	kg/m ³
A	Area of rotor	m ²
T_L	Lift force	N
T_D	Drag force	N
C_T	Thrust force coefficient	-
C_D	Drag force coefficient	-
K^*	Wake expansion rate	-
$C_D A_{mm}$	Momentum term of drag area	kg · m/s
$C_D A_{mm}$	Pressure term of drag area	N/m ²
D	Diameter of VAWT	mm
D_a	Lens aperture	mm
f	Frequency	Hz
f'	Focal length	mm
P	Power	W
p	Pressure	N/m ²
I_0	Pulse energy	-
Λ	Tip-speed ratio	-
Ω	Rotational velocity	s ⁻¹
θ_p	Pitch angle	degrees ($^{\circ}$)
U	Normalised stream-wise wake velocity	m/s
ΔU	Normalised stream-wise velocity deficit	m/s
u_Y	Velocity component along Y	m/s
u_z	Velocity component along Z	m/s
u_{YZ}	Normalised in-plane velocity	m/s
X/D	Normalised stream-wise distance	-
Y/D	Normalised cross-flow distance	-
Z/D	Normalised span-wise distance	-
X	Stream-wise distance	mm
Y	Cross-flow distance distance	mm
Z	Span-wise distance	mm

List of Figures

2.1	Geometry and wake description of the Jensen model [48]	7
2.2	Frandsen model cylindrical control volume [12]	10
2.3	Left Jensen with top hat velocity profile, Right Jensen-Gaussian distributed velocity profile [51]	10
2.4	Comparison wake deficit max with wind-tunnel measurements (crosses), LES data (open circle), Bastankhah and Porté-Agel Model (solid line), Jensen model(dashed line) and Frandsen model(dotted line) for rotor downwind distances [6]	13
3.1	Force balance with VAWT setup	18
3.2	Working Concept of force Balance	19
3.3	Force Balance CAD design with detailed specifications	20
3.4	Fabricated Force Balance measurement device	20
3.5	Alignment and working of force balance system	21
3.6	Detailed CAD drawing of Vertical Axis Wind Turbine design	23
3.7	Fabrication, setup and working of VAWT rotor in OJF	23
3.8	Stereoscopic PIV working principled and concept [19]	24
3.9	Stereoscopic PIV setup at OJF TU Delft	27
3.10	Camera with set of adapters and mount	28
3.11	A preview from experimental campaign	29
3.12	Drag, Lift forces vs time period, (a) a time period of 10 seconds, (b) moving average of the same forces over a time period of 1 second	30
3.13	Variation of Lift and Drag forces over a single revolution	31
3.14	Trigger modes comparison: Mode 1 [32]	32
3.15	Trigger modes comparison: Mode 2 [32]	32
4.1	Wake velocity deficit parameters for CFD model, (a) wake velocity normalized by free stream velocity, (b) wake velocity deficit normalized by wake velocity deficit max for 10 rotors downwind distance	36
4.2	Wake velocity deficit normalize by ΔU_{max} fitted with a Gaussian distribution for half the crossflow width (Y/D) at different downwind distances (X/D=1,2,3,5,7,10)	37
4.3	Standard deviation in wake width (crossflow (Y/D)) VS Rotor downwind distance, with a linear fit	38
4.4	Comparison between theoretical model by (a) Mahdi Abkar Model, and (b) CFD model	39
4.5	Maximum wake velocity deficit (experiment case (zero pitch), CFD Model, Gaussian model) vs Streamwise distance (downwind)	39
4.6	Contour plot of wake velocity deficit normalised by free stream velocity ($\delta U/U_\infty$) for X/D= 2,3,5,7,10 rotor downwind distance for baseline case	40
4.7	Crosswind profile of centerline streamwise wake velocity deficit normalized by (U_∞) (solid blue line) CFD data, and (solid red line) Gaussian fit on them for 1,2,3,5,7,10 rotor downwind distance	41
4.8	Crosswind profile of centerline streamwise wake velocity normalized by (U_∞) (solid blue line) Experiment, (solid red line) Gaussian fit for 1,2,3,5,7,10 rotor downwind distance	42
4.9	The experiment standard deviation (solid blue line), CFD (solid orange line) of wake velocity deficit, linear fit(dotted red lines) vs Rotor downstream distance 1 X/D to 10 X/D	43
4.10	Contours of streamwise wake velocity at different downstream positions near wake (X/D= 1,2,3) normalized by the free stream velocity (U_∞) for baseline case	44
4.11	Contours of streamwise wake velocity at a different downstream position far wake (X/D= 5,7,8) normalized by the free stream velocity (U_∞) for baseline case	45

4.12	A comparison between Experiment data, CFD, Gaussian, Jenson wake model for downwind profile of centerline crossflow wake velocity deficit normalized by (U_{∞}) at ($X/D=1,2,3,5,7,8$) for baseline case	47
4.13	Crosswind profile of the centerline streamwise wake velocity deficit normalized by (U_{∞}) (at midspan). (Dotted line) experimental data (solid line) CFD data at ($X/D=1,2,3,5,7,8$) for baseline case	49
4.14	Vertical profiles of centerline spanwise wake velocity deficit normalized by the (U_{∞}) wind-speed (at the midspan) for different rotor downwind distance ($X/D=1,2,3,5,7,8$) for baseline case	49
4.15	Contours of baseline case streamwise velocity deficit at different downstream positions ($X/D=1,2,3,5,7,10$) normalized by the free stream velocity. In-plane velocity vectors are overlaid. The outline of the rotor is delineated by a black box.	50
4.16	Contours of streamwise wake velocity at different downstream positions near wake ($X/D=1,2,3$) normalized by the free stream velocity (U_{∞}) for positive 10° pitch angle	51
4.17	Contours of streamwise wake velocity at different downstream position far wake ($X/D=5,7,8$) normalized by the free stream velocity (U_{∞}) for positive 10° pitch angle	52
4.18	A comparison between Experiment data, CFD, Gaussian, Jenson wake model for downwind profile of centerline streamwise velocity deficit normalized by (U_{∞}) at ($X/D=1,2,3,5,7,8$) for positive 10° pitch angle	54
4.19	Vertical profiles of centerline streamwise velocity normalized by the (U/U_{∞}) wind-speed (at the midspan for different rotor downwind distance ($X/D=1,2,3,5,7,8$) for positive 10° pitch angle	55
4.20	Crosswind profile of the centerline streamwise velocity deficit normalised by (U_{∞}) (at midspan). (Dotted line) experimental data (solid line) CFD data at ($X/D=1,2,3,5,7,8$) for positive 10° pitch angle	56
4.21	Contours of positive 10° pitch case streamwise velocity deficit at different downstream positions ($X/D=1,2,3,5,7,10$) normalized by the free stream velocity. In-plane velocity vectors are overlaid. The outline of the rotor is delineated by a black box.	57
4.22	Contours of streamwise wake velocity at different downstream positions near wake ($X/D=1,2,3$) normalized by the free stream velocity (U_{∞}) for negative 10° pitch angle	58
4.23	Contours of streamwise wake velocity at a different downstream position far wake ($X/D=5,7,8$) normalized by the free stream velocity (U_{∞}) for negative 10° pitch angle	59
4.24	A comparison between Experiment data, CFD, Gaussian, Jenson wake model for downwind profile of centerline streamwise velocity deficit normalized by (U_{∞}) at ($X/D=1,2,3,5,7,8$) for negative 10° pitch angle	60
4.25	Crosswind profile of the centerline streamwise velocity deficit normalised by (U_{∞}) (at midspan). (Dotted line) experimental data (solid line) CFD data at ($X/D=1,2,3,5,7,8$) for negative 10° pitch angle	61
4.26	Contours of negative 10° pitch case streamwise velocity deficit at different downstream positions ($X/D=1,2,3,5,7,10$) normalized by the free stream velocity. In-plane velocity vectors are overlaid. The outline of the rotor is delineated by a black box.	62
4.27	Vertical profiles of centerline streamwise velocity normalized by the (U/U_{∞}) wind-speed (at the midspan) for different rotor downwind distance ($X/D=1,2,3,5,7,8$) for negative 10° pitch angle	63
4.28	Available power distribution along with the crosswind profile at $X/D = 1, 2, 5, 7$ for baseline, positive 10° , negative 10° case for experimental results	63
4.29	Moving integration window (solid black line), the outline of upstream VAWT (solid white line), Left negative Cross-flow width, and vice versa	64
4.30	Available power distribution along the crosswind profile at $X/D = 1, 2, 5, 7$ for baseline, positive 10° , negative 10° case for CFD simulations	65
4.31	Available power distribution along with the crosswind profile at $X/D = 1, 2, 5, 7$ for Gaussian wake model by M Abkar, and Jensen wake model	66
A.1	Wake superposition for three inline wind turbines[49]	74
A.2	Experiment setup schematic	75
A.3	Experiment setup for phase lock	77

A.4	Force measurements for positive pitch case	80
A.5	Force measurements for negative pitch case	80
A.6	VAWT cover Specifications	81
A.7	VAWT cover Specifications	81
A.8	Blue table specifications	82
A.9	Blue table specifications	82
A.10	Guidance for Transverse System	83

List of Tables

3.1	Turbine Specifications	22
3.2	Image specifications	28
3.3	Post-processing specifications	33
3.4	Wake velocity measurement case description	34
A.1	Phase lock system time delay measurements	76
A.2	Case description	78
A.3	Case description	79

Introduction

1.1. Background

The future necessities of mankind are pure water, clean energy, and better living space. As it is widely known that from the dawn of the industrial age, human activities have profoundly exacerbated the biosphere: with the increased concern for the rising level of energy consumption indicates that our world is on an unsustainable trajectory and solving this energy crisis requires a quicker shift towards non-conventional energy solutions. With this increasing global interest in renewable energies, wind energy is a very promising source of renewable energy for the future. It is witnessing continuous growth at an average annual rate of approximately 25%, stated by the Global Wind Energy Council [26]. Wind continues to retain its prominence amongst the other renewable technologies, as the compound annual growth rate (CAGR) in the wind sector is around 13% over the past five years. [44]. With all these installations, wind could provide around 1,270 TWh of electricity to the global grids

Wind turbines can mainly be classified as either Horizontal Axis Wind Turbines (HAWT) or Vertical Axis Wind Turbines, designated (VAWT). Although HAWTs have a higher power coefficient, which makes them more desirable for the large land stretches hence used by most power companies, whereas Vertical axis wind turbines (VAWTs) have regained interest during the last decade for application as large-scale multi-MW turbines in off-shore areas, and as small-scale turbines in urban environments. There are certain applications where VAWTs could offer superior performance compared to the conventional horizontal axis wind turbines (HAWTs) [36]. The large-scale vertical axis wind turbines are interesting for offshore applications: their simple mechanical design with fewer moving parts reduces the complexity lowering manufacturing, installation, and maintenance costs. Advantages such as scalability, robustness, reliability, and installation of the generator on the ground characteristic also improve the stability of the structure by locating the center of gravity closer to the ground. While their omnidirectional capabilities and lower noise make them highly desirable for urban environments where the wind direction is frequently changing. [31]. However, a significantly lower amount of research in the past three decades has resulted in VAWT performance falling behind that of their horizontal-axis counterparts.

In these recent years, several research activities have focused on further understanding the complex unsteady aerodynamics of VAWTs. Also, a renewed interest in VAWT farm-scale, particularly spurred by works which have shown significant increases in performance at large scales [15]. Considering the increasing size of wind farms, the farm size context is becoming a larger influence on wind farm developments. In a wind farm, turbines should be far enough apart to allow wind speeds to recover, through lateral or vertical momentum entertainment, after deceleration by the upwind turbine (Cortina et al. 2016). Spacing the turbines also reduces the fatigue load generated by turbulence from the up-stream turbines and thus increases turbine lifetime. This is enhanced by the spacing between HAWTs, and their arrangement and is considered often as little as 7 diameters between turbines [4] The studies have shown that this can cause severe detriments to farm performance, and even spacings as large as

12D result in a 40% reduction in performance [15]. In contrast, it has been shown that with good farm design, such small and even smaller spacings for VAWTs are not just viable but in fact can be desirable, potentially offering a magnitude increase in power per area compared to an optimized HAWT farm.

Referring to the above context, a substantial challenge in developing and managing Vertical axis wind energy farms is understanding the power losses due to the wake effect. It is well accepted that the wakes created by upstream turbines significantly impact the power production and fatigue loading of downstream turbines and that this phenomenon affects wind farm performance. If we can demonstrate its effectiveness in the complex wind farm flow/inflow will be of great importance. Hence, improving the understanding of wake effects and overall efficiency is critical for the optimization of the layout and operation of increasingly large wind farms [47].

1.2. The motivation of the study

VAWT operation is characterized by complex and unsteady three-dimensional fluid dynamics, which presents considerable challenges and one of the crucial points to understand is the complex interaction between rotor, inflow, and wake systems (Van Kuik et al., 2016). To investigate the wind/wake aerodynamic flow in computational fluid dynamics, high computational methods are extensively used, computed by solving the full or filtered Navier-stroke equations. There are a number of different CFD models ranging from high to low complexity depending on the assumptions made (e.g. Direct numerical simulation (DNS), simulation of turbulent flows by numerically solving the Navier–Stokes equations requires resolving a very wide range of time and length scales, all of which affect the flow field. Such a resolution can be achieved with direct numerical simulation (DNS), but DNS is computationally more expensive. Large Eddy Simulation, LES is to reduce the computational cost by ignoring the smallest length scales, which are the most computationally expensive to resolve, via low-pass filtering of the Navier–Stokes equations. Reynolds averaged NS (RANS) equation, The idea behind RANS is Reynolds decomposition, which gives approximate time-averaged solutions to the Navier–Stokes equations. Accurate simulation results can be acquired through this method, which is in good agreement with experimental models. However, the CFD models are highly time-devouring and computationally expensive, and their cost prohibits the simulation of complex flow configurations.

This is usually overcome through the implementation of simple and computationally inexpensive analytical wake models, where the flow conditions are solved through simple analytic expressions and only over specific points of interest. Analytical wake models, as opposed to high-fidelity computational fluid dynamics (CFD) models, are simple, easy to implement, and computationally inexpensive.

1.3. Aim and Hypothesis

The aim of the work is to realize and validate a simple and efficient analytical wake model method for prediction of the wind velocity profile downwind of VAWT wind turbine: The best by comparing the modeling results with a set of particle image velocimetry (PIV) measurements of the wakes of an in-house designed VAWT are used as a high-fidelity reference. Besides, the CFD data for the same isolated VAWT by Ming Huang [17] is used for comparison. The main hypothesis can be formulated as follows: To establish the suitability of these references to verify the analytical models' range of fidelity. If this hypothesis is found to be close to the suitability of these references, the next point of attention will be the engineering model, to see how the differences between these two inputs are modeled. What parameters do the engineering models fail to properly account for and what kind of adjustment will need to be made in the future. Afterward, ways should be found to include, different cases of wake interaction from upstream turbine over downwind regions, stream-wise, through pitching the blades on the upstream turbine. Also, force measurement systems calculate the drag and lift forces on the rotor.

1.4. Research Questions

In order to resolve the above objective, the following research questions are framed

1. What is the state-of-the-art of analytical wake models? What are representative VAWT wake models in the literature to capture its wake velocity profile in a simple and more accurate form?
2. Design of the experiments
 - (a) How could the design of scaled VAWT be improved
 - (b) With what means wake on a small scale vertical axis wind turbine model can be deflected? (blade pitching).
 - (c) How can the lift and drag forces on the rotor structure be measured.
 - (d) How to experimentally measure the flow fields of a VAWT (small scale rotors) with different pitch configurations?
3. How to validate the chosen theoretical engineering models with the experimental post-processed data?

To answer the above research questions the following sub-goals were set:

1. Perform a literature study in which we identify
 - (a) The major constraints involving wake development for wind turbines.
 - (b) Study of different available state-of-the-art wind wake models
 - (c) Comparative study of analytical models reviewed to high fidelity simulations and data.
2. Experimental work
 - (a) An actual scaled model of vertical axis wind turbine (VAWT) will be constructed, with required modifications for passive blade pitch control (which will be selected based on literature study) for wake deflection.
 - (b) The present work will be able to evaluate and quantify the influence of the wake deflection produced by the pitch angle of the blades of the scaled VAWT turbine, and to reproduce the main phenomena involved in the flow pattern identifying the general structure of the resulting wake. This will be carried out in the form of a wind tunnel experiment
 - (c) The measurement technique of drag and lift forces on the VAWT rotor, through Literature study of force balance apparatus. Followed by the designing and fabrication of a new force balance system, which is ergonomic to use and can calculate the drag and lift forces on the VAWT rotor with a high range of accuracy and reliability.
 - (d) The influence of the wake deflection produced by upstream turbine over downstream, the velocity deficits relating to it, and the availability of power over hypothetical downwind turbine will be studied. Also, these interactions will be measured with the help of large-scale PIV experiments to obtain detailed maps of velocity and vorticity within the wake of the rotor. An experimental setup will be further designed and constructed to facilitate the PIV equipment (ex:- Lasers, cameras, transverse system, etc) so that everything works in coherence.
3. Program and validate the low fidelity wake model for a single turbine. The theoretical model fidelity will be based on comparison and studies against the available CFD simulation data from previous experiments by (Huang et al. [17]) and the experimental post-processed data. where the experimental results will be used to validate the theoretical model.

The questions above focus on understanding the state-of-the-art analytical models, experimentally validating/verifying the existing wake model Screening the most important quantities that need to be measured for validation purposes. (It assumes indirectly that one of the proposed single wake models achieves the best results). Designing the experiment, measurement cases, and conducting the experiment to acquire the quantities. Finally, Present the velocity fields in a clear manner, the realization of the analytical models and compare them with the experimental data, further validate or sort the range of validity of these models, and make scientific statements on the results.

1.5. Report Outline

The chapter 2 gives an overview of the basic terminologies for the thesis and high fidelity simulation and their solving techniques. For the most part, provides a literature study performed on state of the art wind wake models their improvement over the years. Here based on the study an optimum and reliable single wake model and wake measurement technique are chosen. In continuation to that chapter3, gives a brief explanation for the design system, their fabrication process, and measurement techniques, required in order to conduct the experiments successfully. Also, provides details for techniques used in the experimental campaign and the measurement steps taken to conduct a successful experiment. Chapter4, provides realization of the chosen theoretical wake model to the CFD simulation data from previous experimental campaigns. Also, the results are compared against LES(Large Eddy Simulation data), wind tunnel experiments, and two other theoretical models from different publications (Jensen wake model [20] , self-similar model by M. Bastankhah, F. Porté-Age [6]). The chapter also provides an explicit comparison of the theoretical models to the experimental results and establishes the suitability of these experimental results to verify the analytical model's range of fidelity. Scientific statements are conferred based o the experimental results. The Chapter 5 provides final conclusion of the thesis and provides recommendations for future scope of work and changes that can be accommodated for future study.

2

Literature Review

In order, to answer the earlier formed research questions a literature study was performed and is presented in this chapter. The following learning goals were set to be obtained from the literature review: Understanding the wind turbine wake, learning about the development of different available wind turbine wake models, and finding an appropriate and reliable wind wake model which can be later used for validation of the experiment. In section 2.1 the wake characteristics will be discussed. In section 2.2 - the development of the different available wind wake models will be discussed and lastly, the selected model is been described. Section 2.3 provides explicit details on previous work in field-scale measurements, Laboratory experiments, and numerical simulations.

2.1. Turbine Wake

The undisturbed wind speed is reduced and transforms into a more turbulent form when passed over the wind turbine: After the wind energy has been extracted. This trail of these turbulent and reduced wind speeds is called the wind turbine wake. This wake influences the performance of the downstream turbines. The study of wind turbine wakes is broken into two categories: near wake and far wake.

2.1.1. Near Wakes

The near wake region is concerned with power extraction from the wind by a single turbine, it is the region just behind the wind turbine, which extends to approximately 2-4 rotor diameters downstream. This near Wake flow has a lower velocity and a higher turbulence intensity, which decreases the power production and increases the unsteady loads over the affected turbines in the wake. It is expected that the unsteady effects of momentum deficit and increased level of turbulence will vanish with adequate degree far downstream of the wind turbine: because of turbulent diffusion of the wake. The study of the near wake region is a quite difficult issue to subsist with. Common assumptions are made with considering the flow to be uniform, in-compressible and parallel flow conditions. Although, there have been attempts to tackle this topic, the basics of wind turbine aerodynamics are not fully understood.

2.1.2. Far Wakes

Whereas the far wake starts at the location where the tip vortex breaks down in the near wake. It is more focused on the mutual influence when wind turbines are placed in clusters. For that reason, the study of this region is one of the aims of the study and of high importance in wind farms. [30]. The flow field is fully developed in the far wake, and is independent of the rotor characteristics, and is governed by two main mechanism, convection and turbulent diffusion [45].

It is expected that far enough downstream the momentum deficit and increased turbulence will vanish because of turbulent diffusion of the wake. From measurements and the available data from

wind farms and experimental setups, it is concluded, that in the far wake both the velocity deficit profile and turbulence intensity profile are axisymmetric and have self-similar distributions in the cross-section of the wake [45]. This property of self-similarity is the basis of the kinematic models describing wind turbine wakes. For both these regions, the velocity deficit can be computed with different models and techniques. Which will be discussed in the latter part.

2.2. State-of-the-art & historical development of turbine wake models

Several models exist to compute the wind profile and wake deficit behind a single wind turbine. These modeling techniques used over the span of time also differ a lot. In this chapter these available models will be discussed. The models can be distinguished into three major categories: The CFD models, Flow Field models, and the Kinematic models. Where the CFD models are the highest fidelity and high computationally expensive models whereas the Kinematic models are with the lowest fidelity models and much less computationally expensive. The results of these models can then be used to calculate the wind field in a wind farm by applying different wake superposition methods.

2.2.1. CFD Models

There are different types of CFD models available. The most commonly used models are the Direct Numerical Simulation (DNS), Reynolds Averaged Navier-Stokes (RANS), Large-Eddy Simulation (LES), and Detached Eddy Simulation (DES).

This model can be used for detailed studies of the interaction of turbulent inflow with rotor blades or the interactions between wakes. However, this may take several hours to run and are high computationally expensive for example: high resolution, time-resolved LES models, where computation may take several weeks to complete on a large cluster. The computational costs of DNS are even more excessive, currently prohibiting its use in industrial applications. There have been attempts to use CFD models with decreased or less computational times. One of these CFD models is the FUGA model. However, none of these CFD models, or not even the FUGA model, will be feasible for computing the flow field in a whole wind farm and impossible to use it for annual energy production (AEP) estimations [33]. Hence to conclude these models require a lot of computational resources and time to compute the flow field for a wind farm, which is not available.

2.2.2. Field Models

As compared to the CFD models, the flow field models are of lower fidelity. These models calculate the flow magnitudes at every point of the flow field. These models are based upon approximations of the Navier-Stokes equations, such as the Ainslie model [2]. In this model at each point of the chosen mesh, differential equations need to be solved numerically. This solving requires a certain amount of computational power, however, which is still less than for CFD models. For large-scale experiments, the results are corrected by taking into account meandering effects [33].

2.2.3. Actuator line Model

To bridge the gap between the high and low fidelity numerical modeling aids, an actuator line model (ALM) was developed. The ALM is a combination of classical blade element theory and the Navier-Stokes based flow model. The ALM was originally developed by Sorensen and Shen [40], is an unsteady method that tracks blade element locations and has become popular for modeling axial flows. It has good accuracy when compared with blade-resolved CFD. The ALM when combined with LES becomes the state of the art for modeling entire wind farms [5].

2.2.4. Kinematic Models

The kinematic models are considered to be the lowest fidelity models with a low computational complexity that can be used for predicting the spatial distribution of wind velocity field downwind of a rotor.

These models are usually based upon mass momentum conservation and turbulence mixing. Due to their lesser complicity, the computational times are lower as compared to CFD and field models.

The first approach to study the wind turbine wakes with a so called kinematic model approach was formulated by Lissaman [40]. He used velocity profiles obtained from the experiments and theoretical work. Whereas Vermeulen [46] assumed Gaussian type of wind wake profile. One of the pioneering kinematic models is the one proposed by Jensen [20], which assumes a top-hat shape for the velocity deficit in the wake. This was further developed by Katic [23], Larsen model [10] and the Frandsen model [12], where Frandsen employed the mass and momentum equations, while still assuming a top-hat shape for the velocity deficit in the wake. Also, two new and promising theoretical kinematic models will be discussed first one is the Jensen-Gaussian model [13], and the second is Bastankhah and Porté-Agel [6] one of these models will be chosen for the study based on its reliability and most approximate closeness to the real CFD simulation data.

2.2.5. Jensen

A simple model for the wake behind a wind turbine is given by Jensen [20] which was further developed by Katic et.al [23]. The single wake Jensen model has certain assumptions, the far wake starts immediately after the rotor, thus miss-treating the near wake region. This also means that for the near wake region, the velocity field cannot be computed accurately. The model assumes a prescribed linear geometry for the wake expansion. where the wake starts with a diameter equal to that of the rotor. Furthermore, the profile of the average wind speed in the wake is prescribed to be a constant velocity the so-called 'top-hat' profile. This means that the velocity at certain points in the wake is not accurate, however, the model is used to give an estimate of the energy content in the flow field, rather than to accurately model the velocity field. The model also neglects the blockage effect due to the ground surface, hence the wake expands freely. The Jensen model is based on conservation of mass, the predefined description of the wake structure is shown in the figure 2.1. The control volume is not part of the wake description, but it will be used later in the derivation of the model equations

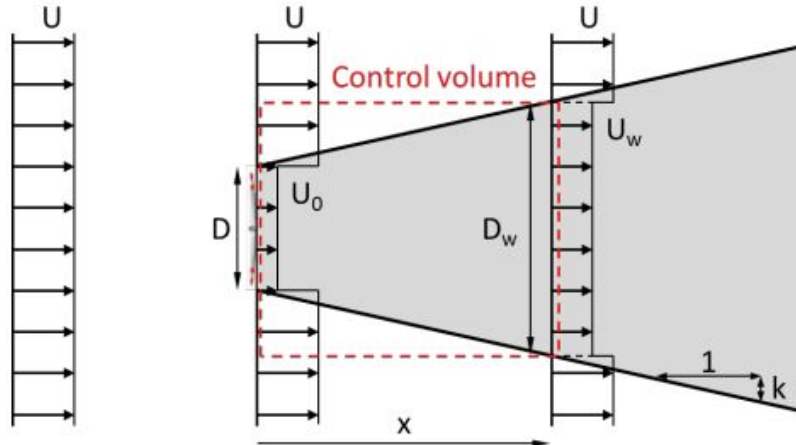


Figure 2.1: Geometry and wake description of the Jensen model [48]

On the left-hand side of the figure, you see the undisturbed wind speed, upstream of the rotor (U). The wake starts at the rotor, with a diameter equal to the rotor diameter D . It expands linearly, meaning that the radius of the wake increases with k for every unit of distance in downwind direction x . The wind speed inside the wake at the position of the rotor is U_0 . At other places in the wake, it is U_w , which is a function of the distance x , but which is constant within the wake diameter D_w . Outside the wake, the wind speed remains undisturbed (U). D is the diameter of the turbine rotor and D_w is the span-wise width of wake expansion at distance x from the rotor.

The fundamental equation used by Jensen to derive his model was based on conservation of mass.

Applying this to a cylindrical control volume as shown in Figure 2.1.

$$\rho U_0 \frac{1}{4} \pi D^2 + \rho U \frac{1}{4} \pi (Dw^2 - D^2) = \rho U_w \frac{1}{4} \pi DW^2 \quad (2.1)$$

The first term on the left is the mass flow through the rotor area. The second term on the left is the mass of the flow through the ring surrounding the rotor, up to the wake diameter Dw . The right-hand side is the mass flow through the wakes span-wise width at distance x . The above equation 2.1 can be written as

$$U_0 D^2 + U(Dw^2 - D^2) = U_w D W^2 \quad (2.2)$$

With the momentum theory, U_0/U can be defined as a function of the axial induction factor, which is the fractional decrease in wind speed, and is expressed as follows:

$$\frac{U_0}{U} = (1 - 2a)$$

substituting this in the equation above

$$(1 - 2a)D^2 + (Dw^2 - D^2) = \frac{U_w}{U} DW^2 \Leftrightarrow \left(1 - \frac{U_w}{U}\right) = \frac{D^2}{Dw^2} 2a \quad (2.3)$$

The wake diameter can be determined from the prescribed geometry, resulting in

$$1 - \frac{U_w}{U} = \left(\frac{D}{D + 2ks}\right)^2 2a = \frac{2a}{(1 + 2ks)^2} \quad (2.4)$$

where $s = \frac{x}{D}$, the dimensionless distance behind the rotor.

Since it is more convenient to use the thrust coefficient than the induction factor, $a = 1/2 - 1/2\sqrt{1 - CT}$ substituting it in ref:mass flow jensen3, we get the final expression.

$$1 - \frac{U_w}{U} = \frac{1 - \sqrt{1 - CT}}{(1 + 2ks)^2} \quad (2.5)$$

From the equation 2.5 it can be clearly devise that the velocity in the wake depends on, the x distance downstream of the rotor, the wake decay coefficient (k): and also, the thrust coefficient C_T . The wake decay coefficient is an empirical parameter and according to [3], it can be written as

$$k = \frac{v_{free}}{v_{hfree}} \quad (2.6)$$

where (v_{free}) is the free friction velocity and (v_{hfree}) is the free hub height wind speed. These expression is a function of surface roughness length, local atmospheric stability correction at hub height, and turbulence intensity In more general terms, The more turbulence, the higher the mixing with the undisturbed wind outside the wake, the higher the wake expansion, and thus the higher k . Higher mixing also means that recovery of the wind speed in the wake goes faster and you can confirm that U_w increases quicker when k is larger. The most commonly used wake decay coefficients are 0.075 for on-shore and 0.04 for off-shore wake decay coefficients [3]. An example of the velocity profile computed with the Jensen-Katic model can be found in figure

Top-Hat wake model of VAWT wakes by Abkar

In this model, it is assumed the wake downstream of an H-rotor VAWT with a blade span of H and rotor diameter of D has a rectangular shape with dimensions H_w and D_w . Which are assumed to expanding linearly as the wake is transported downstream.

$$H_w = H + 2K_{wz}x, D_w = D + 2K_{wy}x \quad (2.7)$$

where K_{wz} is the rate at which the wake expands in the span-wise width along with the height of the rotor and K_{wy} being the rate of expansion along the cross-flow direction. Here the rate of expansion

for the wake is considered to be a linear growth similar to the above Jensen model [20]. For the above equation 2.7 applying the mass continuity and considering a top-hat shape for the wake velocity deficit, it can be written as

$$\rho U_w A_w = \rho U_a A_p + \rho U_\infty (A_w - A_p), \quad (2.8)$$

where ρ is density of air, U_∞ is the free stream velocity before the rotor, U_w is the wake velocity after the rotor (rotor downstream). $A_w = D_w H_w$ is the wake area and $A_p = DH$ is the turbine projected area. Whereas U_a shows the velocity immediately downstream of the rotor (very near wake) and is related to the free stream velocity with the following expression.

$$U_a = (1 - 2a)U_\infty A_p, \quad (2.9)$$

where a is the induction factor. Substituting 2.7 and 2.9 in equation 2.8, an equation for the normalized velocity deficit is obtained,

$$\frac{\Delta U}{U_\infty} = \frac{U_\infty - U_w}{U_\infty} = \frac{2a}{(1 + 2K_{wz}x/H(1 + 2K_{wy}x/D))}, \quad (2.10)$$

Here the induction factor in the above equation 2.10 can be estimated using the momentum theory studied above in Jensen's model ($a = 0.5(1 - \sqrt{1 - C_T})$). C_T is the thrust coefficient used according to the projected area of the turbine $C_T = F_x / (0.5\rho A_p U_\infty^2)$, where F_x is the total force acting on the rotor in the mean wind direction. For simplicity and realizing the Jensen model [20] the rate of wake expansion in span-wise and cross-flow directions is assumed to be the same, $K_{wz} = K_{wy} = Kw$. With this, it should also be noted that, if considered the turbine has a circular projected area with diameter D , the above equation gets converted into the Jensen model proposed for HAWT wakes as mentioned in the above section.

2.2.6. Frandsen Model

Frandsen [12] developed this model, it is designed for a specific layout of the turbines in a wind farm: the model handles a regular array geometry with straight rows of wind turbines and an equidistant spacing between each unit and also between each of the rows. A dimensionless distance between two equidistant turbines is defined as: ($s = \frac{x}{R}$), where x is the actual stream-wise direction and R is the radius of the turbine. The wind direction is assumed to be parallel to the rows. For the single wake model, the analytical expression is derived from the momentum conservation. The momentum conservation is applied over a controlled cylindrical volume around the wind turbine rotor with a diameter equal to that of the wake. The acceleration term, the pressure term, shear forces and the gravity term are neglected in basic considerations. T is the sum of forces from obstacles acting on the interior of the control volume, (thrust force) and is written as:

$$T = \int^A \rho U (U_0 - U) dA, \quad (2.11)$$

where A is the cross-sectional area of the wake, U_0 is the undisturbed wind speed, and U is the wake velocity. The equation above can also be written as

$$T = \frac{1}{2} C_T \rho A_0 U_0^2, \quad (2.12)$$

where C_T is the thrust coefficient, ρ the density at hub height, and A_0 is the swept area by the rotor. The figure 2.2 represents the control volume used for the momentum conservation equation above. The circular wake cross-section is assumed to be with uniform velocity and the x stream-wise distance starts only after the wake expansion. From the above Frandsen [12] derived the following equations:

$$D(s) = (\beta^n / 2 + \alpha \dot{s})^{1/n} D_0, \quad (2.13)$$

where:

$$\beta = \frac{1 + \sqrt{1 - C_T}}{2 \sqrt{1 - C_T}}, \quad (2.14)$$

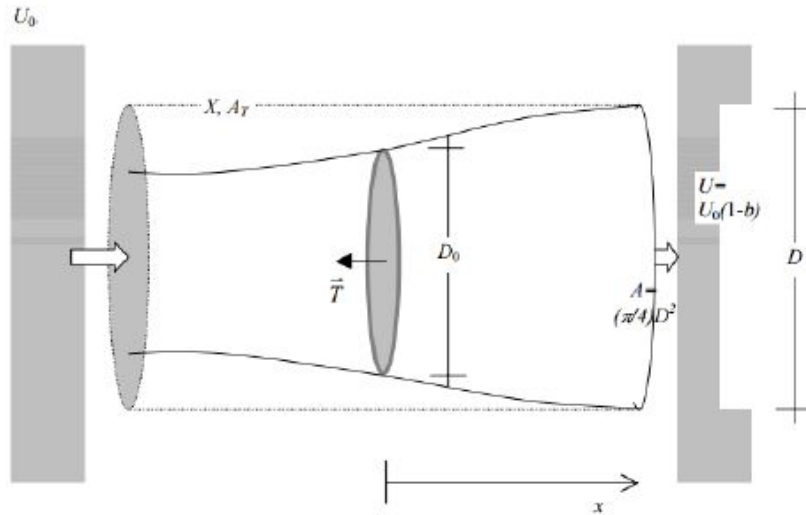


Figure 2.2: Frandsen model cylindrical control volume [12]

$$\frac{U}{U_0} = \frac{1}{2} \pm \frac{1}{2} \sqrt{1 - 2 \frac{A_0}{A} CT} \tag{2.15}$$

The value of α (decay constant) is determined from experiments. n is 3 it is the parameter that defines the shape of the wake expansion [12]. It should be noted that equation 2.15 will use the plus sign when $1 - \sqrt{1 - CT} \leq 0.5$ and the minus sign when $1 - \sqrt{1 - CT} > 0.5$. An example of the wake is shown in the figure below.

2.2.7. Jensen-Gaussian

The studies performed with the Jensen-Katic model which assumes a top hat wake velocity profile, for optimization of wind farm layout: certain assumptions caused inaccuracies in the computation according to [51]. From wind-tunnel experiments and on-site wind farm measurement [16] it was found that a Gaussian velocity distribution in the wake is more realistic for predictions of wake velocities in the far wake and optimization of wind farm layouts. Hence, Jensen’s wake model was modified by [51] to incorporate the Gaussian velocity distribution into its model. In figure 2.3a comparison between the two models can be found.

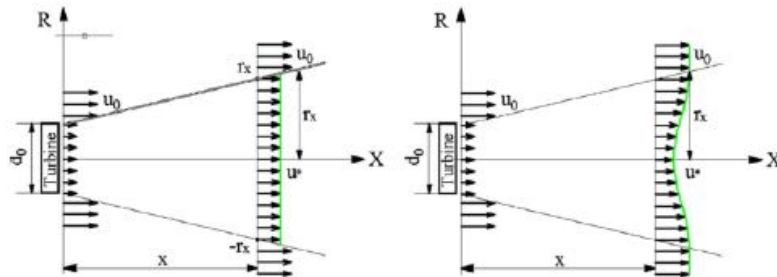


Figure 2.3: Left Jensen with top hat velocity profile, Right Jensen-Gaussian distributed velocity profile [51]

The expression for the wake velocity is given to be :

$$u = A \frac{1}{\sigma \sqrt{2\pi}} \cdot \exp \frac{-r^2}{2\sigma^2} + B \tag{2.16}$$

For finding the parameters in the above equation (A, B and σ) the following assumptions are followed. Using the properties of a Gaussian distribution it is proposed to have $2.58\sigma = r_x$, to obtain a 99% of the Gaussian distribution, where r_x is the wake radius of the original Jensen model. The velocity directly outside this wake radius r_x is equal to the free stream velocity.

$$u_0 = A \frac{1}{\sigma\sqrt{2\pi}} \cdot \exp \frac{-r^2}{2\sigma^2} + B \quad (2.17)$$

Throughout the wake with both the models (Jensen model and Jensen-Gaussian) having same r_x are also assumed to have the same mass flow rate, hence giving the following equation:

$$\int_{-r_x}^{r_x} (A \frac{1}{\sigma\sqrt{2\pi}} \cdot \exp \frac{-(y)^2}{2\sigma^2}) + B) dx = u^* 2r_x \quad (2.18)$$

solving the above equation 2.18 for A, B and σ gives:

$$\sigma = \frac{r_x}{2.58}$$

$$B = u_0$$

$$A = (u^* - u_0) 2r_x$$

Therefore for the Jensen-Gaussian wake model, the following equations describe the velocity profile at a distance x downstream of the rotor:

$$u^* = u_0 [1 - 2a / (1 - 2a / (1 + kx/r_1)^2)] \quad (2.19)$$

$$u = u_0 - (u_0 - u^*) \frac{5.16}{\sqrt{2\pi}} \cdot \exp -r^2 / 2 \cdot (r_x / 2.58)^2 \quad (2.20)$$

Where k is the wake expansion rate, which is given by 2.21.

$$k = 0.5 / \ln \frac{z}{z_0} \quad (2.21)$$

The Jensen-Gaussian model, wake wind velocity deficit is modeled in the figure below

2.2.8. Bastankhah and Porté-Agel Model

The Bastankhah and Porté-Agel Model, was developed by Bastankhah and Porté-Agel [6]. The model has been derived from the momentum equation just similar to the Frandsen model. The important difference between these two models is the wake velocity deficit profile. The Jensen and Frandsen model assumes a top hat velocity profile where as in the Bastankhah and Porté-Agel Model, it is an axisymmetric Gaussian shape. From the wakes of bluff bodies in free stream velocities that have been extensively studied in classical theories of shear flows [21]. These studies present, the self-similar Gaussian profile of the velocity deficit in the far-wake regions. For wind turbine wakes in turbulent boundary layers, even though the velocity distribution does not show axisymmetric behavior [34], the velocity deficits in the wake has an approximately a Gaussian axisymmetric profile after some downwind distances [34].

This Gaussian shape of the velocity deficit in turbine wakes has been observed through wind-tunnel measurements [21], numerical simulations [50], and data of operating wind farm [16]. Hence, Gaussian distribution is a relevant way to describe the wind velocity wake (certainly more concrete in far wakes). The following equation can be obtained for normalised wake velocity deficit by applying mass and momentum conservation and neglecting the viscous and pressure terms:

$$\frac{\Delta U}{U_\infty} = C(x) f(r/\partial(x)), \quad (2.22)$$

where C(x) represents the maximum center normalized velocity deficit at each downwind location, r is the radial distance from the center of the wake, and $\partial(x)$ the characteristic wake width at each x. The

velocity deficit in the turbine wake, regardless of incoming conditions, is assumed to have a Gaussian shape. Thus, the above equation 2.22 can be written as:

$$U_w = U_\infty = (1 - C(x) \exp\left(-\frac{x^2}{2\sigma^2}\right)) \quad (2.23)$$

where σ is the standard error of the Gaussian like velocity deficit profile at each x . Inserting equations 2.12 and 2.23 into equation 2.11 and integrating it from 0 to ∞ will give the following equation:

$$8\left(\frac{\sigma}{d_0}\right)^2 C(x)^2 - 16\left(\frac{\sigma}{d_0}\right)^2 C(x) + C_T = 0 \quad (2.24)$$

By solving Equation 2.24, two values for $C(x)$ are acquired while only one of these values, which predicts the smaller value for the velocity deficit at larger downwind distances, is physically acceptable:

$$C(x) = 1 - \sqrt{1 - \frac{C_T}{8(\sigma/d_0)^2}} \quad (2.25)$$

When a linear expansion for the wake is to be considered then σ/d_0 can be written as:

$$\frac{\sigma}{d_0} = k^* \frac{x}{d_0} + \epsilon, \quad (2.26)$$

where $k^* = \partial\sigma/\partial x$ is the growth rate and ϵ is equivalent to the value of σ/d_0 as x approaches zero. Therefore, the final expression for the model:

$$\frac{\Delta U}{U_\infty} = \left(1 - \sqrt{1 - \frac{C_T}{8(K^*x/d_0 + \epsilon)^2}}\right) \times \exp\left(-\frac{1}{2(K^*x/d_0)^2} \left(\frac{z - z_h}{d_0}\right)^2 + \left(\frac{y}{d_0}\right)^2\right), \quad (2.27)$$

The above equation gives the normalized velocity deficit in the wake as a function of normalized coordinates. where y and z are the span-wise and vertical coordinates and z_h is the hub height. To achieve the wind velocity deficit from the above equation 2.27 requires the value of " ϵ ", which can be determined by equating the total mass flow deficit rate at $x = 0$ obtained by the Frandsen model and the one obtained by this model. This can be calculated, because both the models are derived from the same governing equations. The following relationship for " ϵ " is derived:

$$\epsilon = 0.25\sqrt{\beta} \quad (2.28)$$

where β is given by:

$$\beta = \frac{1}{2} \frac{1 + \sqrt{1 - C_T}}{\sqrt{1 - C_T}} \quad (2.29)$$

According to the LES data with a comparison to the Bastankhah and Porté-Agel Model, the above expression with a lower constant coefficient gives a better estimation of the value of ϵ , The value of ϵ should therefore be lower than the one predicted by equation 2.27. hence,

$$\epsilon = 0.20\sqrt{\beta} \quad (2.30)$$

The relationship between the wake width growth rate k^* and the longitudinal turbulence intensity TI_x is presented by

$$k^* = 0.35TI_x \quad (2.31)$$

The data from the full-scale field experiment, and from validated LES simulations as well as wind tunnel experiment, presented in [6], agree well, taking into account the significant variability of the data. The data show clearly that the rate of growth of the wake width increases with the turbulence intensity. ($0.065 < I_a < 0.15$) A linear fit to the full-scale field data gives:

$$k^* = 0.383TI_x + 0.0037 \quad (2.32)$$

Where I_a is the ambient turbulence intensity and I is the local turbulence intensity at the turbine rotor. The analytical model to be programmed will be based on the Bastankhah and Porté-Agel model as it gives most reliable and accurate profile for a wind velocity deficit. A similar relationship for k^* , $\left(\frac{\partial\sigma}{\partial x}\right)$ based a CFD will be developed and will be discussed further in chapter 3, where the programmed model will be validated against the Bastankhah and Porté-Agel Model and all other models. Using data for a wind tunnel experiment.

Theoretical Modeling of VAWT wakes by Abkar

With the lack of improved low-order models, in order to produce/predict the spatial distribution of the wake velocity deficit in the far-wake region for a VAWTs in real conditions [1] Mahind Abkar, developed a reliable theoretical model with less computation and simple design for prediction of wind velocity field downstream of an H-rotor wind turbine and power harvest optimization operations. This model is extremely useful for the focus of this study. In this model, it is preferred that the wake downstream (far wake) of an H-rotor VAWT with a blade span of H and rotor diameter of D has a self-similar Gaussian shape consistent with the classical theory of shear flow [37]. Considering this important finding, and applying mass continuity and momentum balance theory (as similarly used in Bastankhah and Porté-Agel [6] for HAWTs), according to them the maximum velocity deficit downstream of the turbine is

$$\frac{\Delta U_{max}}{U_{\infty}} = 1 - \sqrt{1 - \frac{C_T}{2\pi(\sigma_z \sigma_y / A_p)}} \quad (2.33)$$

Here the σ_z and σ_y are the standard deviations of the velocity deficit distribution in span-wise and cross-flow direction respectively. By applying a two-dimensional Gaussian function for the wake, the velocity deficit can be described as

$$\frac{\Delta U}{U_{\infty}} = \frac{\Delta U_{max}}{U_{\infty}} \times \exp\left(-\frac{1}{2}\left[\left(\frac{z - z_h}{\sigma_z}\right)^2 + \left(\frac{y}{\sigma_y}\right)^2\right]\right) \quad (2.34)$$

σ_z and σ_y are varying quasi-linearly with the downwind distance in the turbulent inflow as

$$\sigma_z = k_z^* x + \epsilon H, \sigma_y = k_y^* x + \epsilon D, \quad (2.35)$$

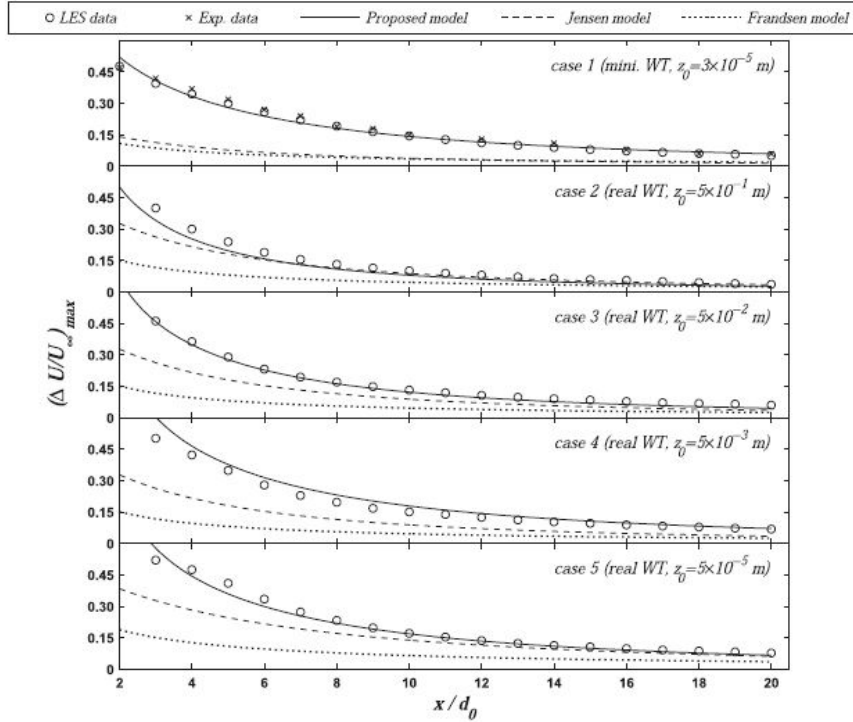


Figure 2.4: Comparison wake deficit max with wind-tunnel measurements (crosses), LES data (open circle), Bastankhah and Porté-Agel Model (solid line), Jensen model(dashed line) and Frandsen model(dotted line) for rotor downwind distances [6]

Here the wake expansion rates in the span-wise and cross-flow directions are represented by k_z^* and k_y^* respectively. The non- dimension parameter ϵ , which characterize the standard deviation of the wake at the rotor, is defined as $\epsilon = 0.25\sqrt{\beta}$, where $\beta = 0.5(1 + \sqrt{1 - C_T})/\sqrt{1 - C_T}$. In this model for simplicity, it has been assumed that the wake expansion in span-wise and cross-flow directions are the

same, but this is not a case for real application and is further evaluated in the experimental comparison phase. Note that for the above equation if we consider a circular projected area of diameter D , the equation leads to the formula introduced by Bastankhah and Porté-Agel [6] for HAWT wakes. Also, the wake in the VAWT is slightly deflected in the cross-flow direction, due to blade rotation is not taken into account in this model. This deflection of the wake is further studied in the experimental and theoretical model comparison section.

2.2.9. Self-Similar Gaussian Distribution for VAWT

In particular, the model examines the self-similarity of the wake structure downwind of a VAWT, and it is found that the wake velocity deficit can be well-characterized by a two-dimensional multivariate Gaussian distribution. By assuming a self-similar Gaussian distribution of the velocity deficit, and by applying the mass and momentum conservation, an analytical model is developed and tested to predict the maximum velocity deficit downwind of the VAWT turbine.[1]

In the span-wise direction of the wind turbine, the momentum deficit flow rate, $M(x)$, is defined as:

$$M(x) = \int \rho U (U_{in} - U) dA. \quad (2.36)$$

In the self-similar region, $M(x)$ can be also written in terms of U_{in} , ΔU_{max} and $(\eta) = \Delta U / \Delta U_{max} = \exp(-\frac{r^2}{2\sigma_{eq}^2})$, where σ_{eq} is equivalent standard deviation of the Gaussian like velocity deficit profile at each point of x . Hence,

$$M(x) = T = \frac{1}{2} C_T \rho A_p U_{in}^2, \quad (2.37)$$

Where, C_T is the thrust coefficient, $A_p = H \times D$. (H = height of the rotor, D = diameter of the rotor). By using equation 2.37 in equation 2.36 and integrating from 0 to ∞ , the maximum velocity deficit equation is formed:

$$\frac{\Delta U_{max}}{U_{in}} = 1 - \sqrt{1 - \frac{C_T}{2\pi(\sigma_{eq}^2/A_p)}} \quad (2.38)$$

The equivalent standard deviation of the wake $\sigma_{eq} = \sqrt{\sigma_y \sigma_z}$, σ_y, σ_z are the standard deviations of the two-dimensional multivariate Gaussian distribution fitted to the wake velocity deficit in the span-wise and wall-normal directions respectively. Where the equivalent standard deviation is increased with the rotor downwind distance. from the above, considering a two-dimensional Gaussian shape for the wake, the velocity deficit is:

$$\frac{\Delta U}{U_\infty} = \frac{\Delta U_{max}}{U_\infty} \times \exp\left(-\frac{1}{2}\left[\frac{(z - z_h)^2}{\sigma_z^2} + \left(\frac{y}{\sigma_y}\right)^2\right]\right). \quad (2.39)$$

A similar approach has been used by the Bastankhah and Porté-Agel [6] which was presented above 2.2.8. They have derived an analytical wake model, for HAWT and assumed an axisymmetric Gaussian shape for the wake deficit, whereas the current approach assumes a two-dimensional multivariate Gaussian distribution.

An overview of the extra studies (literature review, programmed models for theoretical Wake Superposition Method based on Law of Conservation of Momentum) for wake superposition, where the wind profile and wake deficit behind a single wind turbine can be combined with a superposition method is presented in the AppendixA

2.3. A Survey on Simulating and Measuring the Wake of VAWTs

An ample amount of work in field-scale measurements, wind tunnel experiments, and numerical simulations have been done recently to study the wake aerodynamics of VAWT'S. An overview of the most recent experiments and studies related to the aerodynamics of the wake for VAWT is been provided. one of the first experimental studies on the wake downwind stream of VAWT were conducted by Brochier et al [11]. They used a model of straight-bladed VAWT and studied its wake characteristics using Laser Doppler Velocimeter (LDV) tests in a water channel. They focused on the dynamic stall and relating tip speed ratios (λ) Kinzel et al [24] found a high plan-form kinetic energy flux that advocates the recovery of the wake: in arrays of real-scaled VAWT's. They analyzed wake flow within these arrays by computing the mean and turbulent kinetic energy flux. A full-scale straight blade wind turbine was analyzed for power performance and wake properties by Li et al [27] their findings showed the recovery process in the wake region to be asymmetric.

A near wake study using a Darrieus-type wind turbine was conducted in wind tunnel experiments by Bergeles et al [38]. For different tip speed ratios λ_R They outlined mean velocity and turbulence level profiles at two downstream/rotor behind positions. It was reported, wake deflects slightly towards the direction of rotation and the turbulence level is larger near the edges of the wake. The mean shear is stronger at the edges than compared to the center of the wake. Battisti et al [8] conducted wind tunnel experiments to study the wake behind a VAWT (tip-speed $\lambda_R= 1.6$ and 2.5). They reported that the wake appears to be asymmetric and deflected due to the rotation of the blades. They demonstrated that this phenomenon is due to the blade-tip vortex interactions that are stronger in the region of upcoming blades than in the region of retreating ones. They also showed that for higher tip speed ratios the wake deflection is been reduced, as the flow recognizes the turbine rotor as a porous cylinder, with symmetric deflection of the wake. Araya and Dabiri [4] used PIV to study the wake of rotors with different blade numbers. They explained that the far wake region of VAWT and a circular cylinder of the same aspect ratio demonstrates wake characteristic that is quantitatively the same. Where Rolin and Porté-Agel[37] used PIV experimentation with two counter-rotating vortex pair behind a VAWT, which leads to higher turbulent momentum flux into the wake. Near wake of VAWT's were studied by Kadum et al[27] with a PIV and wind tunnel experiments. They reported asymmetric behavior of both first and second-order moments of the wake downstream.

Besides wind tunnel experiments, some numerical methods and simulations have also been deployed to investigate the wakes for VAWT's. For the first time, Shamsoddin and Porté-Agel [38] used large-eddy simulations (LES), to simulate wake downstream of the VAWT's. The reporting from their study were concrete predictions of the mean and higher-order statistics for the wake of VAWT's when they used a combination of LES coupled with the actuator-line model. Hezaveh et al [15] Using Large Eddy Simulations (LES) investigated the effect of turbine solidity, aspect ratio (H/D) and tip-speed ratio λ_R on the downstream wake of an isolated VAWT. While Abkar and Dabiri [1] used LES to explore the wake over the VAWTs and found that the wake has self-similar properties after some distance downstream. while Abkar [1] use the same concept of mass continuity and momentum balance similar to the self-similar Gaussian shape velocity deficit model by Bastankhah and Porté-Agel [6], for VAWT's. They compared the newly developed theoretical model to large eddy simulation as well as field measurement data of vertical axis wind turbine wakes. The reporting was the Gaussian-based wake model was more accurate with the field results and LES data than other theoretical counterparts. Mendoza et al [31] simulated the near-wake flow of a VAWT's using an actuator line technique. They showed that the actuator line model is able to characterize the main features of the wake flow downwind of the turbine. whereas Lam and Peng [22] used a blade-resolving numerical technique to study the near and far-wake regions of a straight-bladed VAWT. They showed that the asymmetry of the wake increases as the wake follows downstream.

Here we can identify two main approaches used to simulate the flow field through VAWT's. one where the boundary layer flow around the turbine blades are resolved. Where detailed information about turbine loading and near wake characteristics can be obtained. second based on actuator type technique, which removes the need for resolving the boundary layer flow around the blades. Thus significantly reducing the additional computational cost and necessities compared to full-scale blade

resolving simulations. However, some perceived disadvantage of both approaches is increased computational complexity which prevents its use to study the wake flow in the real-time environment. Whereas for the actuator-based technique its performance is sensitive to the aerodynamic input data of the blades and the concrete reliability of that data is questionable. All the above-reported studies have provided valuable insights into the interaction between the incoming flow and the vertical axis rotor including wake flow characteristics, aerodynamic loads on the blades, and structural fatigue due to dynamic stall and blade-wake interactions.

The present work aims to investigate and realize the structure of wake behind a VAWT and different accommodation of pitch angles for VAWT rotors. In this framework, the theoretical model's wake (Wake model for VAWT by Mahind Abkar [1], selected) is used to recreate the wake flow characteristics and compared against PIV experimentation and CFD simulations. The experiments are designed at the OJF wind tunnel at TU Delft.

3

Experiment apparatus and setup

In this chapter, the setup regarding the performed experiment and the associated testing procedures are going to be discussed. In particular, the attention will be drawn towards the setup implementation steps and the associated challenges together with relevant feasibility and time constraints. The intent is to focus on the sub-assembly components that assisted in making the whole experimental setup successful.

Building the overall setup requires cooperation and interface between different equipment, sub-assemblies, and resources. For example coordination of force balance assembly 3.2 with the manufactured vertical axis rotors for the force measurement techniques; making the rotor design with fewer possible vibrations 3.3.1; Understanding the stereoscopic PIV principles and preparing the PIV setup 3.5.1; Movement of the whole experimental setup with respect to the rotors by means of the transverse system 3.6; Phase lock measurement techniques 3.6.3. Moreover, a careful testing procedure is required for data accuracy and an involved safety factor.

3.1. Open Jet Facility

The experiments have been conducted in the Open-Jet Facility (OJF), High-speed lab at the Aerospace Engineering Department of TU Delft. OJF at Tu Delft is an impressive facility with a height of 8 meters and a width of 13 meters. The wind tunnel has an octagonal test outlet with a contraction ratio of 3:1 for an equivalent diameter of 3 m and, delivering a uniform flow stream with approximately 0.5% turbulent intensity at the near region from the jet exit. The flow stream in the OJF is driven by a large fan that is pro-pulsed by a 500KW electric engine and can achieve a maximum velocity of 34 m/s. Also the free-stream area contracts with a 4.75° semi-angle along the length of the jet, because of developing a jet shear layer at this test section [28]. After this test section, the flow passes a long diffuser and is guided by two rows of corner vanes such that it is rotated by 180 degrees. The flow enters a second, short diffuser, in which a wire mesh prevents flow separation. In the settling chamber, the flow passes several dense wire meshes that reduce velocity deviations and turbulence in the flow: Via a contraction, a smooth flow is then blown into the open test section. To compensate for the added heat in the flow, the flow is cooled by a 350KW immensely big radiator at the end of the test section: and the flow temperature is kept constant at $20^\circ C$ [25]. Finally, before entering the fan, the flow is redirected 180 degrees again by two rows of corner vanes. The settling chambers were also used to accommodate the aero-sole particle seeder so that the flow gets a uniform distribution of the aero-sole particle as to trace the lasers during the experiment. The Use of a blue table was done in the OJF to fix the experimental setup in-order to encounter the blockage issue. The blue table was fixed such that it aligned with the lower edge of the OJF hexagonal tunnel opening. The details of the blue table setup are explained in appendix A.6.

3.2. Force Balance

3.2.1. Design

A substantial part of the innovative work involved in this project was in the design, fabrication, and assembly of a three-component external platform force balance system. Which was capable of measuring the small aerodynamic loads (drag and lift force) on the rotor design. The force balance with the attached VAWT rotor for load measurement is shown in the figure 3.1. The concept for the force balance system was derived from the works of Gavin Kumar and Ananda Krishnan [14].



Figure 3.1: Force balance with VAWT setup

Design 1.0

For the whole force balance system, a number of iterations were performed in order to achieve an efficient, reliable, and economical balance. The figure below shows the development of the concept behind the force balance as this was one of the closest designs to the final balance. The fabrication and working of the final system are based on the working concept shown in the figure 3.2. This balanced design consists of two parallel mounted platforms that allowed it to measure principally lift and drag forces on the rotor structure. Each platform used eight double-ended flexural pivot bearings. These flex-pivots are one of the main components of this particular balance design. They ensure that the balance reacts similarly in all principal directions without any hysteresis also, they are stiction-free and allow movement only in a single direction.

As it can be clearly seen from the isometric CAD diagram 3.1, the lift platform was mounted on the base platform, and the drag platform was suspended within the lift platform. The flex-pivots here restricts the moment of a platform in only one direction (as shown with the red mark the moment of both platform in one direction and perpendicular to each other). Both platforms were connected to the load cells, hence this arrangement allows a measure of lift and drag forces on the rotor structure. The mounting brackets shown in the corners were introduced to accept different load cell attachment

points to allow variations in the operational range of the lift and drag platforms. Also to ensure that the load cells were always working in tension for accuracy and calibration, pre-loading is done via the pre-loading brackets. The working concept behind the following design was adopted from an experiment for the aerodynamic performance of low to moderate aspect ratio wings at low Reynolds's number at the University of Illinois at Urbana-Champaign, by Gavin Kumar and Ananda Krishnan [14]. While the specifics of designing and accommodation of the balance as per the requirements for this project were made in-house.

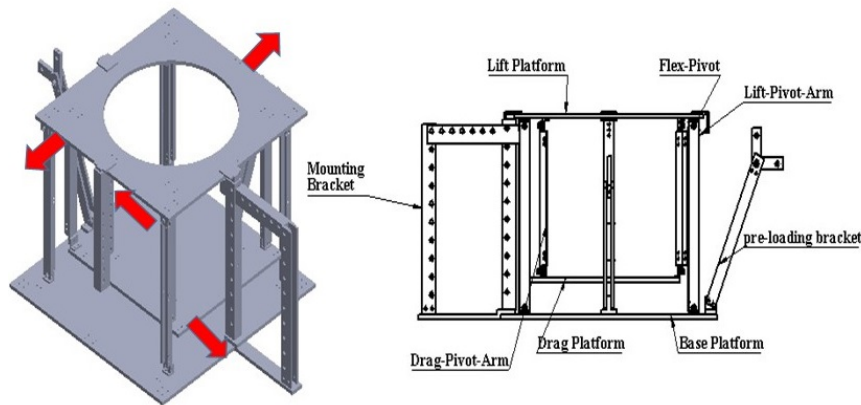


Figure 3.2: Working Concept of force Balance

Design 2.0

The final design 2.0 of the Balance was an optimized version of the previous design 1.0. Here certain aspects of the previous version were reduced to make it cleaner, sensitive, and efficient. The load cell brackets were replaced for directly fixing the load cells to the base plate. This also reduced the Pre-loading brackets and their components. The concept of two platforms was minimized to a single base platform design, which now makes no longer use of the flexural pivots. Also, the flexural pivots were replaced by the Flexure-rods fabricated using titanium. They have a similar function to the flexural pivots.

The added use of sensitive titanium flexural rods makes the balance more reliable and accurate. These rods have one end attached to the load cells and the other to a fixed bracket on the base plate. The load cells are attached to the fixed frame of the balance. The base plate is suspended within the frame using four guide wires one at each corner, further, the VAWT is fixed on this base plate using Allen screws. The three-component balance use, Two load cells with a parallel configuration and equal distance from the frame and one load cell perpendicular to these two load cells. This arrangement is such that the clockwise rotating moment of the rotor with the blades turning in, aligning it selves to the two parallel load cells. This parallel configuration calculates the drag force on the rotor, whereas the third perpendicular load cell calculates the lift force. The highly sensitive flexural rods allow its movement only in one direction and are connected to the suspended base plate and load cells they determine the magnitude of the force on the rotor which is then calculated using the load cells.

3.2.2. Fabrication and Assembly

Most of the components for the force balance were fabricated at the demo workshop at TU Delft Aerospace department and assembled at the low-speed lab by ir.S.(Stefan) Bernardy. The concept and design started in December 2020 and were assembled and ready for the test, March 2021. Where a test run was conducted at the end of March to check the workings of the force balance. The Balance was specifically designed with ease of use for future projects, where different rotors can be easily mounted on the balance for force measurements. The assembly was designed to tolerance levels of ± 0.05 to ± 0.15 mm. This tolerance level ensures that assembly of the balance was performed with

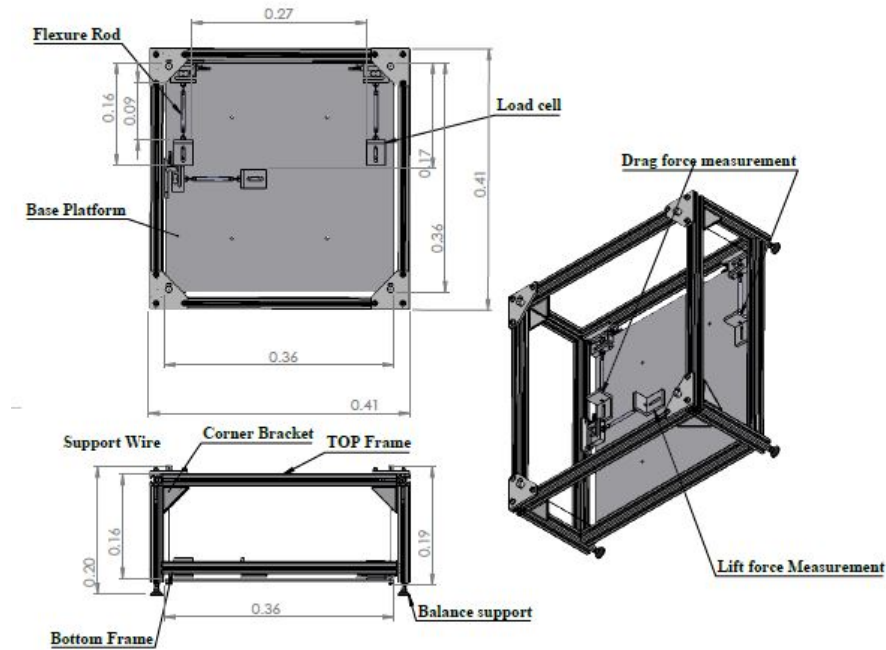


Figure 3.3: Force Balance CAD design with detailed specifications

minimal fitting issues. An isometric view of the CAD model and the design specifications of the constructed force balance is shown in figure 3.4, 3.3.

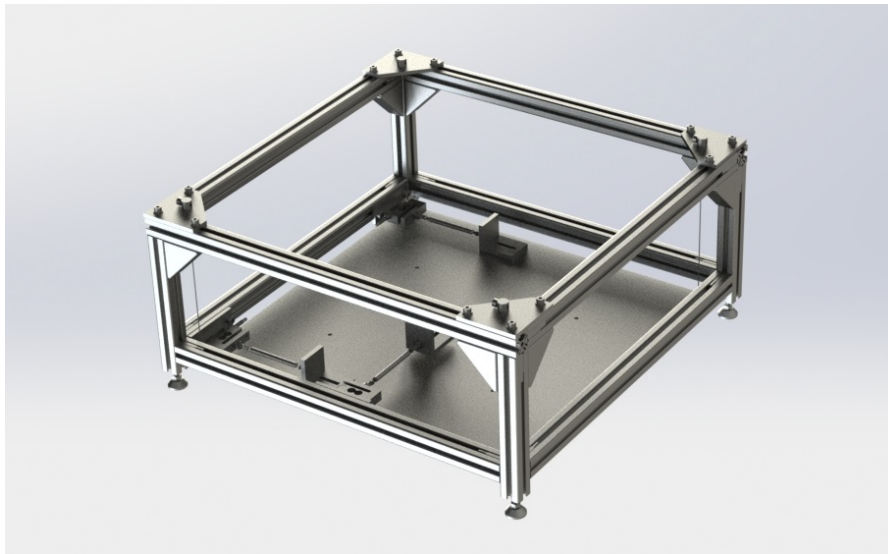


Figure 3.4: Fabricated Force Balance measurement device

The balance frame and base platform both are manufactured from mat steel metal, the guidewire and the load cell brackets are made from stainless steel whereas the balance support knuckle is hard rubber made. Also, as previously mentioned the flexural rods are fabricated using titanium. Totally three KD 40s compact load cells are used each measuring a force range till 50N, with a rated output of 0.5 mV/V and accuracy of 0.1%. The load cells are directly connected with the custom cable solution and minimal tools to the RJ50 jack of the NI 9237 module. A high-quality, high-speed strain/ load measuring system with zero inter-channel phase delay. The NI 9237 simultaneous bridge module in combination with the Compact DAQ chaise contains all the signal conditioning required to power

and measure up the load cells. The Compact DAQ is a portable, rugged data acquisition chassis that integrates connectivity, data acquisition, and signal conditioning into modular I/O for directly interfacing to the load cells. Secondly, using Compact DAQ with LabVIEW, the measurement data was easily acquired, analyzed, and managed also the visualization of the data through this process was easy to understand and study.

3.2.3. Alignment and Installation

The force balance was calibrated at the low-speed lab, TU Delft using a six-component force balance calibration device. Also, the LabVIEW software used was added, with a programming loop to ensure the accuracy and calibration of the balance before every set of measurement cases. The overall force balance is lightweight, less complex, highly reliable, and easy to assemble and install.

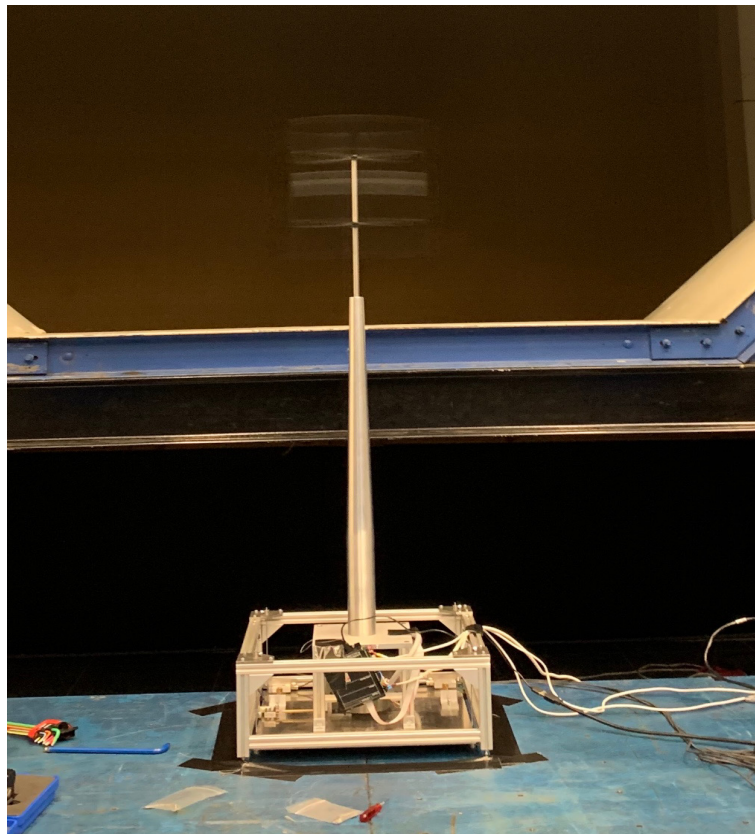


Figure 3.5: Alignment and working of force balance system

In order to keep the balance undisturbed from the inflow velocity of the wind in the OJF. The balance was covered using a low-cost, lightweight plywood box. The box was designed in such a way that it could accommodate all the connections and cables to and from the balance. Also, the box could be used as a protective balance carrying case for the future. Further, the balance with the box was set up on the blue table in OJF, where the box and balance both were fixed to the blue table and only moved for required measurement cases. This can be seen in the figure 3.5 for the balance setup.

3.3. H-type Vertical Axis Wind Turbine

In this section, the design and fabrication of the Vertical Axis Wind Turbine will be discussed briefly. The improvements in design to counter the vibration for the rotor and how they were solved, Also the passive pitch deflection, to change the angle of attack on the blades will be discussed here.

3.3.1. Design

The VAWT model has two blades, and two supporting struts with a profile of NACA0012. The length of the blade is 300 mm, and the rotor diameter is 300 mm. The model is driven by a DC brush-less combination motor, 260 W with a hall sensor by the Maxon group. The rotating shaft used is 1.10 meters long and 0.01 meters in diameter. The base platform was designed to accommodate the generator, the EPOS4 Compact positioning controller, the magnetic sensor, and cables with a height of 0.16 m and width of 0.17 m. The whole structure is 1.10 m tall. Designing the structure with minimal vibrations and fluctuations was a prime and important task: so that the forces calculated on the structure were accurate and also, considering the safety factor for the structure. The details regarding the VAWT are presented in the table below 3.1. The details specifications and working for the DC brush-less combination motor and the EPOS4 Compact positioning controller are in the following document [35].

The improved structure was based on previously designed for VAWT by (Ming Huang [16]) and the modifications to the whole structural design were made in solidworks designing software. Also, the structure was made sure to be gyroscopically stable. Certain important additions were made to the design to make it more stable and reduce the vibrations on the rotor. A tubular shaft cover made of steel with dimensions of 0.70 m tall and 0.05 m thick was introduced with two bearing groves at the top and bottom of this tube, which was fixed to the bottom platform. The tubular shaft cover acts as a more stable and robust supporting structure to the rotating shaft, which reduces the overall vibrations on the rotor and a smooth operation for the rotation movement. A bellow coupling was also used to reduce the misalignment factor in the rotating shaft and the motor which further again reduced the vibration of the structure. A set of design provisions were made on the structural assembly to accommodate the electronics and its cabling constraints. The CAD design along with the bill of materials for the VAWT design can be seen in the figure 3.6.

VAWT specifications	
Property	Dimensions
Number of blades	2
Blade length	300 mm
Rotor diameter	300 mm
Blade profile	NACA0012
Chord blade	3 mm
Strut profile	NACA0012
Chord strut	3 mm
Tip-speed ratio	2.513

Table 3.1: Turbine Specifications.

3.3.2. Fabrication and Assembly

Similar to the balance force balance the VAWT parts were made at the demo workshop aerospace department TU Delft. The assembly was done at the workshop in low-speed lab aerospace TU Delft. The material used in the fabrication of the parts is stainless steel. The figure 3.7 shown below is the assembled VAWT. A black 3D printed shaft cover was manufactured at the low-speed lab in order to cover the shaft, which was attached to the balance box. The function of the 3D printed cover was to further reduce the vibrations on the tower of the VAWT structure and a string was attached in circular loops on the cover so that the vortex shed by the tubular tower can be dissociated/ reduced. The black 3D printed cover also helped in lowering the reflections of the tower in PIV experiments. The CAD file for the 3D printed cover is in the appendix A.5.

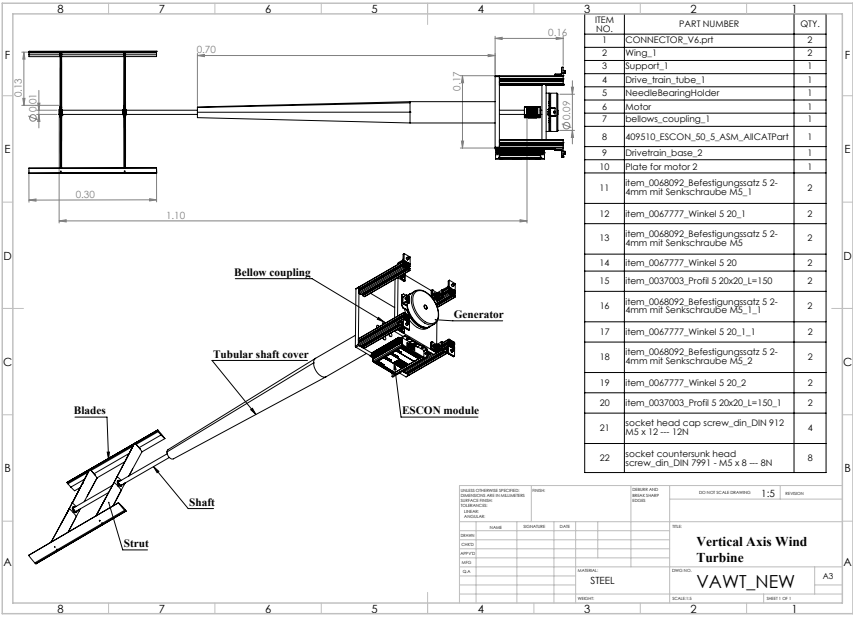


Figure 3.6: Detailed CAD drawing of Vertical Axis Wind Turbine design

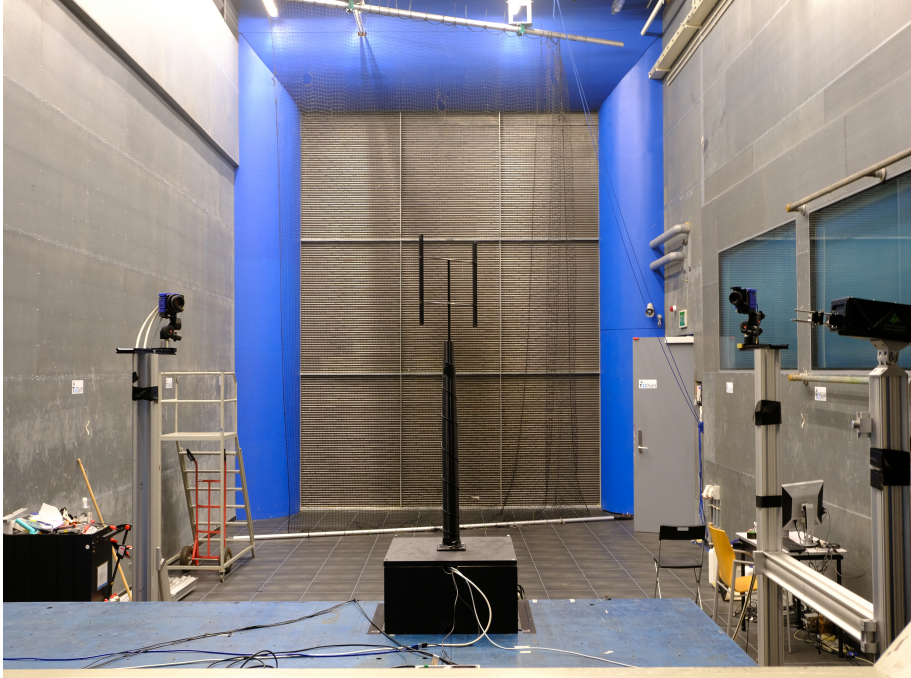


Figure 3.7: Fabrication, setup and working of VAWT rotor in OJF

3.4. Particle Image Velocimetry

In this subsection, the theoretical basics necessary to understand and then implement for experimental campaigns will be discussed. As the main aim of the experiments is to study the wake flow field measurements of the scaled VAWT, the principles of Particle Image Velocimetry are firstly introduced 3.4

Particle Image Velocimetry (PIV) is an optical, non-intrusive method that is related to both, flow visualisation and optical point technique, that can provide a whole quantitative velocity measurement for both its uncertainty and instantaneous flow: by acquiring subsequent frames of illuminated flow particles. The flow contains tiny seeded, neutrally buoyant particles called traces (Seeding particles are injected). The area of interest is called FOV (Field Of View), which is illuminated using a light sheet, formed by passing a double pulse laser beam (ex-Double pulse NDYAG system used in this experimentation). The laser is focused optimally using the cylindrical lenses so that the particles in the flow are illuminated twice with a small time lag. For both occurrences of the laser pulse with a short time delay, the particle position at these two different frames is recorded by using a CCD camera. The particle displacement from one frame two to the second is measured locally across the FOV, and the velocity field is obtained by dividing the displacement with the known time lag between the two laser pulses. The magnification factor for the lenses of the camera is also taken into consideration. Based on the flow velocity and the camera, lens magnification factors the DAVIS system adjusts the time delay between the two laser pulses, and an accurate displacement of the particles and the velocity vector can be calculated.

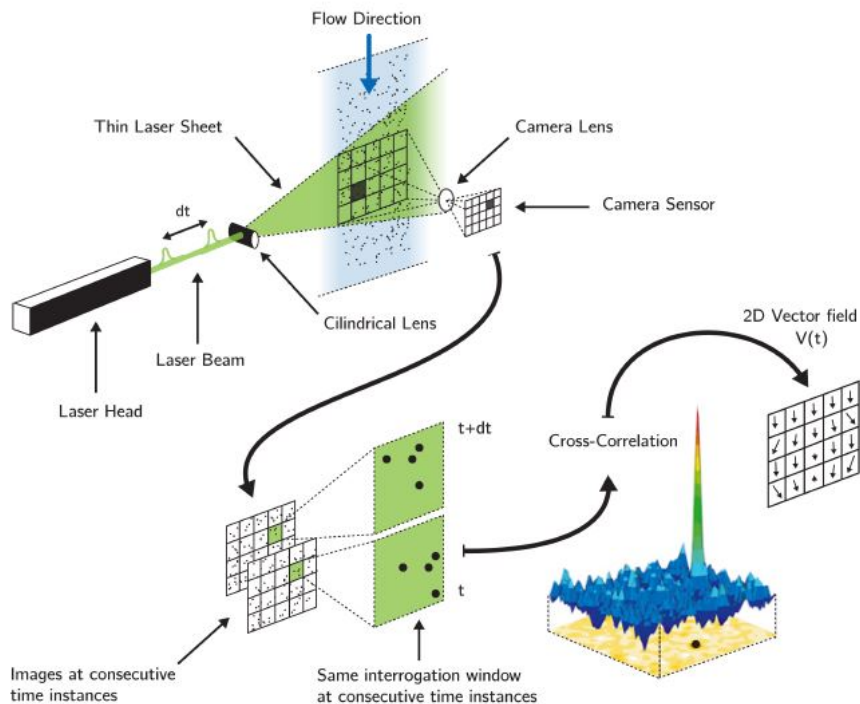


Figure 3.8: Stereoscopic PIV working principled and concept [19]

To study the particle image, trace particles follow a local flow velocity, in the flow between the two illuminations. The (digital) PIV recording is divided into small subareas called ‘interrogation windows’, and a statistical correlation technique is used to determine a local displacement vector for every interrogation window, further explained in more detail. So a small size for this interrogation window is selected such that all particles within this area have moved homogeneously in the same direction and the same distance. This is a cross-correlation technique also called : (double frame/ double exposure)

used in the experiment.

As mentioned above the light scattered by the trace particles during first and second exposure is recorded in two separate frames, where two frames combine to complete an image. These frames have a subdivision of interrogation windows as explained before, where every interrogation window is evaluated by cross-correlation of the window in frame 1 recorded at time instant t with the same window in frame 2 recorded at time instant $t + dt$. For recording this a fast double shutter CCD Camera with double exposure was used in the experiment, details of which are listed in subsection 3.5. The time delay between the two laser pulses and the time necessary for the frame transfer of the camera is synchronized by the DAVIS system used as a data acquisition in the experiment.

Stereoscopic PIV

As studied from the previous experiments from [17], the computation of the VAWT wake through a controlled volume approach requires evaluating the wake velocity deficit in the stream-wise direction. In the classical planar PIV arrangement, only one camera is employed. The camera viewing axis is orthogonal to the laser plane and the technique aims at measuring the in-plane projection of the velocity flow field. As the field of view is two-dimensional and only two components of the velocity vector are obtained. A planar PIV wake analysis of the VAWT with a plane aligned to the turbine center-line is not sufficient to capture the out-of-the-plane velocity deficit. Hence a different approach of PIV measurement technique called stereoscopic-PIV is implemented for the experiment. The stereoscopic-PIV recovers the complete set of velocity components, with an additional PIV recording from a different viewing axis using a second camera. Using these two different viewing angles one can easily obtain projections of the velocity vector in two planes. The viewing directions of both cameras with respect to the orientation of the light sheet position and their calibration is an important parameter. Once the arrangement of both cameras is fixed, all three velocity components can be measured on a two-dimensional domain by using the stereoscopic-PIV.

Camera arrangement: Based on the PIV experimental setup and arrangement a backward forward scattering camera arrangement was adopted for the experiments. Also, this camera arrangement is easier to calibrate. In this case, both cameras are mounted on the same side of the light sheet. The calibration was done with a two-level calibration plate. One of the cameras is recording the light scattered in forward direction while the other camera is recording the scattered light in the backward direction. A larger aperture is used in this case as the intensities detected by both cameras with the same f-number of the camera lens are different (typically a factor 10 between backward and forward direction) [19].

Scheimpflug condition: According to the Scheimpflug criterion, the image plane, the lens plane and the object plane has to intersect in a common line for each camera, this is adopted to increase the measurement precision of the out of the plane component, which also increases with the angle between the viewing directions of the two cameras. If the angle between the viewing direction is 90° degrees the precision for measurement in in-plane and out-plane is the same. But, the problem lies in the depth of field for the oblique viewing direction, which can be rectified by additionally tilting the image plane in respect to the camera lens and light-sheet this is accomplished by using a Scheimpflug adapter. Unfortunately, this arrangement has the side effect of introducing a strong perspective distortion. The factor of magnification is no longer constant across the complete field of view and needs additional calibration [18].

Calibration: The two cameras need to be good calibrated in a Stereoscopic PIV. Correcting for off-axis viewing is important for reliable results. The Davis system has a full empirical calibration method, which does not require a need to measure angle and distances. For calibration of stereoscopic systems a LaVision two-level calibration plates with defined separation of the calibration planes and mark spacing were used. The plate Type is printed on the bottom right of the front side of the plate and can be selected in the software. The software pre-select all the essential parameters. The cameras, in synchronization with the Scheimpflug adapter, is used to focus the calibration plate by maximizing the overlap areas of both cameras. Full detail on calibration is provided in the Davis Imaging Tools manual [18].

3.5. Experiment Setup

The stereoscopic PIV experiment was only possible with the construction of the experimental setup to assist it. Its main objective consists of reconstructing the velocity field by capturing the full wake velocity deficits downwind of the turbine. For this to succeed a numerous factors and construction arrangements were required which are explicitly described in the following subsection.

A basic setup of the PIV experiment can be seen in the figure 3.9, where a setup of the cameras and laser arrangement is shown. VAWT rotor is close to the opening face of the wind tunnel, whereas the camera holding the X-beam structure was 2.3 m with respect to the rotor. The position of the VAWT rotor was fixed at all instances and only the pitch angles on the rotor were changed according to the need of measurement cases planned. By aligning the cameras with a FOV of 800 mm \times 500 mm with the object distance of 2.34m and magnification of 0.001% with respect to the turbine. By considering both solid and wake blockage (Barlow et al., 1999) for the rotor configuration, the largest overall blockage in such a tunnel is less than 4% in the current experiment. With the blockage factor into consideration, the rotor was adjusted to a height such that the center of the rotors be almost aligned to the center of the opening face of the wind tunnel. This arrangement gave a more ideal wake expansion and correct capture of velocity deficit during PIV, with the lowest probability of wake coming closer to the ground till ten rotor diameters from the first turbine.

There are four major constraints to look at the setup first being the positioning of the VAWT's, second the arrangement of the cameras and laser to move coherently, third correct positioning and mounting of the laser with respect to the cameras and turbines, and finally the data collection of the PIV experiment. The positing of the VAWT'S with respect to X-beam has been discussed above, whereas the VAWT is fixed on the blue table at OJF and the blue table is further used to adjust the height constraints of the turbine, (in certain far wake cases the table was been lowered so that the wake was correctly captured by the cameras). For the movement of the cameras cohesively with the laser to capture the wake velocity field at different downstream positions ($x/D= 1,2,3,4,5,6,7,8,9,10$) a transverse system was used, this transverse system at OJF TU Delft was attached with a design of X beams construction on it. The transverse could hold the whole x-beam design (U-shaped x-beam structure) as seen in the figure 3.9 and with a controlled program of transverse, the structure could be accurately moved at different distances in a direction perpendicular to the face of the wind tunnel (rotor downwind direction). For the laser to move in coordination with the cameras a special type of attachment of ball-bearing and plate was designed and fabricated at high-speed lab Aerospace Tu Delft. This fabricated ball-bearing part was mounted on an x-beam and attached to the main (u-frame) made of X-beam to the transverse system, further the laser was mounted on the x beam as seen in the figure 3.9 using a fixed mount structure. When there was a moment of transverse by the trans-version system the ball-bearing part and with it, the X-beam and laser were pulled in the direction of the transverse. The detailed design of the ball-bearing part can be seen in the appendix A.7. Also, the attached laser arrangement helped us to track the rotor downwind position (X/D), which is described further in the PIV setup. The X-beam structure separates the cameras with a distance of 3m and positions them at an angle of 45 degrees. The height of the cameras, set up on the X-beam are specifically chosen as the same as the center of the VAWTs. The distance between the cameras and the center of the rotor was chosen to be 2.2 m.

Finally, the data acquisition was done with a PC-B PIV processing unit, the synchronization of the laser unit with the cameras and the transverse system has been explained in the next subsection 3.5.1 this was controlled by PTU (Programmable Timing Unit). The PTU and the PC-B were connected to the cameras and laser and fixed to the transverse system. The processing and movement of all the working equipment are even the start and stop of the rotors were controlled remotely through the monitoring room of OJF. To ease the working and for safety and precautions, a small test run was conducted from monitoring room before every case and change of position, so the data would be reliable and with minimal discrepancies. Some reflection problems through the opposites wall to the laser were countered by adjusting black screens to reduce the reflection.

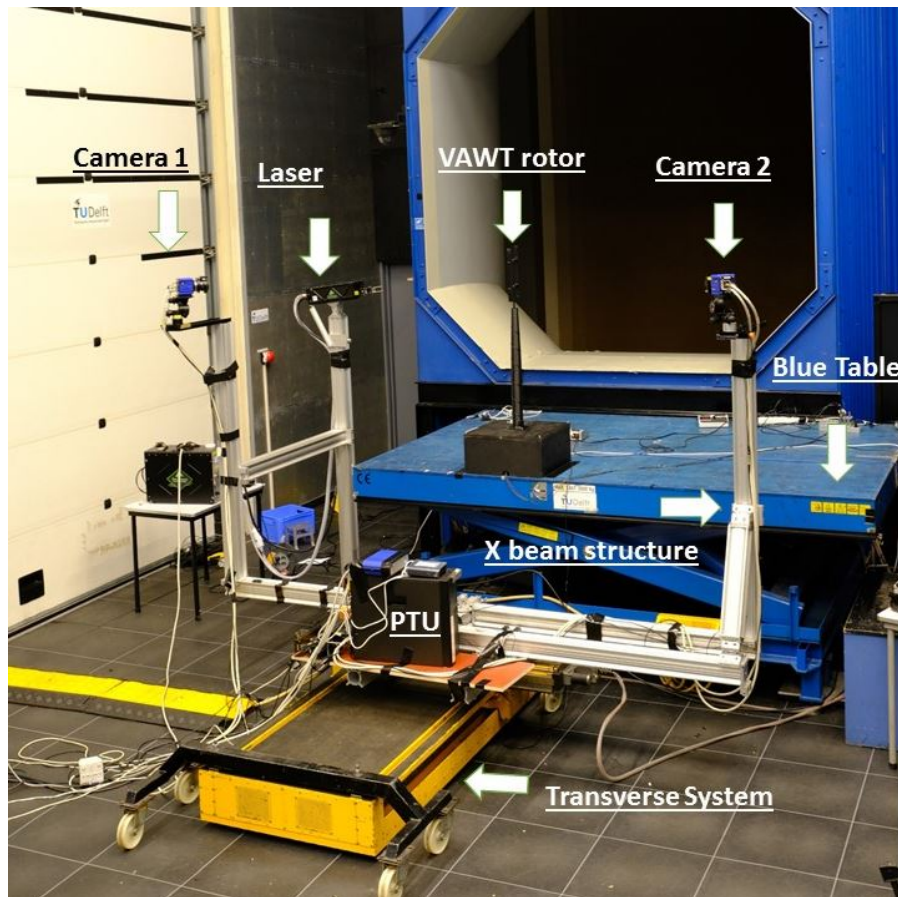


Figure 3.9: Stereoscopic PIV setup at OJF TU Delft

3.5.1. PIV Setup

The Stereoscopic PIV experiments were conducted, where three velocity fields components are mapping for the rotor wake; results are obtained via an average of the vector fields. The stereoscopic PIV set-up was installed on a traversing system able to scan the flow field in the wake for the stream-wise direction of the VAWT wake, as shown and explained in the figure 3.9. A field of view (FOV) with 800mm width and 500mm height was considered. The dimension of the field of view was chosen based on iterations and previous experiments [17].

In the stereo-PIV setup, two low-speed cameras were used specifications sCMOS camera [19] a 16-bit, double shutter (120ns) capable of acquiring images up to a frequency of 50 Hz. The camera has a sensor size of 2560×2160 pixels and a pixel pitch of $6.5\mu\text{m}$. Each of the camera was mounted with a AF Nikon lens with a focal length of ($f=180\text{ mm}$) at a magnification M of 0.10. Sheimpflug adapters were also used to align the three planes (image, lens, and object plane). Both the cameras were positioned at a height aligning the centers of the rotor of VAWT, were separated with a distance of 3 m and positioned at an angle of 45° .

The experimental light source was a Quantel Evergreen 200 laser, with maximum pulse energy of 200mJ and pulse width of 7ns 180mJ a double pulse NDYAG system. The wavelength of the laser was 532nm and it pulsed at a rate of 15Hz maximum [28]. The laser was positioned laterally at 3 rotor diameter from the turbine center axis and the beam was aligned with a laser sheet such that the beam coincided with a perfect mark of 5 rotors downwind distance from the fixed position of the VAWT rotor. This not only helped in illumination but also to track the projection distance in rotor downwind direction (X/D). The laser sheet thickness was chosen based on the possibility to capture a large depth of flow field and also to increase the seeding density. (The laser light is conveyed to a 2 mm laser sheet of

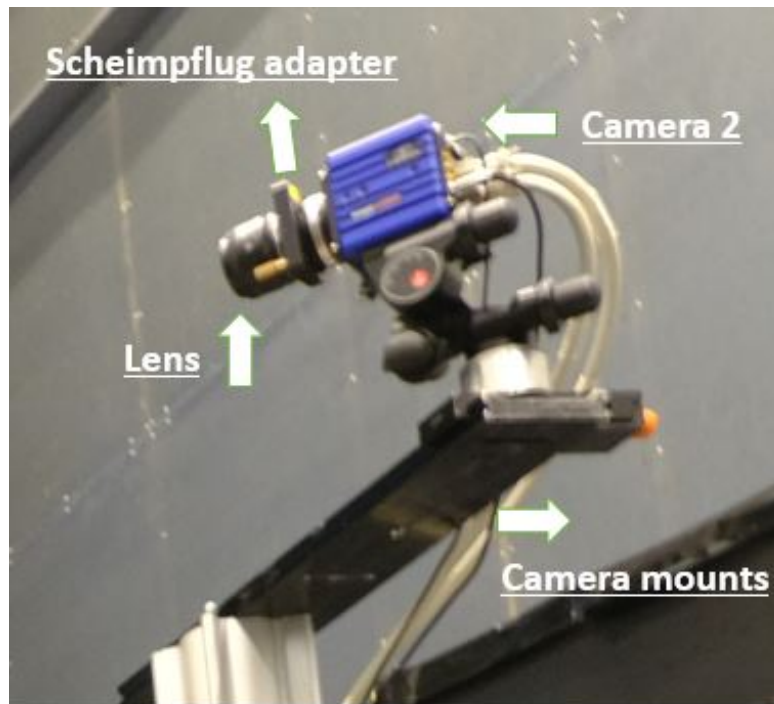


Figure 3.10: Camera with set of adapters and mount

about 0.40 m widths at the field of view, by a combination of a spherical lens and two cylindrical lenses). The laser was mounted on a special design attachment (roller attachment) explained above, so that the cameras and laser as a complete assembly could move together. Laser and camera synchronization was achieved through a Programmable Timing Unit (PTU) of LaVision, The frequent adopted for the entire experiments and the system to perform perfectly were assembled average of 15 HZ. Except in the phase lock experiments where the frequency of the system got adopted to the rotation of the turbine 13.33 Hz this was triggered using the trigger box developed at TU Delft, aerospace. The acquisition software was Davis 8.1.2, and a total of 300 images were shot at every single case and position to get the correct wake velocity field (L.E.M. Lignarolo et al., 2014) while the post processing software was Davis 8.5.10 and Davis 10.0.5.

Image specifications	
Property	Dimensions
FOV field of view	800 mm × 500 mm
Camera angle	45 degree
Sensor	2560 × 2160 pixels
pixel size	6.5 μ m
Focal length lens	180 mm
Lens aperture	f# 2.8-4
Magnification factor	0.001%
Acquisition Frequency	15 Hz
pulse time interval	3 ms
Camera time interval	10 ms
Rotation frequency of rotor	13.33 Hz

Table 3.2: Image specifications

Cameras and lasers were used to visualize the particles in the flow to retrieve the velocity field. Seeding particles were injected in the test section with a SAFEX smoke generator employing a SAFEX MIX, able to produce liquid droplets of less than 1 mm. Trace particles were produced using a single

entry seeder. A preview of the experimental campaign can be seen in figure 3.11

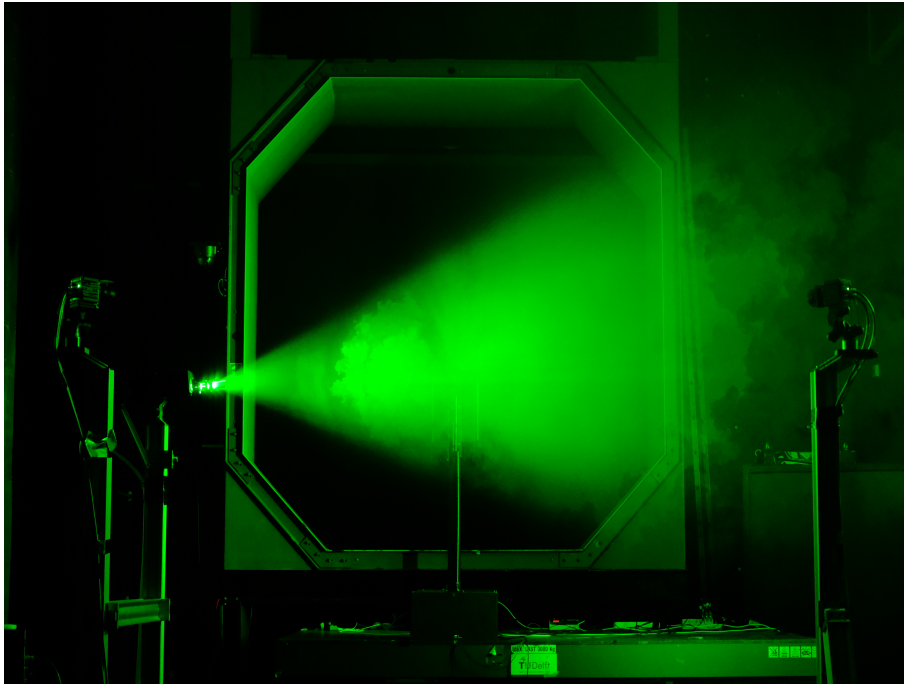


Figure 3.11: A preview from experimental campaign

3.6. Measurement Techniques

3.6.1. Force Balance

The force balance constructed above 3.2.2 to measure the drag and lift forces on the VAWT structure was put into action at this point. The measurement data acquired through the load cells via compact DAQ chassis and was stored using the LabVIEW software. Here 2 of the load cells measured the drag forces and a single for the lift measurements, the total drag is the product sum of these individual readings.

Figure (a) 3.12 shows the fluctuations in the calculated drag and lift measurement, this measurement measures both the forces for a time period of 9 seconds, The drag force varies in the limits of 1 and 0.9 whereas the lift fluctuates in between 0.2 and 0.1. The same figure shows the measured forces for about 120 revolutions, ie (9 seconds, 13.33 revolutions per second). Both the forces are shown negative because of the positioning of the load cell sensors in the force balance, and also due to the rotation of the vertical axis rotor in the clockwise direction (having a pull force generated). Averaging these forces over the time period of 9 seconds the following values are obtained: Drag force of 0.9410 N and lift force of 0.1388 N. Whereas figure (b) 3.12 shows a moving average of the same forces over a period of 1 second, this moving average removes the fluctuations and show a clear picture of force change over a time period.

With the calculation of the forces on the turbine structure, the drag and lift coefficients are also calculated using the following equation:

$$C_T = \frac{T}{0.5 * \rho * V^2 * A}, \quad (3.1)$$

Where C_T = Thrust coefficient, C_D = Drag coefficient, T= measured Thrust force, T_D =measured Drag force, V= free stream velocity, A= area covered by the rotor. The Drag coefficient is calculated to be 0.6828 and the lift coefficient to be 0.1007. The figure below 3.13 shows the change in Drag and lift

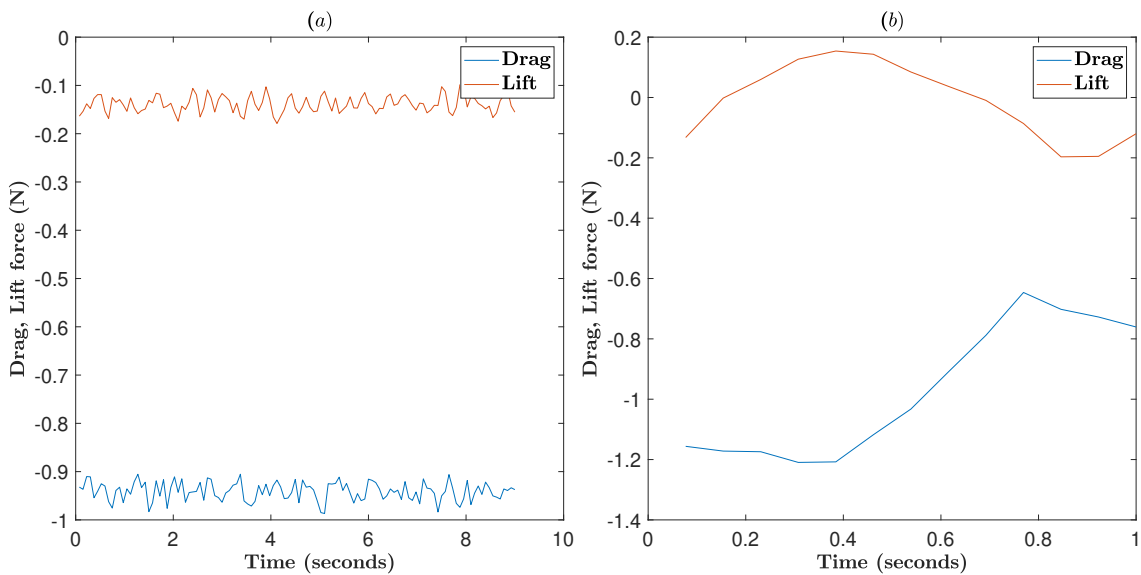


Figure 3.12: Drag, Lift forces vs time period, (a) a time period of 10 seconds, (b) moving average of the same forces over a time period of 1 second

forces over one revolution, it starts at rotor 0 degrees (rotor axis perpendicular to the wind flow). As it can be observed drag is dominated in most of the regions also lift is strong in opposite to drag regions. Similar Drag and lift forces were measured for positive 10-degree pitch angle cases 1.03154 N, 0.6144 N respectively. Drag force coefficient of 0.7513 and lift force coefficient of 0.4436. For the negative 10 degrees pitch angle case the forces were measured to be 0.8119 N drag force and 0.1252 N lift force, whereas the drag force coefficient was 0.5891 and lift force coefficient of 0.0909 respectively. With the increase in pitch angle of 10 degrees the angle of attack is increased by greater amounts, thus resulting a higher drag force and its coefficient on the structure of rotor (a condition similar to stall is developed) and similarly visa-versa for the negative pitch angle the resultant forces are reduced. The calculated drag forces and lift forces and their coefficients for pitch angle cases can be found in the appendix A.4.

3.6.2. Data Acquisition System

3.6.3. Phase-locked Acquisition for Wake Synchronisation

In order to visualize the spatial, temporal flow pattern of the resulting wake of scaled VAWT. To understand the interdependence between these flow patterns and identify the general structure of the resulting wake the phase-locking technique was employed. The data is recorded at a particular fixed rotating phase/position of the rotor using a trigger mechanism. The measured phases of the rotor are 0° , 45° , 90° , and 135° .

In order to acquire the correct wake flow field at a distance X/D after the rotor (rotor behind distance) in subsequent frames for the stereo-PIV measurements, synchronization between the accurate rotor position and the image acquisition is of primary importance to study the wake precisely. To achieve such synchronization, a trigger signal per revolution at an exact blade location is needed. Therefore, a through-beam magnetic sensor was developed. This sensor was attached to the VAWT frame using a L-bracket pointing inwards to the rotating shaft of the turbine. The lower naked part of the shaft where it has been attached to the generator using a coupler, a small light weight fiber disk is attached. This disk has been equipped with a thin magnetic strip, which is read by the magnetic sensor every time it passes over it and pulses of 5v are transmitted to the interface box. The interface box is designed at the TU Delft high-speed Aerodynamics department and connected to the PTU (Programming Time Unit) and acts as an external trigger, to locate the correct position of the turbine blades.

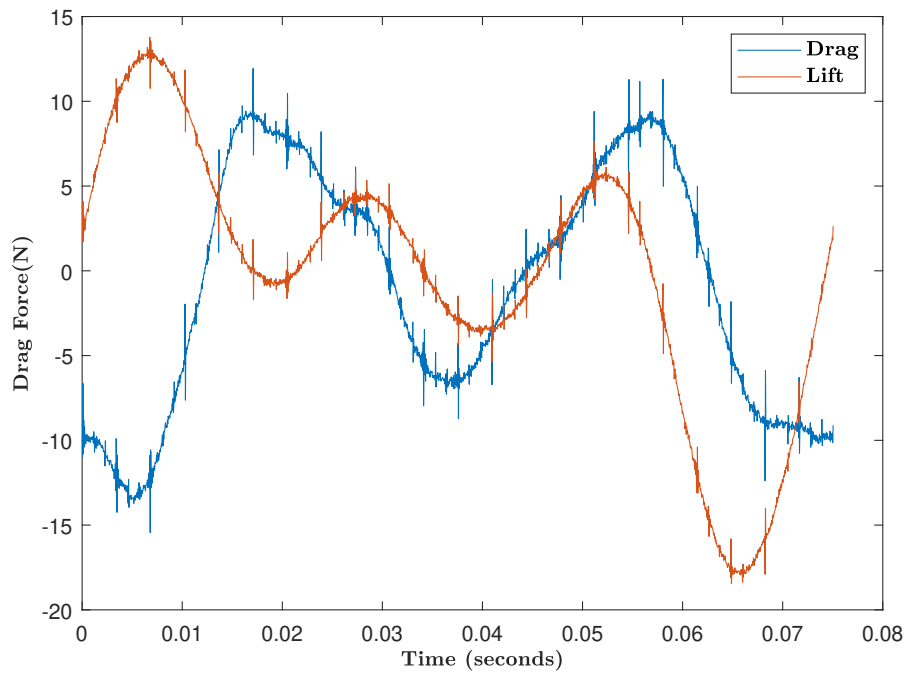


Figure 3.13: Variation of Lift and Drag forces over a single revolution

After studying the stereo-PIV measurements in the ring of fire experiment campaign [32]. Two different methods were evaluated for the use of trigger in the PIV image acquisition for the VAWT wake experimental campaign, hereafter referred to as mode 1 and mode 2. The differences are ascribed to the setting of the DaVis software and the hardware connection.

In mode 1, the interface box trigger signal is connected to start trigger connection of the PTU, through an internal cyclic mode. The signal is transmitted with the detection of the magnetic strip by the corresponding sensor and counted as a trigger. The working principle is illustrated with the comparison of two different test cases in the figure 3.14. The DaVis recording sequence was enabled by adding a loop for the limited number of images acquisition, and by synchronizing the camera and the rotor frequency. The time instant varies relative to the trigger reception shown as a red line. Images are overwritten on the RAM until the external trigger is received and images are stored shown in blue dot. The relative time difference between two tests for the same wake plane is limited by the chosen acquisition frequency. For this experiment, mode 1 a discrepancy was observed for the first trigger position for every different iteration conducted. It was thus difficult to locate the correct initial position of the rotor every time an iteration was conducted. If the original position of the rotor is not the same for different iterations then the experiment results would be invalid to study the wake flow field. Hence a new mode was selected as mode 2. Mode 1 was used in the static calibration of the experiment campaign conducted in Appendix A.2

In mode 2, the interface box signal is sent to the trigger port of the PTU using a trigger addition link. The image acquisition process in the recording sequence in DaVis is preceded by a flag enabled by the reception of the trigger. The trigger used is external with no added loops system. The latter is still the same single signal originated by the magnetic strip passing over the magnetic sensor. In this case, no image acquisition is performed before the received trigger and this should guarantee synchronization of the wake planes. This is shown in figure 3.15, if the angular velocity of the rotor is constant as well as the system delay. The delay between the rotor passing with the trigger activating and the effective beginning of the image acquisition was measured with a second test in a subsequent campaign, described in the Appendix A. The delay of the photoelectric sensor is less than 0.2 ms very small, hence neglected. If the delay is not constant, the synchronization between the trigger activating and the image acquisition is hampered by it. To quantify the system delay, an experiment campaign was carried out as elaborated in Appendix A.2. The acquired delay is further used to accurately predict the correct

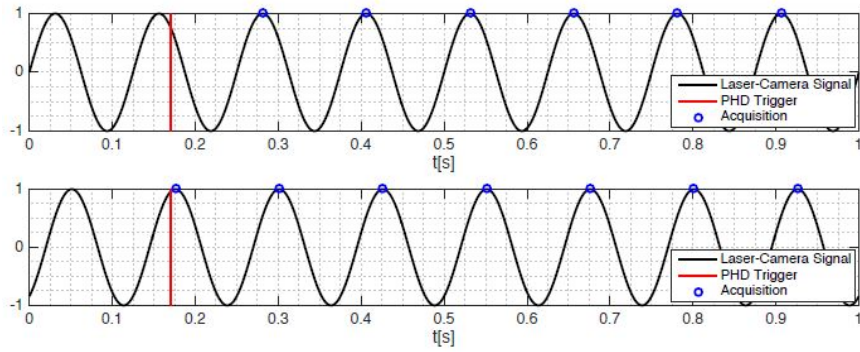


Figure 3.14: Trigger modes comparison: Mode 1 [32]

positioning of the rotor for every conducted iteration. By adding it to the DaVis software and using a set of developed equations the correct delay for image acquisition is calculated. Hence, Mode 2 was used for dynamic experiments.

To accurately predict the location of the rotor and change its position around, as per the experimental

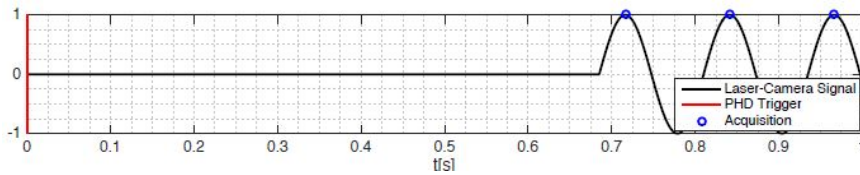


Figure 3.15: Trigger modes comparison: Mode 2 [32]

requirements: the following formulas are devised, Where $System_{delay}$ = system added delay is the required delay to be added in the system to achieve the desired position, T = time required for 1 revolution of the rotor. Δ_{Davis} = system delay for image acquisition.

$$System_{delay} = (T - \Delta_{Davis}) \quad (3.2)$$

Similarly for obtaining 90 degrees to the original position of rotor:

$$System_{delay} = \left(\frac{T}{4} - \Delta_{Davis}\right) \quad (3.3)$$

180 degrees to the original position of rotor:

$$System_{delay} = \left(\frac{T}{2} - \Delta_{Davis}\right) \quad (3.4)$$

3.6.4. Velocity Stream Measurements

In this subsection, a detailed overview of all the case description for wake velocity distribution captured at different (X/D) positions will be discussed in details. With this what were the different cases how were they achieved and how many planes of measurement data was collected through this experimental campaign and last but not least were we able to successfully complete the planned experimental campaign and all the cases decided.

A total of twelve cases were successfully achieved with reliable and good-quality data. With each case registering, measuring ten different planes, except for the phase lock measurements where twelve different planes were measured for each case. Summing up a total of 136 planes were measured for the free stream wake velocity. The measured planes started with planes downwind and upwind with respect to the rotor fixed position. All the measurements were observed by keeping the rotor position constant for every single case and all measuring distances and references were made with respect

to this fixed VAWT position. The measured planes started with $X/D = -2, -1, 0, 1, 2, 3, 4, 5, 6, 7, 8, 9, 10$. The measured phase-lock measurement was done with a different mode of data acquisition and with a trigger mechanism for every rotation, this is explained in detail in the above subsection 3.6.3 Phase-locked Acquisition for Wake synchronisation.

post process specifications	
Property	Dimensions
Post process server	PIV server 1
post process function	stereo cross-correlation function
Weight of parameters in cross correlation	1:1
Maximum expected displacement	12 pixel (13.4 m/s)
Spatial resolution	32 pixel (8.22 mm)
Multi-pass vector window size	32×32
Overlap ratio	75%

Table 3.3: Post-processing specifications

3.7. Post-processing of the Time Averaged Wake Flow

Stereoscopic PIV experiments are conducted, mapping the three-component velocity fields in the rotor wake up to 10 rotor diameter downwind; results are obtained via a time average of the vector fields, as detailed in table 3.3. The post-processing of the wake flow is done using the PIV server 1 at a high-speed lab. Aerospace Department, TU Delft. A version of Davis 10.0.5 is used, the post-processing is done using multiple steps and band-pass filters to start with, a average time series step is incorporated to subtract average time filter with a filter length of 11 images, followed by a stereo cross-correlation function is enabled between the two camera images with a maximum expected displacement of 12 pixels (13.4 m/s) and a spatial resolution of 32 pixel (8.22 mm). A multi-pass vector calculation is adopted with a window size of 32×32 , a weight of 1:1, and a overlap ratio of 75% with three passes. A final step of vector statistic for vector field results to obtain the spatial average velocity and its standard deviation, where standard deviation has a range of 2.5 times the average value.

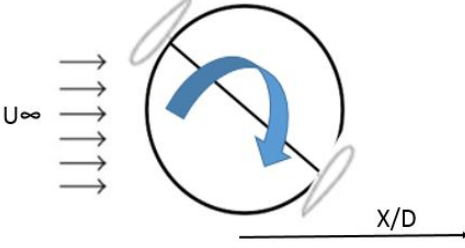
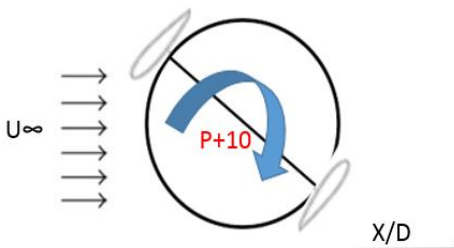
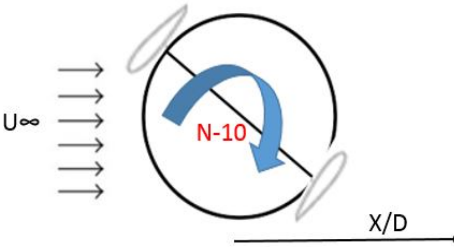
Case description		
Case no	Case	Description
1	<p>VAWT-1</p> 	<p>Baseline case: Single rotor with straight blades (Zero angle deflection on blades) Wake measurement till 10 x/D</p>
2	<p>VAWT-1</p> 	<p>Positive pitch angle case (+P10): Single rotor with blades deflected to a positive 10 degree angle (angle of attack is been increased on the blades) Wake measurement till 10 x/D</p>
3	<p>VAWT-1</p> 	<p>Negative pitch angle case (-N10): Single rotor with blades deflected to a negative 10 degree angle (angle of attack is been decreased on the blades) Wake measurement till 10 x/D</p>

Table 3.4: Wake velocity measurement case description

4

Results, comparison, and discussion

In this chapter, a fair comparison between the CFD simulations and theoretical wake models has been observed, also parameters relating to wake growth rate, and center-line wake profiles have been discussed 4.1. The data acquired by stereo-PIV is analyzed and reported where mean quantities are computed as time averages of the wake flow. A fair comparison and study of all the wake models have been done in the following chapter. Firstly the experimental data has been rearranged in order to understand the correct co-relation to the theoretical and CFD models 4.1. Secondly, the experimental data is meticulously compared to the CFD model, theoretical Gaussian model, Jensen wake model studied in section 2. Lastly, a discussion is made on all the models ,and comments are constructed on a comparison between the wake deficit at different downwind positions. The following has been repeated for a set of cases performed during the experimental campaign in section 4.2.

4.1. Realisation of Theoretical Wake Models and CFD Simulations with Experimental Results

In this section, the more reliable and accurate analytical model by Mahdi Abkar [1] based on the theoretical framework for HAWT by Bastankhah and Porté-Age [6] will be realized for our case. The constraints such as wake growth rate and ϵ (initial wake growth just after the rotor) will be calculated and compared based on wake propagation for CFD and experimental results.

In order to validate our analytical model based on works of Mahdi Abkar [1], a CFD data is considered and acquired from previous experiments by Huang et al [17], and the C_T is from the measured force balance system (Baseline case). This CFD data provides with turbine induced three-dimensional velocity flow field distribution of the wake for up to 10 diameters in the stream-wise direction downwind of the rotor and for 2 diameters in upwind of the rotor. A MatLab script is built in order to process and shape the CFD data, and achieve the required wake velocity distribution. In the table 3.1 in chapter 3, design specifications for the constructed VAWT are listed:

The spatial distribution of wake velocity field over the VAWT specified above is shown in the figure 4.1 It represents a contour plot where the X and Y-axis denote the stream-wise distance downwind of the rotor (X/D) and span-wise width (Y/D) for the expansion of wake in Y direction respectively. Note in figure 4.1 (a) the wake velocity in the contour, as the VAWT is been placed at ($X = 0$) a pool of decreased wake velocity can be observed after the rotor shown in dark blue, with the increase in the stream-wise distance behind the rotor the wake recovery can be observed, as the blue shifts to chrome yellow showing recovery in the wake, with wind velocity similar to the one before the wake formation (wind velocity upstream of the rotor). Figure 4.1 (a) shows the wake velocity deficit normalized using free-stream velocity (U_∞) here the recovery in the CFD model is easily observed with the shift in the color bar from a minimum deficit (dark blue) to wake recovery of (chrome yellow) where the

deficit approaches almost 1, i.e., the free-stream velocity. The figure 4.1 (b) displays a wake velocity deficit normalise by (ΔU_{max}) where (ΔU) is the wake velocity subtracted from the free-stream velocity $(U_\infty - U_{Wake})$. Note the change in contour plot here, the spatial distribution clearly shows the incoming wind passing over the turbine, whereas the turbine produces a narrow wake channel, with a higher recovery at the edges of the wake structure due to more turbulence.

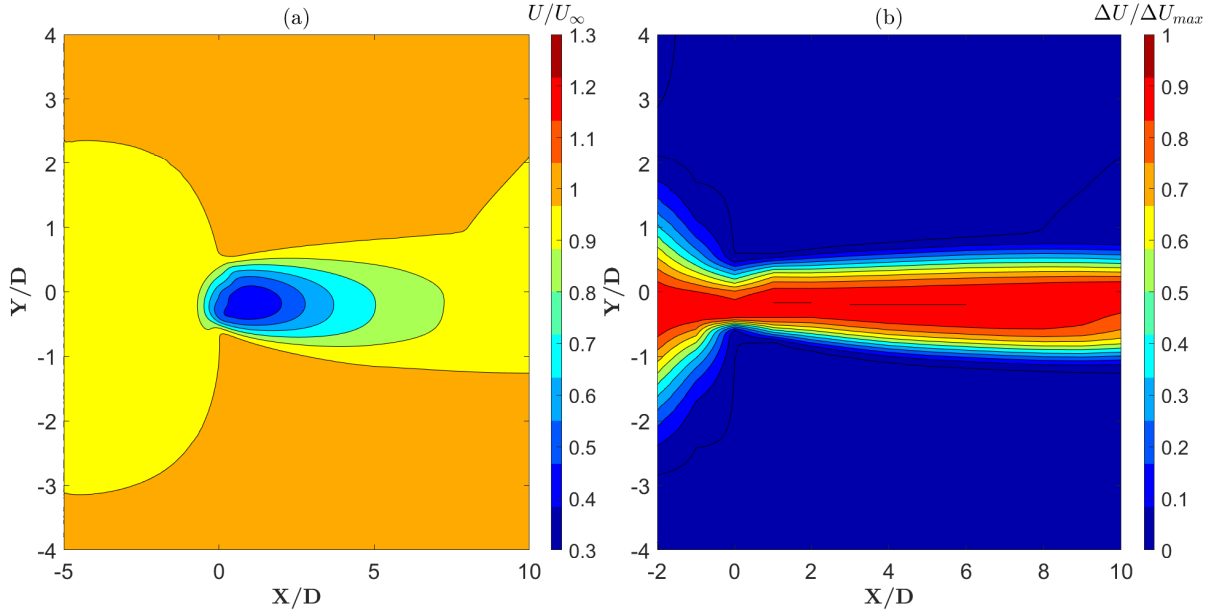


Figure 4.1: Wake velocity deficit parameters for CFD model, (a) wake velocity normalized by free stream velocity, (b) wake velocity deficit normalized by wake velocity deficit max for 10 rotors downwind distance

In relation to the above contour, the figure 4.2 shows the wake velocity deficit (stream-wise velocity profile at the center-line) at different rotor diameters downwind of the turbine (near wake ($X/D=1,2,3$), far wake ($X/D=5,7,10$) with the transverse coordinate Y-axis normalized by half of the wake width. From the previously studied theoretical wake models in the section 2.2.8 in this study, a self-similar Gaussian profile of the velocity deficit is found in the far wake. In order to examine whether the wake of VAWT follows the Gaussian distribution, the wake data is rearranged. where a function of maximum wake velocity deficit $(\frac{\Delta U}{\Delta U_{max}})$ is arranged against half value of span-wise distance (Y) or wake half-width. These wake half-width $r_{1/2}(X)$ is defined at each X position as:

$$\frac{\Delta U(r = r_{1/2})}{U_\infty} = \frac{1}{2} \frac{\Delta U_{max}}{U_\infty} = \frac{1}{2} C(X), \quad (4.1)$$

The equation 4.1 is used as the characteristic wake width in the figure 4.2. The figure shows the profile of $(f = \frac{\Delta U}{\Delta U_{max}})$ plotted against $(r/r_{1/2})$ approximately collapse into a single Gaussian curve, except at the edges of the wake. This means that the velocity deficit profile can be assumed to have a self-similar Gaussian shape after some downwind distance. Hence a Gaussian function is fitted to all the maximum wind velocity deficit in near and far wake regions ($1,2,3,5,7,8,10 = X/D$) respectively.

For simplicity, the Gaussian fit is assumed for the further development of the model. The wake growth rate (k^*), and the wake growth immediately after the rotor: at X approaches to 0 (ϵ), mean, standard deviations, and other parameters of the wake velocity deficit are devised from the Gaussian curve. The above fits at each downwind distance from the rotor (1D-10D). The standard deviation of the wake width in the span-wise direction is plotted against the rotor behind distances in the figure 4.3. Also, a linear fit has been equipped to calculate the wake growth rate. The evaluated CFD data here has a very low relation with the turbulence intensity as the wake velocity deficit has been time-averaged and normalized to observe the wake distribution. Hence the standard deviation of the wake deficit has been observed and taken into accounts for the calculation of the wake growth rate. The slope of the

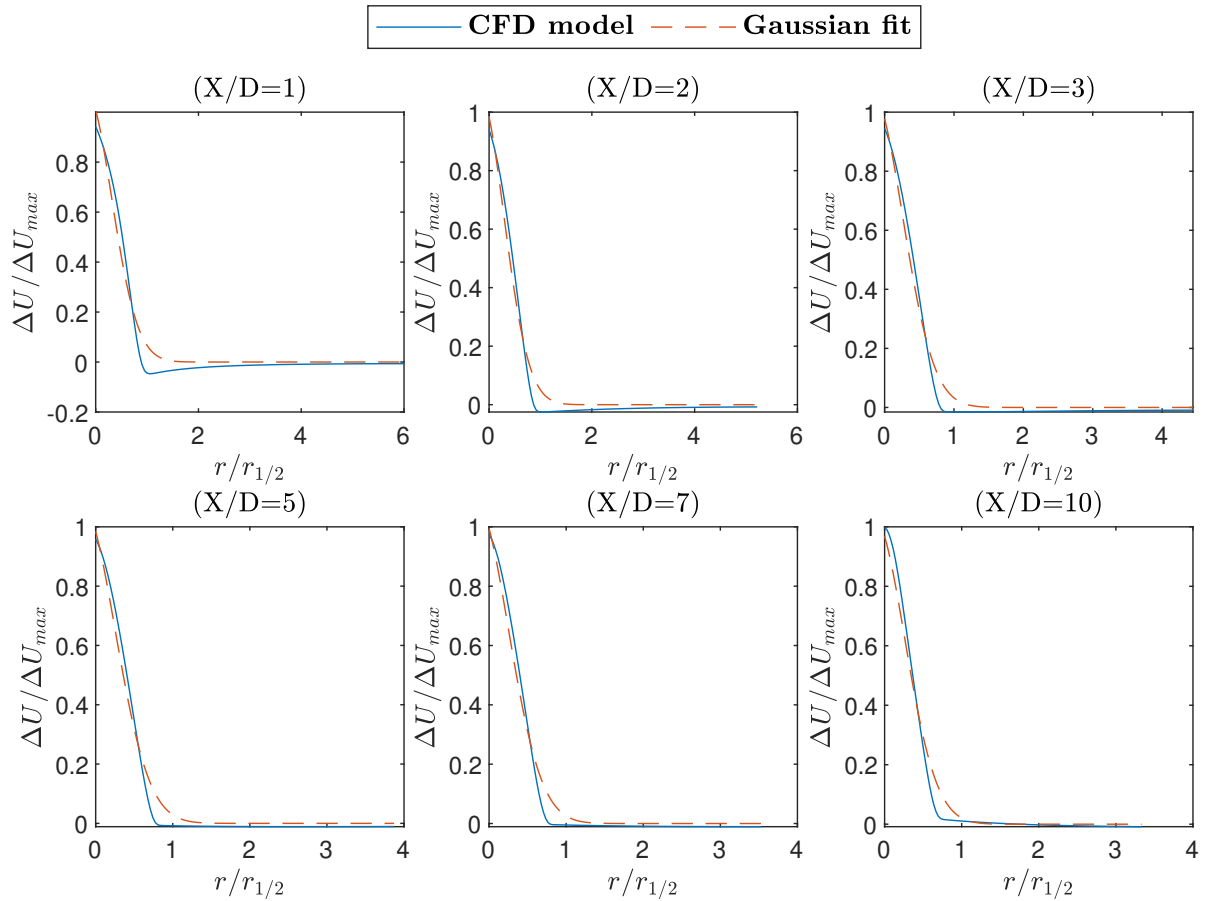


Figure 4.2: Wake velocity deficit normalize by ΔU_{max} fitted with a Gaussian distribution for half the crossflow width (Y/D) at different downwind distances ($X/D=1,2,3,5,7,10$)

linear fit, will represent the value for wake growth rate in this case,

$$\frac{\sigma}{D} = k^* \frac{X}{D} + \epsilon, \quad (4.2)$$

Using the above equation with the CFD data the wake growth rate is calculated to be 0.0258. The value of ϵ wake expansion immediately after the rotor is calculated using [6]

$$\epsilon = 0.2\sqrt{\beta} \quad (4.3)$$

where β is calculated using the equation 2.29 from moment and mass conservation. The value of ϵ is estimated by extrapolating the LES data and the theoretical model values in figure 4.3 see in the literature review (Chapter 2).

With the reckoned k^* wake growth rate and ϵ and a C_T of 0.6828 a plot 4.5 of the maximum wake wind velocity deficit is arranged at every X/D distance behind the rotor (0D-10D). Whereas in figure 2.4 the developed theoretical model from the CFD data is compared against the actual model by Mahdi Abkar [1] and the same HAWT by Bastankhah and Porté-Agel. The comparison shows a similar trend for both the groups a sudden increase in the maximum wake velocity deficit in the near wake region and with the increase in rotor behind distance a gradual decrease in the wake velocity, this depicts the recovery in the far wake region. But, using the theoretical model by Mahdi Abkar [1] with the VAWT specifications used for experiments in this thesis: The values for the maximum wind velocity deficit overshoots the theoretical values of the model developed with the CFD data (CFD simulations).

Also, the figure 2.4 in Chapter 2 study of analytical wake models, shows a comparison between maximum wind wake deficit and rotor downwind distance for wind-tunnel measurements, LES data,

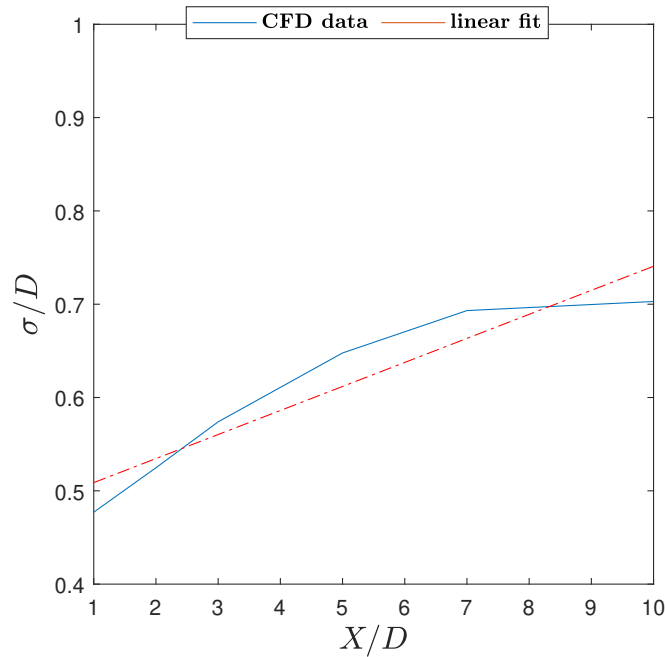


Figure 4.3: Standard deviation in wake width (crossflow (Y/D)) VS Rotor downwind distance, with a linear fit

Bastankhah and Porté-Agel Model, Jensen model and Frandsen model [6]. Case 1 shown at the top in the figure corresponds to the wind-tunnel measurements reported by Chamorro and Porté-Agel [9]. Correlating this case 1 values with the values from the figure 4.5 here a similar comparison is presented, the experimental data, CFD model, and the theoretical Gaussian developed model similarity can be observed and cohesion between both the cases can be established. Here it can be observed that with the increase in rotor downwind distance the maximum wake velocity deficit is recovered for all the models, whereas the CFD model shows the fastest recovery compared to Gaussian and experimental models. Whereas the Gaussian model depicts its recovery units in between the experimental data and CFD model. This resemblance, both from the previous experimental study (literature) and the present study can be accounted to institute the validity for the developed theoretical Gaussian model and its parameters.

Lastly, a correlation is presented in the contour plot 4.4 where (a) displays a wind velocity deficit ($\frac{\Delta U}{U_\infty}$) for the model by Mahdi Abkar [1] based on work of Bastankhah and Porté-Agel Model [6], and the (b) displays the same for CFD model developed using the CFD data, both show the position of the rotor to be at 0 (X/D). The wake deficit contours can be easily spotted, showing yellow: the near wake velocity contour and moving towards dark blue as the wake recovery propagates to the far wake region. A slight difference in the wake geometry can be observed here, the CFD model with the CFD data showing a different rate of wake expansion (smaller) immediately after the rotor (for near wake 3D) and a slightly larger wake expansion rate for the rest of the rotor downwind distance. Whereas the model by Mahdi Abkar [1] based on the work of Bastankhah and Porté-Agel Model [6] shows a uniform wake growth rate, with a drop in the wake velocity deficit a bit later rotor downstream than the other model.

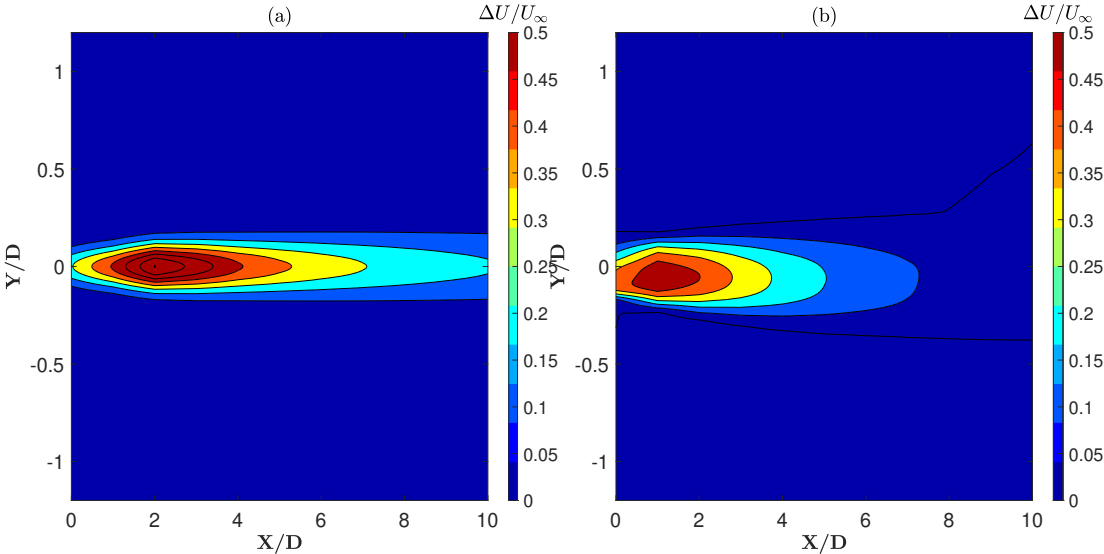


Figure 4.4: Comparison between theoretical model by (a) Mahdi Abkar Model, and (b) CFD model

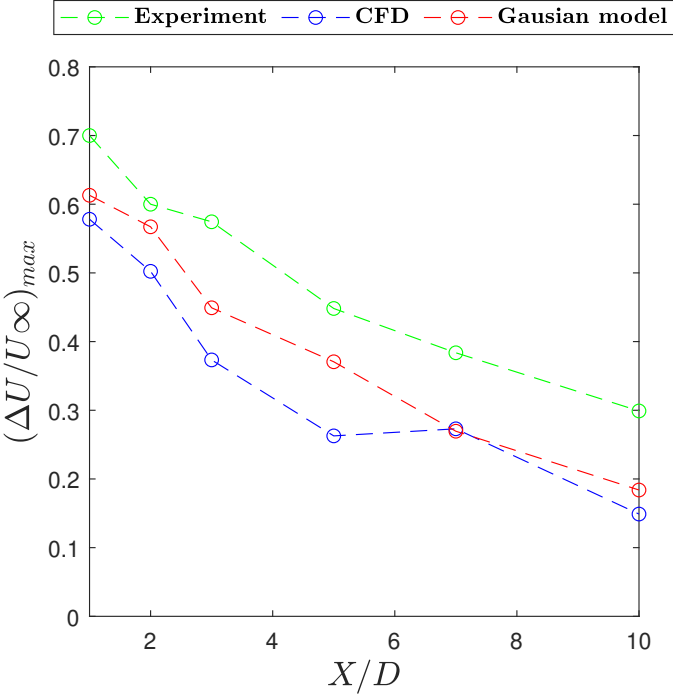


Figure 4.5: Maximum wake velocity deficit (experiment case (zero pitch), CFD Model, Gaussian model) vs Streamwise distance (downwind)

Realisation of Wake Models with Experimental Results

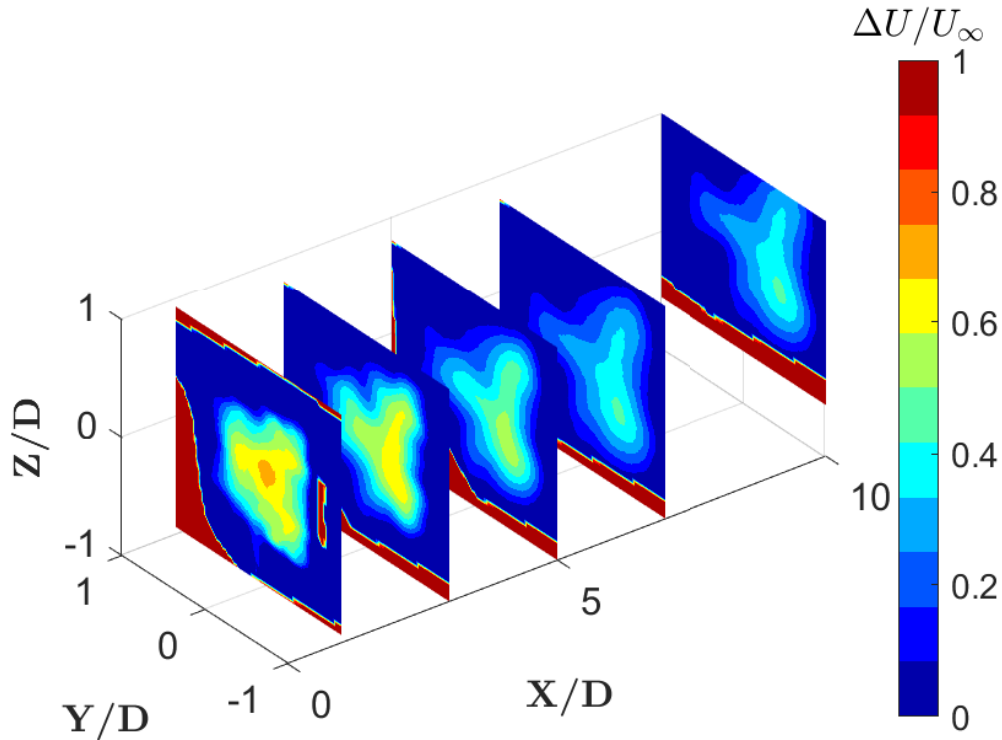


Figure 4.6: Contour plot of wake velocity deficit normalised by free stream velocity ($\delta U/U_\infty$) for $X/D= 2,3,5,7,10$ rotor downwind distance for baseline case

The shape and structure of the wake are presented in the figure 4.6 which shows the mean velocity deficit over 10 measured planes (only 5 planes are shown in the figure). It represents a 3d plot of wake velocity deficit given by $\Delta U/U_\infty$ at 1,3,5,7,10 rotor stream-wise direction. Where Y-axis denotes the transverse direction expansion of wake (Y/D) (normalized by the the rotor diameter) and the z-axis represents the span-wise rotor height direction (Z/D). Here the observation made is that with the increased span-wise distance with the rotor the wake expands gradually and recovers, This is denoted by the color bar with decreasing wind velocity deficit in the wake (shown by the redshift). As the chrome yellow shifts to blue showing recovery in the wake, gradually as the distance is increased. Note the increase in the standard deviation of the wake crosswind width. There is a shift in the last plane at $X/D=10$ in the span-wise direction (Z), this is done in order to capture the full wake in two parts. The shown elevated plane captures the top half part of the wake here an assumption is made for the bottom half-plane that, it is similar to the top half part.

From the previously studied theoretical wake models in section 2 and the corresponds to the wind-tunnel measurements reported by Chamorro and Porté-Agel [37] and the LES performed by Wu and Porté-Agel [34] to investigate the wake of a miniature wind turbine in a turbulent boundary layer flow. These studies show a self-similar Gaussian profile of the maximum velocity deficit for wind tunnel measurements and the LES data at different stream-wise distances (far wake). In order to clearly visualize the spatial wake velocity field and its Gaussian attributes in the experimental post-processed data, a rearrangement of the wake data is necessary. Hence the above data in the figure 4.6 has been sorted and rearranged. Here to acquire the maximum velocity deficit along with the cross-flow and span-wise direction and to check its quality. A fair comparison of center-line velocity and maximum velocity deficit was made and to be assured they both coincided well. (Note: As it is assumed further, for all model calculations that the center-line velocity would present the maximum moment deficit in the whole wake

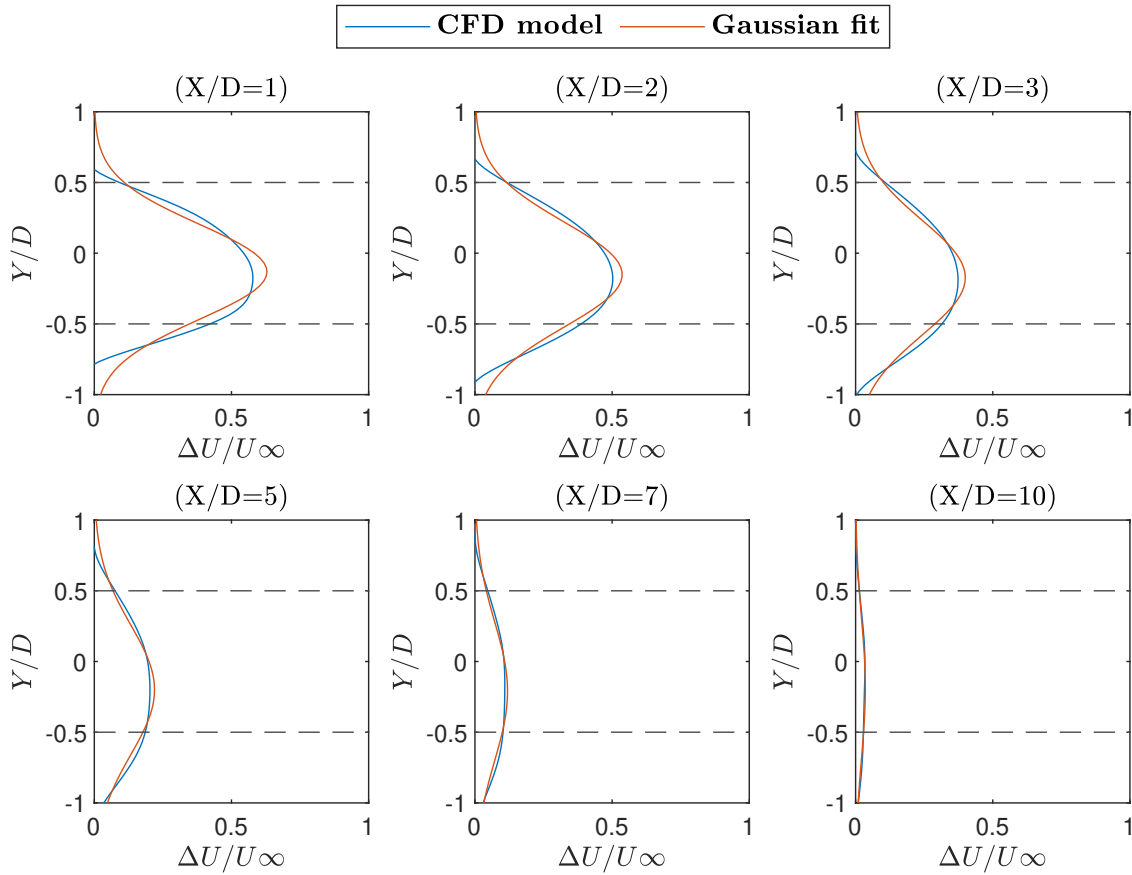


Figure 4.7: Crosswind profile of centerline streamwise wake velocity deficit normalized by (U_∞) (solid blue line) CFD data, and (solid red line) Gaussian fit on them for 1,2,3,5,7,10 rotor downwind distance

cross-section). This was checked with this comparison study.

The figure above 4.7 shows a multivariable Gaussian curve fitted over the center-line wake velocity deficits at near and far wake regions ($X/D = 1, 2, 3, 5, 7, 10$). The X-axis represents the velocity deficit normalized by the free-stream velocity, and the Y-axis is the cross-flow distance normalized with rotor diameter. The Gaussian fits are used in determining the wake growth rates (k^*) and the cross-flow spread width and used as a comparison with theoretical work. The dotted line here represents the rotor diameter. A similar approach is used in the figure 4.8 where instead of the CFD data, experimental center-line velocity deficit data (also maximum velocity deficit in the cross-flow vs span-wise plane) from cross-sections at different rotor span-wise distance (1,2,3 X/D) near wake and (5,7,10 X/D) far wake was used and a multivariable Gaussian curve was fitted to the same. The blue solid line shows the experimental velocity deficit normalized by free stream velocity and the red solid line shows the Gaussian fit. Note the CFD data approximately collapse onto a single Gaussian curve except at the edge of the wake. It means that the velocity deficit profile can be assumed to have a self-similar Gaussian shape after some downwind distance. Whereas the experimental data doesn't show a good agreement, for the experimental data two peaks are observed and the Gaussian fit over the data is skewed as compared to the CFD counterpart.

In the figure,4.9 The normalized standard deviation of the Gaussian curves fitted to the velocity deficit profiles in the wake is plotted as a function of normalized stream-wise direction for CFD and experimental cases. It shows that the wake expands approximately linearly in the range of $2 \leq X/D \leq 10$ for both cases. The wake expansion rate of both CFD and experiments were compared and found to be almost coincide, $k_{CFD}^* = 0.02510$, $k_{EXP}^* = 0.02518$. Hence for the comparison study (Gaussian, CFD, Jensen) in the present work the following wake growth rate is been assumed. The calculated wake

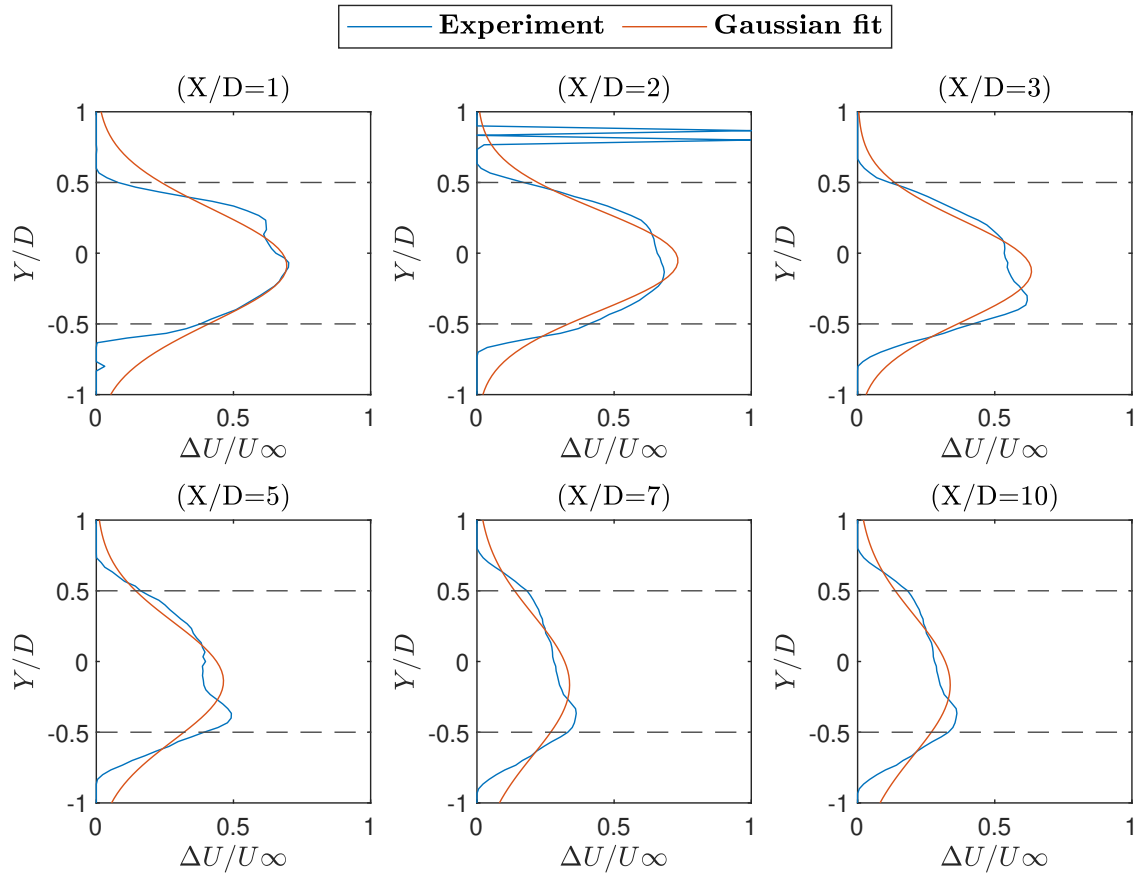


Figure 4.8: Crosswind profile of centerline streamwise wake velocity normalized by (U_∞) (solid blue line) Experiment, (solid red line) Gaussian fit for 1,2,3,5,7,10 rotor downwind distance

growth rate is in good agreement with the LES, experimental data, and theoretical wake proposed by Mahdi Abkar [1] based on the work of Bastankhah and Porté-Agel Model [6]. Although classical theories of shear flows predict the wake width varies as $x^{1/3}$ [49]. This discrepancy might be due to the following reasons: To derive this power-law dependence of wake width on X in classical studies, $\Delta U/U_\infty$ at the wake center is assumed to tend to zero (lower than 0.1). [49] whereas it is not a good assumption in the area of interest of turbine wake in our experiments $X/D \leq 10$. Secondly, in classical studies [34], the effect of ambient turbulence intensity on the wake growth is not considered. In turbulent boundary layers, the wake is, however, known to recover faster than in non-turbulent flows. In our case, shear-generated turbulence is almost negligible. (As a blue table is attached to the opening jet of the wind tunnel).

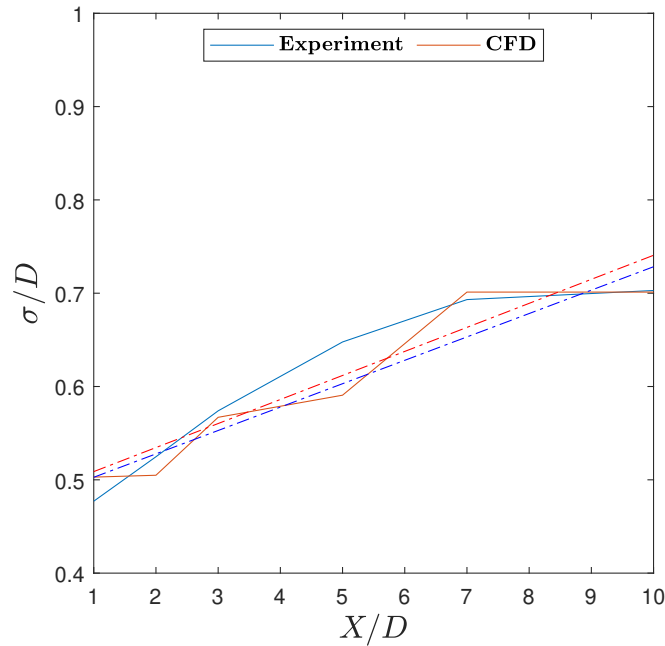


Figure 4.9: The experiment standard deviation (solid blue line), CFD (solid orange line) of wake velocity deficit, linear fit(dotted red lines) vs Rotor downstream distance 1 X/D to 10 X/D

4.2. Experimental Validation of Wake Models and CFD simulations

The wake recovery for different pitch angles and arrangements of VAWT was quantified by threshold planar slices of the stream-wise velocity component at various stream-wise positions downstream of the turbine by the free upstream flow velocity incident on the turbine, U_∞ . For each slice, this threshold procedure divided the wake region, defined as the region of flow where the local stream-wise velocity component was less than U_∞ , from the surrounding free-stream region. This wake velocity normalized by the free-stream velocity U/U_∞ at various stream-wise positions (near wake and far wake) was plotted against cross-flow and span-wise width X and Y-axis respectively. Where the X and Y axis were normalized by rotor diameter (D). Figure 4.10, 4.11. From left (a) experiment result, (b) CFD result, (c) Gaussian model by Mahdi Abkar based on theoretical wake development work of M. Bastankhah, F. Porté-Agel, and lastly (d) the Jensen wake model for near wake ($X/D = 1,2,3$), far wake ($X/D=5,7,8$) respectively. At a tip-speed ratios of $\lambda = 2.513$. $C_T = 0.6828$ for baseline case, measured using the force balance system. While the white box is the projection of the small VAWT with a length of 300 mm and a width of 300 mm. The zero on both the X and Y-axis represents the absolute center of the VAWT. As this study seeks to ascertain the effects of wake recovery of the 3-D structure of the near wake and far wake for different VAWT wake models, a set of key differences between the velocity fields of the four turbine models are highlighted. Firstly, in YZ cross-sections of U/U_∞ for the baseline case (Single VAWT with zero pitch angles, no deflection of the blades) downstream of the turbine, topological differences were evident in the wake region of the four compared models, where the local streamwise velocity fell below the free-stream velocity.

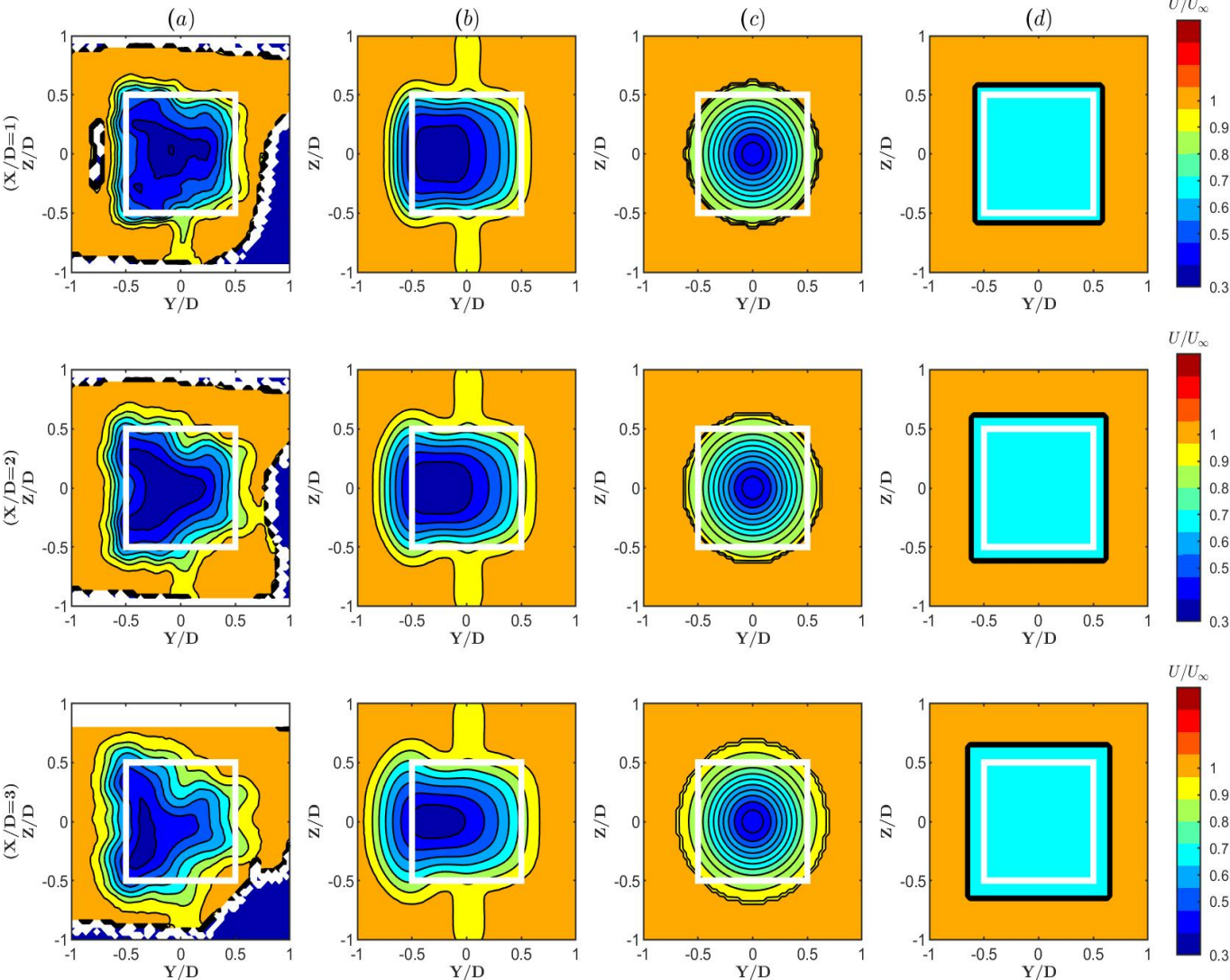


Figure 4.10: Contours of streamwise wake velocity at different downstream positions near wake ($X/D= 1,2,3$) normalized by the free stream velocity (U_∞) for baseline case

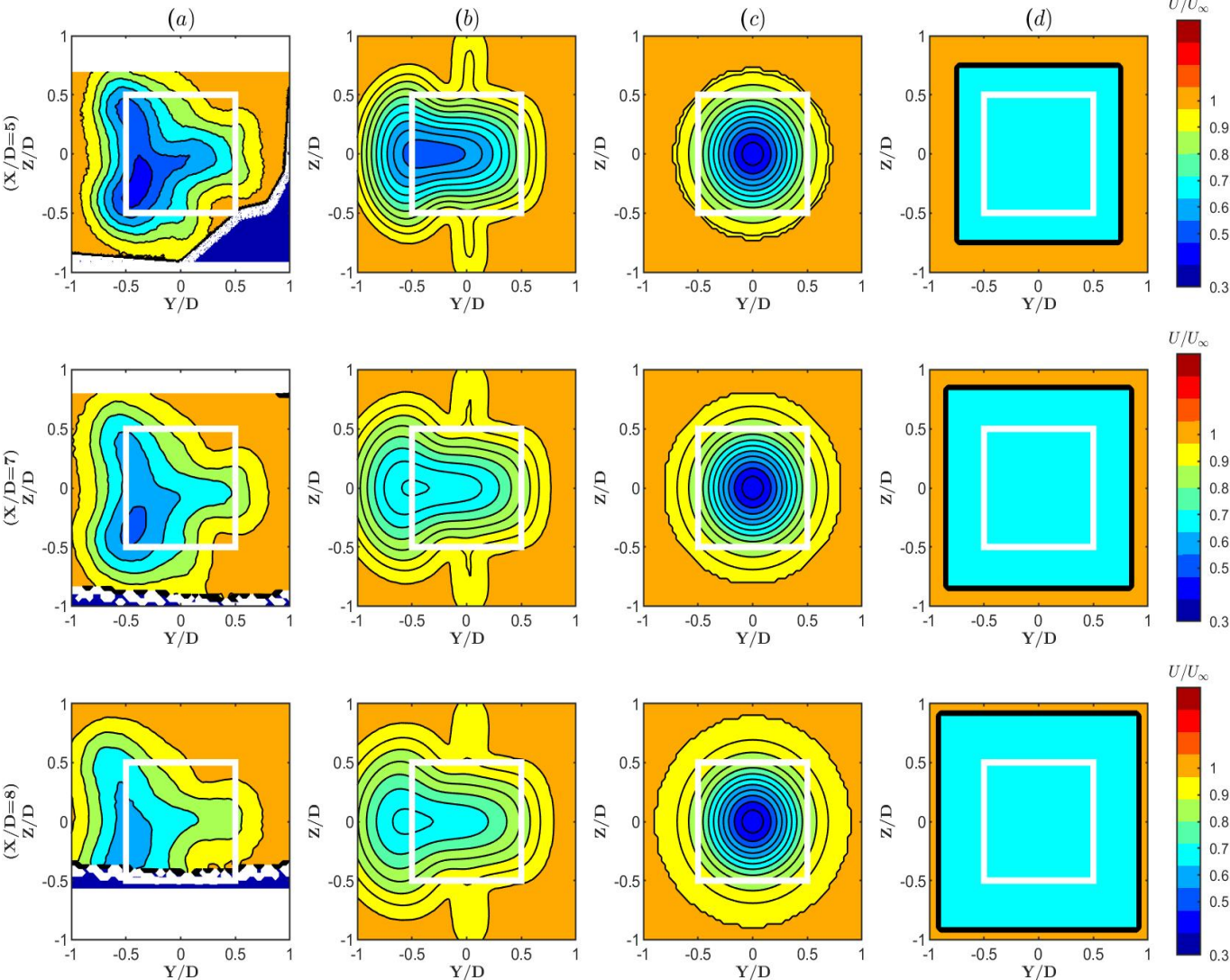


Figure 4.11: Contours of streamwise wake velocity at a different downstream position far wake ($X/D= 5,7,8$) normalized by the free stream velocity (U_∞) for baseline case

Comparing the normalized velocity (U/U_∞) in the cross-flow region (Y/D) to the position of the rotor indicates that the far wake region ($5X/D$ to $8X/D$) is deflected towards the negative- Y direction, for the experimental data and CFD model. Velocity deficit in the wake is unevenly distributed such that the momentum behind the negative- Y sector of the rotor (direction of rotor blades turning into the wind) is significantly lower than behind the positive- Y sector this can be observed through the color bar shift from blurple to chrome yellow. The wake shift in the negative- Y direction can be caused by the blade rotation, with the clockwise rotation of the vertical axis rotor, and the rear blade turning into the incoming flow of wind. Whereas, for the near wake region ($1X/D$ to $3X/D$) there isn't an observable shift in the negative- Y direction as the wake is clearly starting to mix and not totally expanded. Secondly, The vertical profile of normalized velocity (U/U_∞) span-wise width (Z/D) shows an uneven distribution on both sides above mid-span and below mid-span (with the center of the rotor being at $Z/D=0$) but the wake recovery profile is almost symmetric on both sides except on the negative Y -direction: A downward swept pool caused by the turbine tower, hence the higher region of the wake returns to the inlet condition more quickly than the lower portion. For the CFD model, the wake expansion in both far and near wake in span-wise direction is symmetric on both the ends. Finally for the baseline case, the Gaussian model and Jensen model both expand with an expansion rate of $k^* = 0.0251$ shown in figure 4.9 comparison of CFD and experimental expansion rates. These models are to be symmetric in both cross-flow and span-wise direction, with the Gaussian model forming gaussian profile of wake recovery and the Jensen model with the top hat approach expanding according to the rotor dimensions. Comparing the four models side by side it can be seen that the wake topography of experimental results is very different than that of the theoretical models, also the CFD models do not produce an accurate representation of wake deficit.

The reasons to account for the change in wake topography for experimental results of VAWT when compared to CFD and theoretical models are due to the factor of, presence of two pairs of counter-rotating vortices at the edges of the wake. The pairs are of different magnitudes, with those in the wake of the negative- Y section of the rotor which turns into the wind being significantly larger and stronger than those in the wake of the positive- Y section. As stated in the previous studies by Rolin, F. Porte-Agel [37], the wake of the VAWT features two pairs of counter-rotating vortices. Figure 4.15 shown contours of baseline case stream-wise velocity deficit at different downstream positions ($X/D=1,2,3,5,7,10$) normalized by the free stream velocity in-plane velocity vectors are overlaid. The outline of the rotor is delineated by a black box. This in-plane velocity vector depicts the formation of the vortices pair at the diagonal corners, top left, and bottom right as can be seen clearly in the $X/D=3$ counterplot. Hence it is critically important to understand the cause of these vortices and under what condition they appear and their effect on wake re-energizing and redistributing of momentum.

The VAWTs act as an actuator cylinder model rather than the actuator disk concept and are expected to exert lateral forces, During the rotation, the blades of VAWTs exert both a stream-wise and a lateral force on the wind by conservation of momentum. Due to continuity, this crosswind force introduces crosswind momentum to the flow, and as a result, gives rise to the occurrence we have associated with the production of a CVP (counter-rotating vortices) [37]. A similar phenomenon is observed by Bastankhah and Porte-Agel [7] in the wake of yawed HAWTs in wind-tunnel experiments. In this case, they introduced a yaw angle to the HAWTs resulting in a crosswind force being exerted on the flow by the turbine. which in opposition induces a lateral velocity through conservation of momentum. Due to the continuity, the crosswind gradient of lateral velocity induces a vertical gradient of vertical velocity: these gradients report the crosswind vortices observed in the flow. The yawed HAWTs, wakes to appear to have much in common with the wakes of, VAWTs with the phenomenon of not only the production of CVPs but also the cross-flow deflection of the wake center in a similar direction as the velocity induced by the rotor (in our case negative- Y seen above). Analyzing the fluxes of momentum deficit and the motion of in-plane velocity vectors in the wake figure 4.6, 4.13, 4.15 these vortices appear to induce significant crosswind motion, also indicating that these CVPs will be the most important mechanism in introducing momentum to the wake. Note these counter-rotating vortex pairs tend to occur where there is a variation in crossflow momentum which can be spotted in the figure 4.15.

The principal cause of wake re-energizing, redistributing momentum and change in wake topography of the experiment results are the combined action of the vortice pairs which induces the highly energetic unperturbed flow into the wake. The wake recovers asymmetrically as more momentum is entered from the free stream flow (U_∞) into the wake, by the asymmetric distribution of the load along with the actuator cylinder as stated above. The high-velocity gradient from the boundary of the wake behind the negative-Y section of the VAWT gives rise to peak turbulence levels and encourages mixing in this region. The normalized velocity advective flux of stream-wise momentum, shown in figure 4.10, 4.15 illustrates the impact of the counter-rotating vortex pair on transporting momentum into the wake (seen with a change in wake structure as it recovers downwind distance to the rotor). Studies by [37] suggest that the turbulence tends to play a large role in mixing momentum and re-energizing the wake. It is clearly observed that the highest levels of turbulence mixing of the wake occur at the periphery of the wake, figure 4.10. The stronger velocity deficit gradient on the negative-Y boundary of the wake produces significantly stronger turbulence, whereas the vertical profile of the wake shown in figure 4.14 shows an almost symmetrically moving flow with a very slight change in flow moment at higher in the boundary (positive, span-wise width) causes a smaller change in velocity gradient at the upper boundary of the wake, leading to slightly higher mixing at the upper boundary. The results of wake expansion in the vertical direction are not in consistent with the previously observed behavior of the wake behind a VAWT in boundary layer flow [37]. As for our experiment the boundary layer effect by the ground is almost negligible. The turbulent fluctuations on the edges of the wake also cause momentum to be entered into the wake.

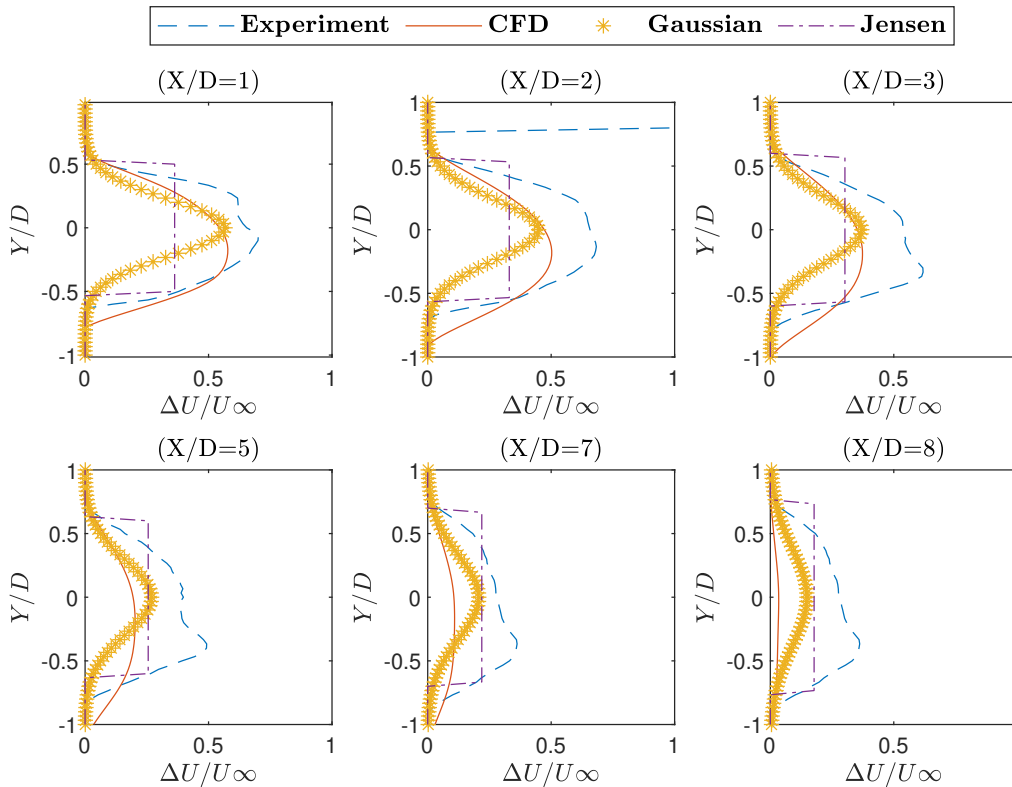


Figure 4.12: A comparison between Experiment data, CFD, Gaussian, Jensen wake model for downwind profile of centerline crossflow wake velocity deficit normalized by (U_∞) at ($X/D=1,2,3,5,7,8$) for baseline case

Tip vortices can also again be a cause of distortion seen in the wake generally for the near wakes as tip vortices are caused by the lift-producing pressure differential over the rotor blades. Hofemann et al [39] followed the trajectory of rotor tip vortices using PIV techniques in the rotor near-wake, and Tescione et al [42] observed their presence and influence on the flow up to a distance of three diameters from the turbine, at which point these vortices tend to roll up and dissipate due to the boundary layer turbulence which causes rotor-tip vortices to break down earlier than in smooth flow.

Figure 4.12 presents a detailed comparison among the experimental data, CFD model, and theoretical wake models. Here maximum stream-wise velocity deficit normalized by the free-stream wind velocity $(1 - \frac{U}{U_\infty})_{max}$ over each stream-wise measurement plane (near wake and far wake) is plotted against the cross-flow width of the wake. The reason behind using a $(1 - \frac{U}{U_\infty})_{max}$ as the wake velocity deficit here is all the models are normalized with the free stream velocity, hence easy for comparison and ease in scaling the models. It can be noted here from previous findings that the maximum stream-wise velocity deficit coincides with the center-line velocity of the wake cross-section. As can be seen, both the theoretical models are capable of predicting the recovery and the expansion of the wake with downwind distance with relatively good accuracy. The experimental data (dotted blue line), CFD model (Solid red line), Gaussian model by Mahdi Abkar (star orange), Jensen wake model (magenta solid line). When compared, both theoretical models and the CFD model under-predicts the maximum stream-wise wake velocity deficit, in both near and far wake cases. Regarding the top-hat model, although this approach is not able to capture the spatial distribution of the wake correctly, it is still beneficial and useful due to its simplicity and its consistency with the widely-used Jensen model for wind turbine wakes. The comparison also reveals that the Gaussian-based wake model is more accurate compared to the top-hat model in predicting the wake velocity defect, also the comparison of the Gaussian and CFD model reveals that the Gaussian-based wake model is more in close agreement to the CFD data, but the only thing it cannot quantify the deflection in the cross-flow direction. This is mainly related to the consistency of the Gaussian wake model with the physics of the turbulent wake development downwind of the turbine. Comparing these models with the experimental data, it is observed that the experimental values form a two peak Gaussian, instead of a single Gaussian, also the wake is asymmetric in the near and far wake as well, which is not in agreement with the self-similar Gaussian wake in far wakes presented by Mahdi Abkar for VAWT and M. Bastankhah, F. Porté-Agel for HAWT in their theoretical wake model. None of the theoretical and CFD models can reproduce or capture the wake phenomenon at the edges of the cross-flow width, also an under prediction of wake velocity deficit by all models is observed.

The deflection in the wake of the experimental case for near and far wakes can be seen in figure 4.13 dotted blue line Experimental wake, solid red line Gaussian-based wake model. Look at the shift in wake to the negative-Y direction which is not quantified by the Gaussian-based wake model, the shift is more prominently observed in the far wake. Also, see the under prediction of wake by Gaussian model with the increase in rotor downwind distance.

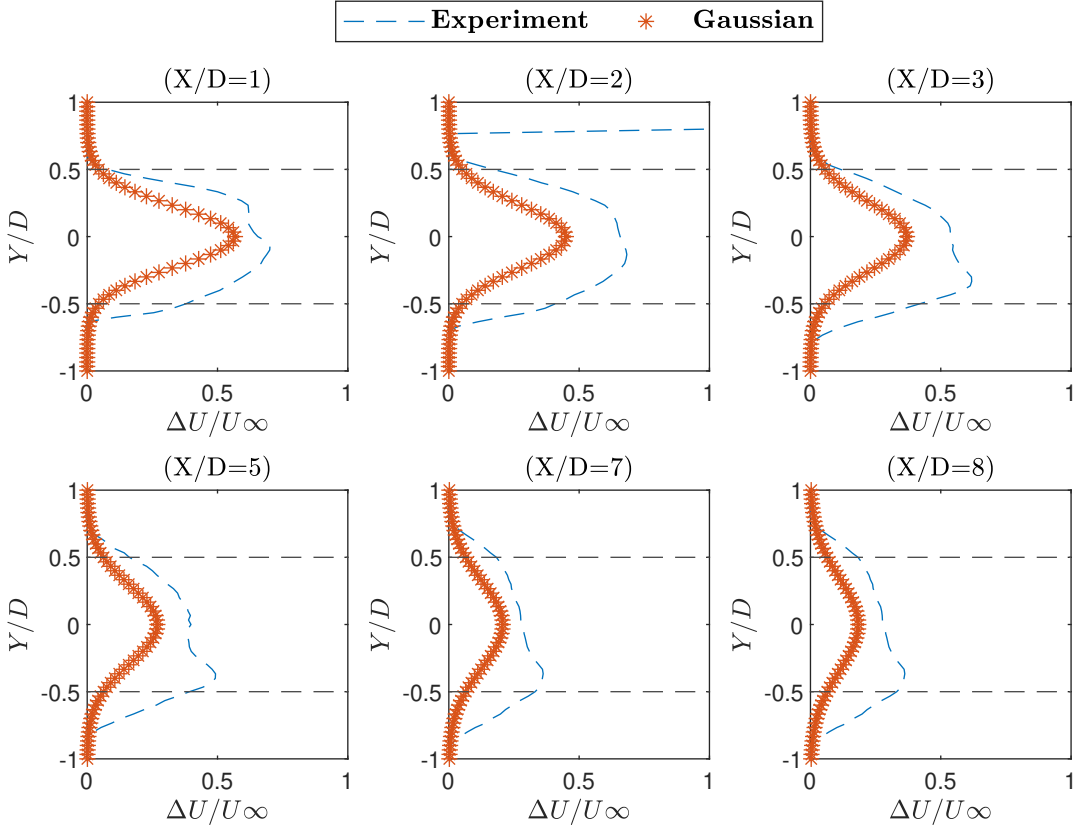


Figure 4.13: Crosswind profile of the centerline streamwise wake velocity deficit normalized by (U_∞) (at midspan). (Dotted line) experimental data (solid line) CFD data at ($X/D=1,2,3,5,7,8$) for baseline case

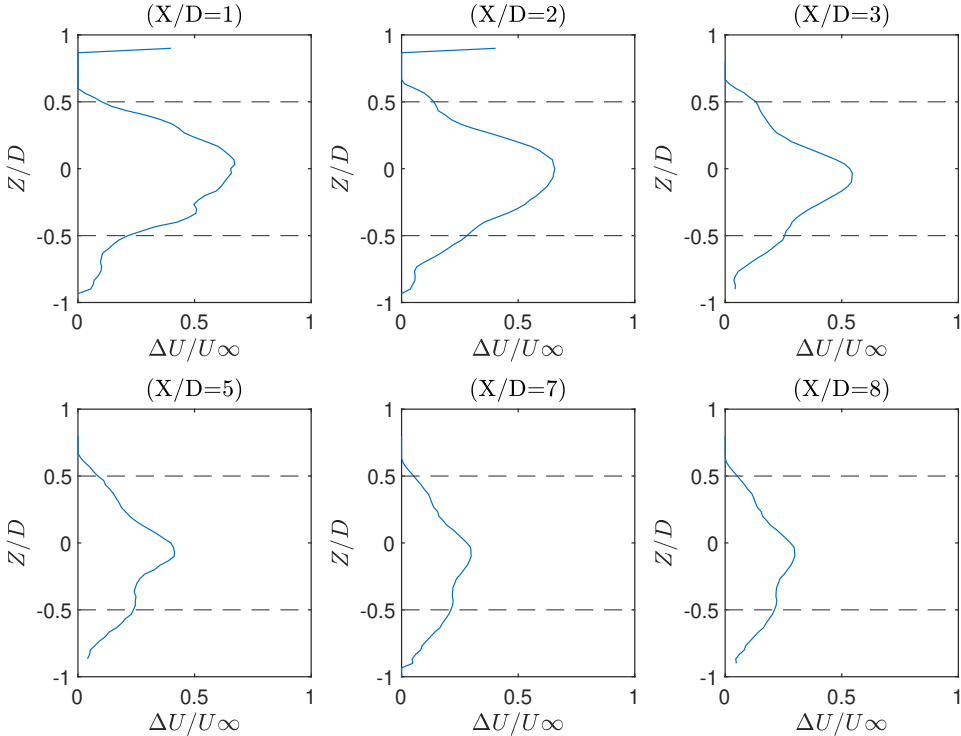


Figure 4.14: Vertical profiles of centerline spanwise wake velocity deficit normalized by the (U_∞) wind-speed (at the midspan) for different rotor downwind distance ($X/D=1,2,3,5,7,8$) for baseline case

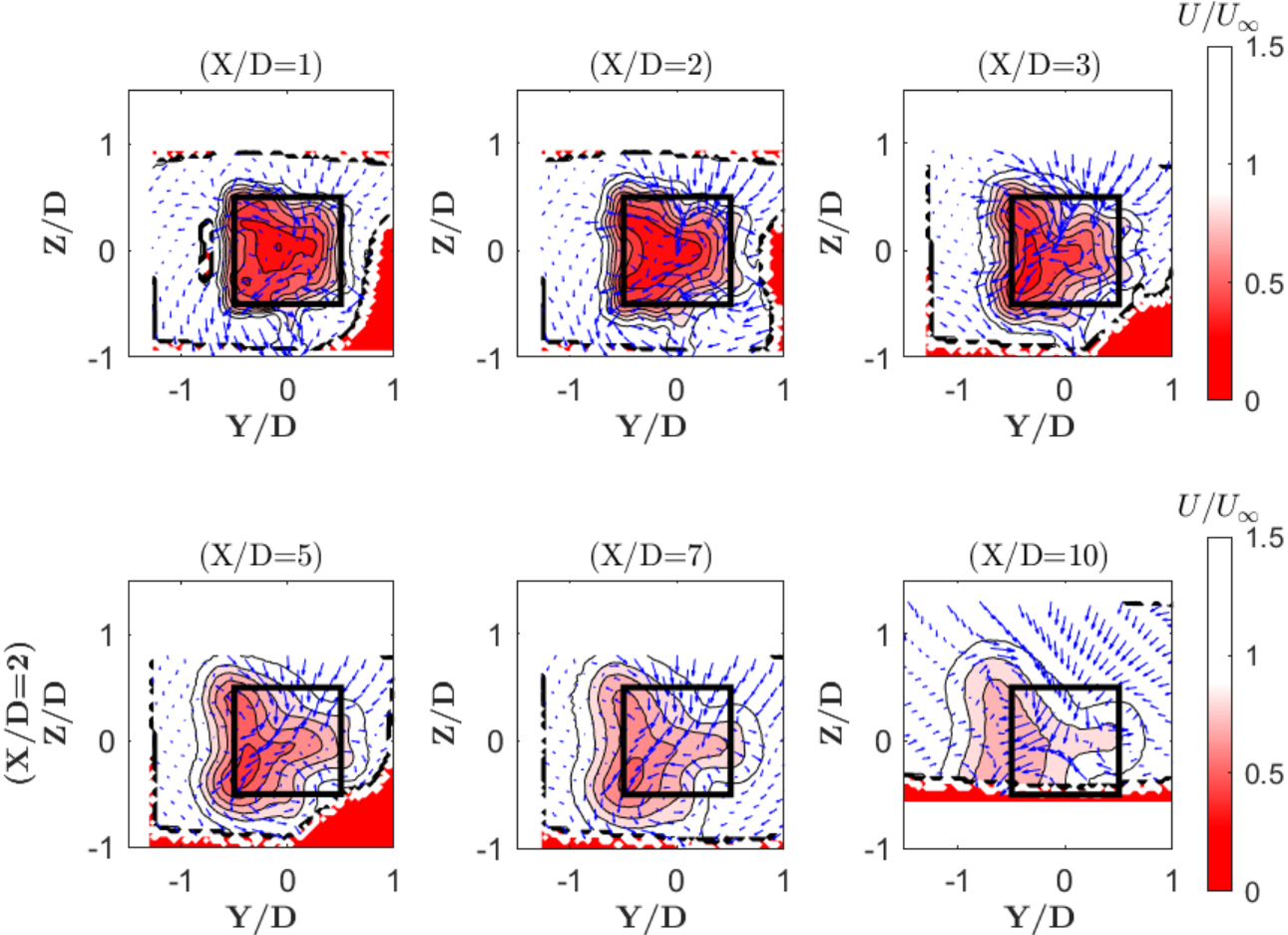


Figure 4.15: Contours of baseline case streamwise velocity deficit at different downstream positions ($X/D=1,2,3,5,7,10$) normalized by the free stream velocity. In-plane velocity vectors are overlaid. The outline of the rotor is delineated by a black box.

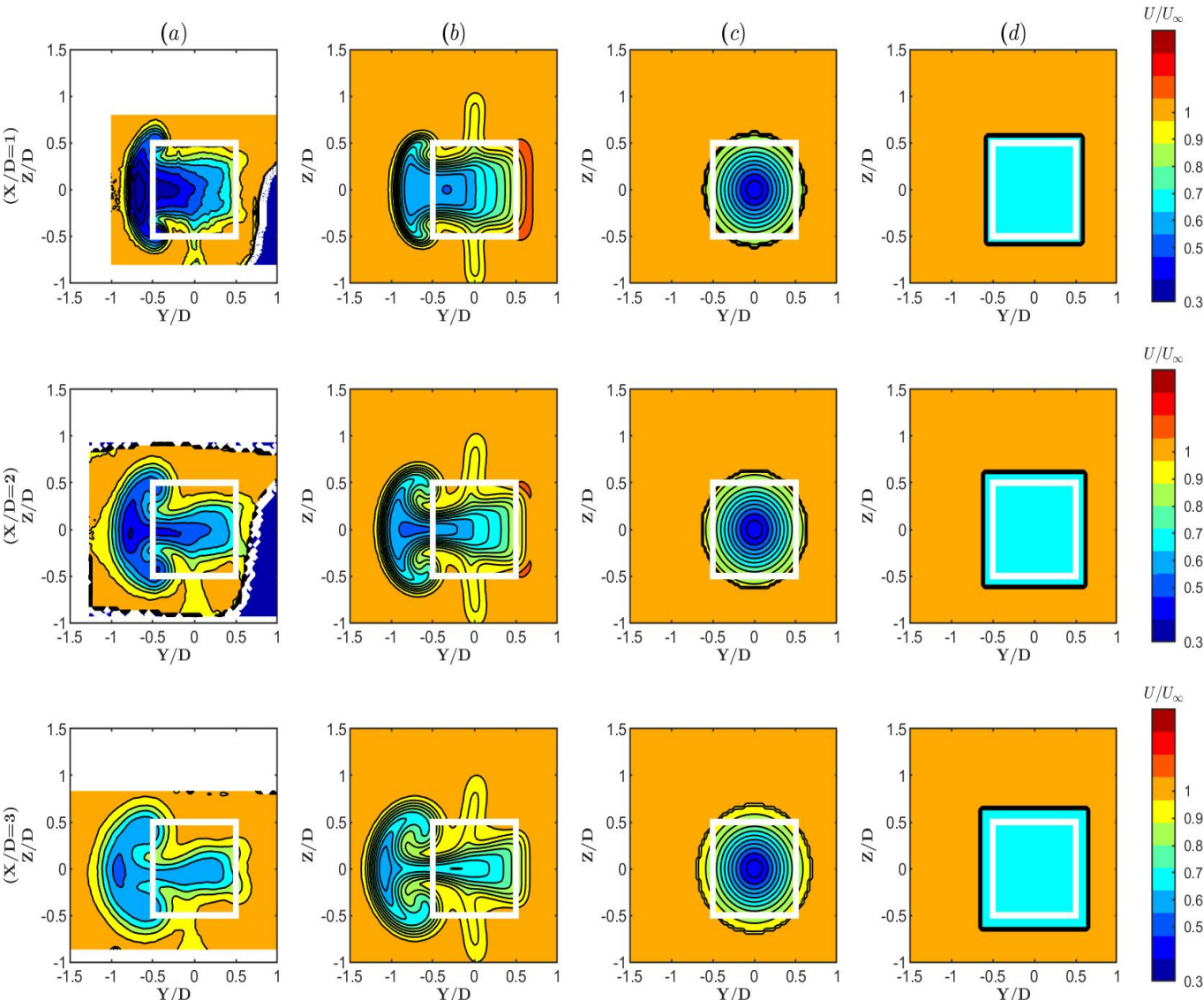


Figure 4.16: Contours of streamwise wake velocity at different downstream positions near wake ($X/D= 1,2,3$) normalized by the free stream velocity (U_∞) for positive 10° pitch angle

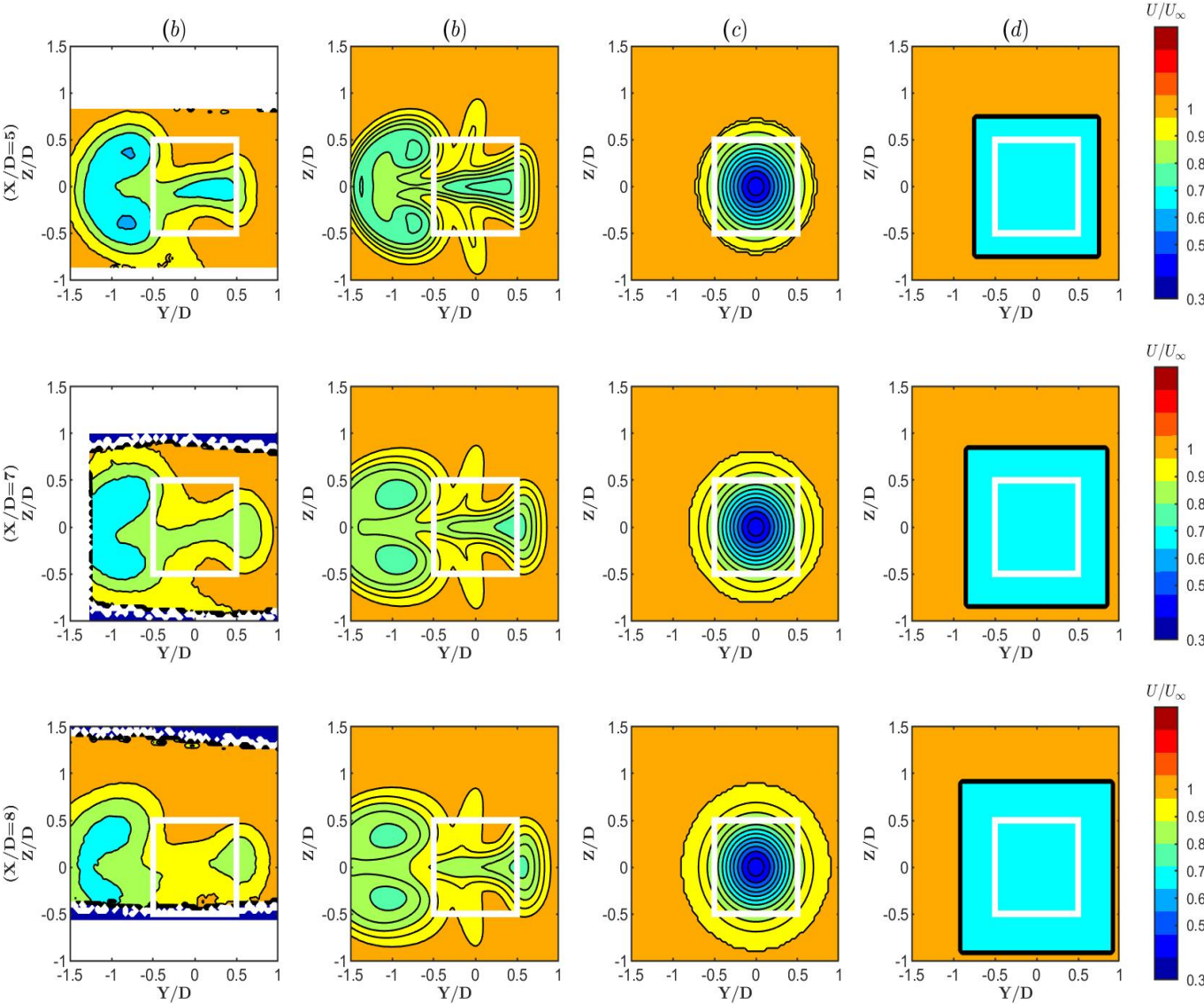


Figure 4.17: Contours of streamwise wake velocity at different downstream position far wake ($X/D= 5,7,8$) normalized by the free stream velocity (U_∞) for positive 10° pitch angle

A similar wake recovery was quantified by threshold planar slices of the stream-wise velocity component in near and far wake at different rotor downwind positions of the turbine by the free upstream flow velocity incident on the turbine, U_∞ . A pitch angle of positive 10 degrees on the blades of the VAWT rotor is shown in the contour plot 4.16,4.17. For each slice, this threshold procedure divided the wake region, defined as the region of flow into wake velocity deficit U/U_∞ and is plotted against cross-flow and span-wise width of the rotor, X and Y-axis respectively. Where the X and Y axis were normalized by rotor diameter similar to the above comparison shown for baseline case. Here the cross-flow width expands from $Y = -1.5 D$ to $1 D$ and the span-wise width from $Z = -1D$ to $1D$ the reason behind the change in the axis is described in the further part of the explanation.

Starting from the left (a) experimental result, (b) CFD result, (c) Gaussian model by Mahdi Abkar based on theoretical wake development work of M.Bastankhah, F. Porté-Agel for HAWT, and lastly the (d) Jensen wake model for near wake ($X/D = 1,2,3$), far wake ($X/D = 5,7,8$) at tip-speed ratios of $\lambda = 2.513$. Here the parameters for the construction of theoretical models are taken from stream-wise, cross-flow, span-wise distances from experiments, k^* wake expansion rate from the Gaussian curve fitting of experimental, and CFD data, C_D Drag force coefficient calculated using the force balance measurements, ($T_D = 1.03154 \text{ N}$, $C_D = 0.7513$, for positive pitch angle on VAWT) and the original dimensions of the rotor. The white square box outline on the contours represents the VAWT. With the comparison to ascertain the effects of wake recovery of the 3-D structures of the near and far wake for the above mentioned different models: the wake topological differences for wake velocity deficit in experimental data are remarkably different for the positive pitch case, this is evident from the mushroom-shaped cloud formation of wake seen in the contours above. Comparing the normalized velocity (U/U_∞) in the cross-flow region (Y/D) to the position of the rotor a larger deflection towards the negative-Y Sector is seen, with the bulging/ expanding of the mushroom dome in the negative-Y sector with the increase in rotor downwind distance. This is a clear attribute to the larger side forces generated by the positive pitching of blades on VAWT. The momentum behind the negative Y sector of the rotor which turns into the wind is significantly lower than behind the positive-Y sector. The velocity deficit profile normalized by the free stream velocity is shown in the figure 4.20 caused by the blade rotation.

Comparing the experimental results to the CFD simulations, for the near and far wake, the CFD model comes close to representing the wake distribution for the positive pitch case with respect to all other shown models. There is a slight discrepancy in representing the recovery in wake normalized velocity, the CFD model shows a higher recovery compared to experimental results in the spatial wake distribution for far-wake as seen in the contour plots, whereas the expansion of wake in negative-Y direction (cross-flow width) is larger in the experimental case compared to the CFD model. The vertical profile of the normalized velocity (U/U_∞) in span-wise width (Z/D) shows wake recovery profile is almost symmetric on both sides above mid-span and below mid-span (with the center of the rotor being at $Z/D=0$) such that it is seen that the upper portion of the wake is been replicated in the down region but the except on the negative Y-direction a downward swept pool caused by the turbine tower. As can be observed from the contours in the far wake (8D), only wake in the upper half-plane is been measured, due to the higher expansion and difficulty to capture the wake in a single plane, an assumption is made here, the lower part of the wake to be symmetric to the upper half for further calculations. However, the Gaussian wake model and the Jensen wake models are not able to capture the spatial wake distribution and its shape attributes, this is because of the reason that the Gaussian, Jensen models are based on the classical actuator disc model of conservation of mass and momentum whereas, the VAWT acts as an actuator cylinder model. But with regards to maximum wake velocity deficit, along the cross-flow and stream-wise direction, the Gaussian model is in good agreement with the experimental and CFD model, this is discussed further in this section.

Based on the comparison of the positive pitched contours to the baseline case (zero angle deflection) for experimental results there is a drastic difference in the wake topography, the positive pitch case shows a mushroom cloud-shaped wake, where the zero pitch case has an irregularly shaped wake structure. a similar observation can be made for the CFD model as well. In both cases, the normalized wake is deflected towards the negative-Y direction(crossflow), but in the case of the positive pitch (P10),

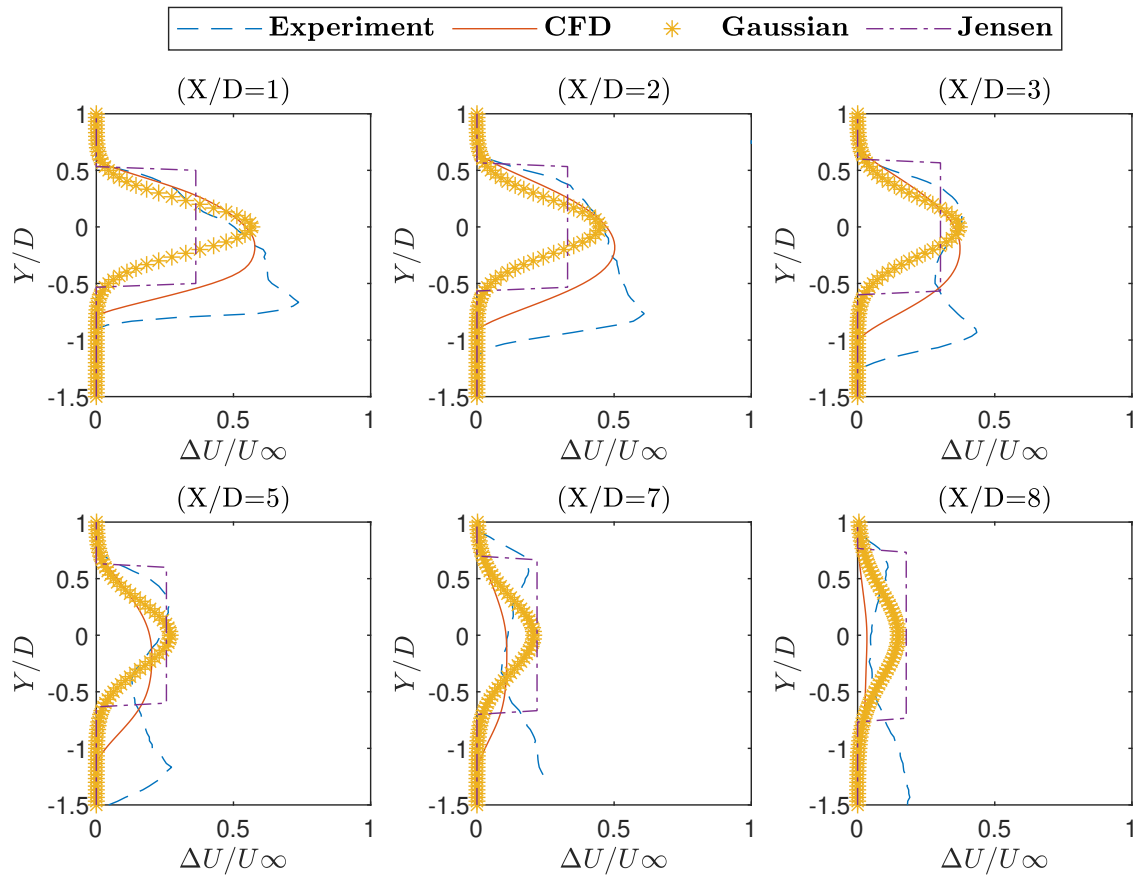


Figure 4.18: A comparison between Experiment data, CFD, Gaussian, Jensen wake model for downwind profile of centerline streamwise velocity deficit normalized by (U_∞) at $(X/D=1,2,3,5,7,8)$ for positive 10° pitch angle

the measure deflection is larger to the zero pitch case (P0), whereas in the positive-Y direction the expansion of wake in (P10) case again is slightly more than that of the (P0).

The vertical profile of the normalized velocity (U/U_∞) in span-wise width (Z/D) shows that the wake for the (P10) case expands higher in the near wake region whereas the wake expansion is almost the same in the far wake. For both cases, the wake in span-wise direction is almost symmetrical on both sides to the center of the rotor. Analyzing the wake recovery, it is observed that the (P10) case shows a higher recovery in the wake, with respect to the (P0) case. The figure 4.21 shows contours of positive 10 degrees pitch case stream-wise velocity deficit at different downstream positions $(X/D=1,2,3,5,7,10)$ normalized by the free stream velocity. In-plane velocity vectors are overlaid. The outline of the rotor is delineated by a black box. The in-plane velocity vectors disclose the trace of at least two pairs of stream-wise CVPs this can be seen in the same figure with the effect of these CVPs the wake shape is quickly deformed along with the stream-wise distance. The Gaussian and Jensen models are almost similar in both cases, just, a smaller change in Drag force and Drag force coefficient is observed, higher Drag force and the coefficient is measured in case of (P10), which results in a slightly higher wake velocity deficit in (P10), wake models.

Figure 4.18 presents a detailed comparison between theoretical wake models, the experimental data, and the CFD model for the P10 case. Here maximum stream-wise velocity deficit normalized by the free-stream wind velocity $(1 - \frac{U}{U_\infty})_{max}$ over each stream-wise measurement plane (near wake and far wake) is plotted against the cross-flow width of the wake. It can be noted here from previous findings that the maximum stream-wise velocity deficit coincides with the center-line velocity of the wake cross-section. The experimental data (dotted blue line), CFD model (Solid redline), Gaussian model by Mahdi Abkar (star orange), Jensen wake model (magenta solid line). Comparing the four models, it can be seen for the experimental results and CFD model, that in the negative-Y direction and also from

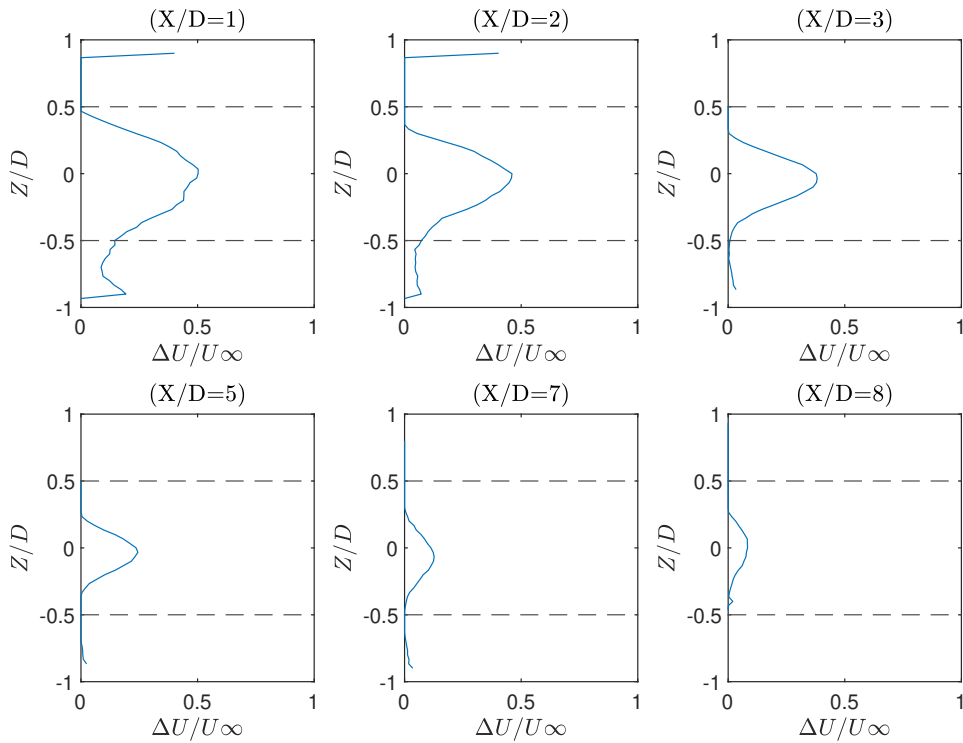


Figure 4.19: Vertical profiles of centerline streamwise velocity normalized by the (U/U_∞) wind-speed (at the midspan for different rotor downwind distance $(X/D=1,2,3,5,7,8)$ for positive 10° pitch angle

the above contour plots the wake is highly deflected in this P10 case. The maximum wake velocity deficit /center-line wake deficit in near wake has been under-predicted by the CFD, Jensen model and over-predicted in far wake. Whereas the Gaussian model predicts the wake velocity deficit in both near and far wake in close agreement with the experimental data, but it cannot capture the deflection in the wake. Also, the experimental data is seen with two peaks, which is not in agreement with the Gaussian wake model [1]. The CFD model performs better at far wake distances rather than the close wake, and it represents the spatial distribution and structure of the wake in good agreement. The Jensen model is the least accurate and cannot represent the wake phenomenon well.

Comparing the velocity deficit normalised with the free stream velocity for (P10) and baseline case it is clearly observed that the velocity deficit is recovered faster in the (P10) case both in near and far wakes (At $X/D=3$, $X/D=8$ P0 $(1 - \frac{U}{U_\infty})_{max} = 0.7, 0.2$ whereas for P10 case $(1 - \frac{U}{U_\infty})_{max} = 0.5, 0.2$ respectively for the experimental case). The Gaussian-based wake model is good in predicting the wake velocity deficit for the (P10) case rather than the (P0) case, but again cannot account for deflection and wake shape. The deflection in the wake of the experimental case for near and far wakes can be seen in figure 4.20 dotted blue line Experimental wake, solid red line Gaussian-based wake model. Note the shift in wake to the negative-Y direction which is not quantified by the Gaussian-based wake model, and the two peaks in experimental data slowly come to the same height in far wake representing faster wake recovery. The Gaussian wake model is able to quantify the wake deficit well, but not the shape. Figure 4.19 shows the vertical profile of wake velocity deficit mid-span downwind, it can be noted here again the wake is almost symmetric in both halves of the plane and recovery is faster compared to the (P0 case).

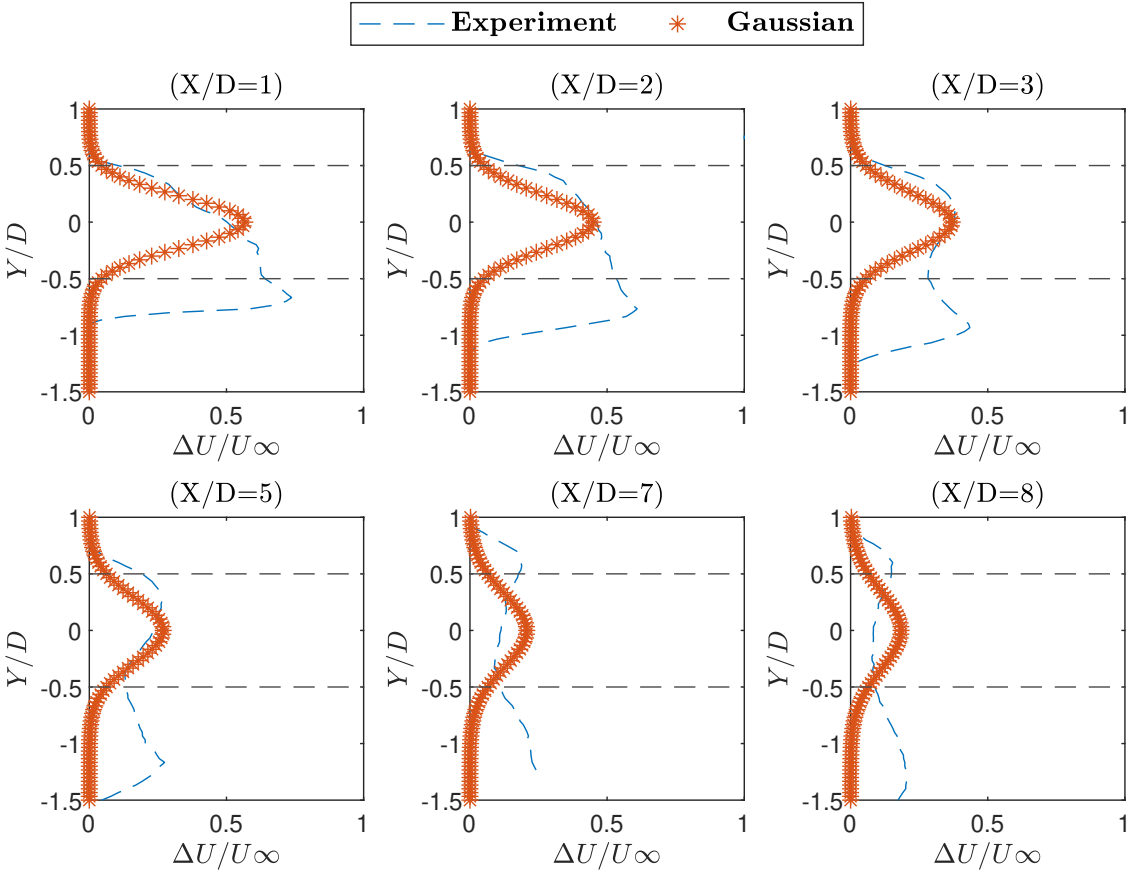


Figure 4.20: Crosswind profile of the centerline streamwise velocity deficit normalised by (U_∞) (at midspan). (Dotted line) experimental data (solid line) CFD data at ($X/D=1,2,3,5,7,8$) for positive 10° pitch angle

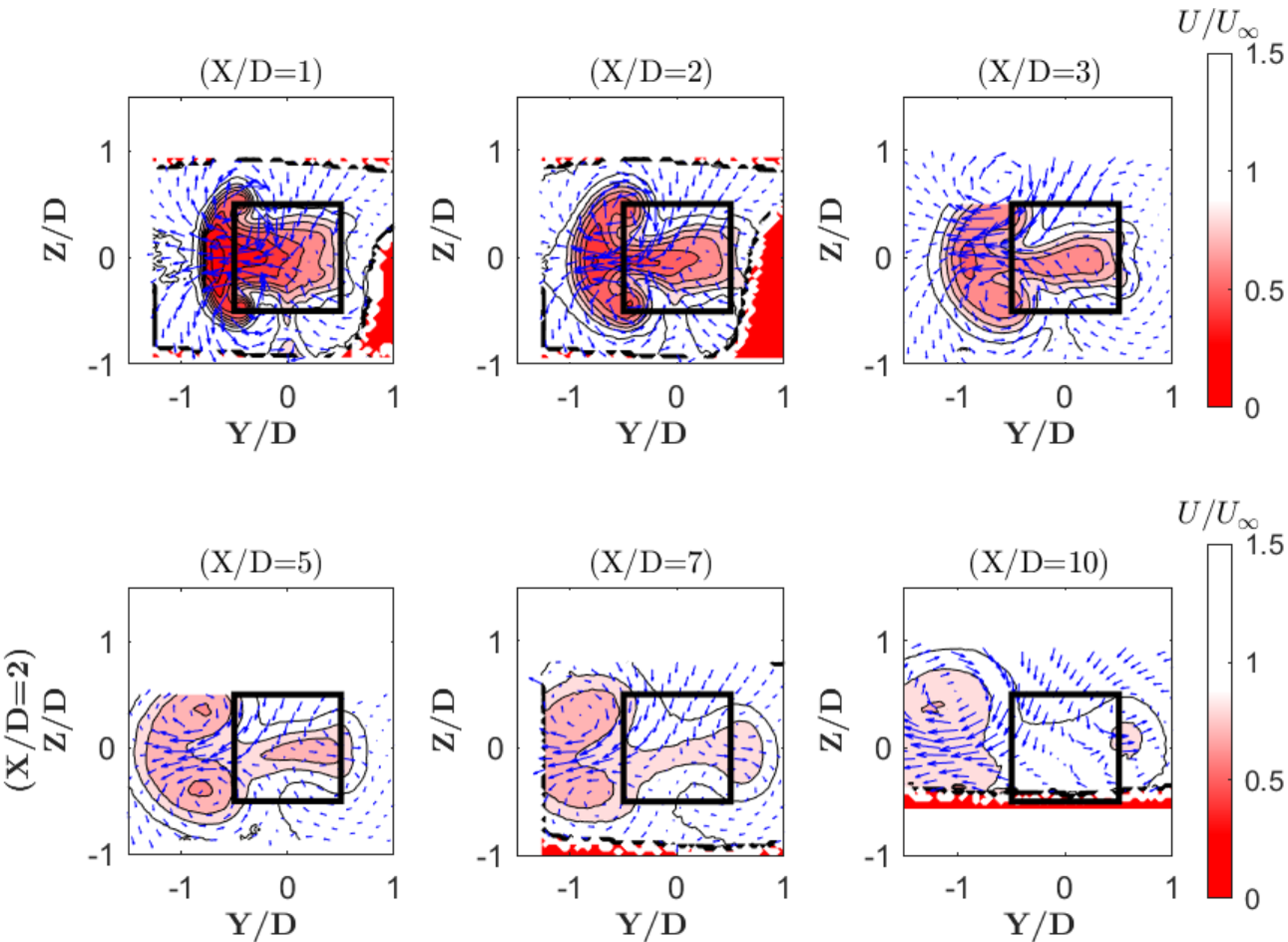


Figure 4.21: Contours of positive 10^0 pitch case streamwise velocity deficit at different downstream positions ($X/D=1,2,3,5,7,10$) normalized by the free stream velocity. In-plane velocity vectors are overlaid. The outline of the rotor is delineated by a black box.

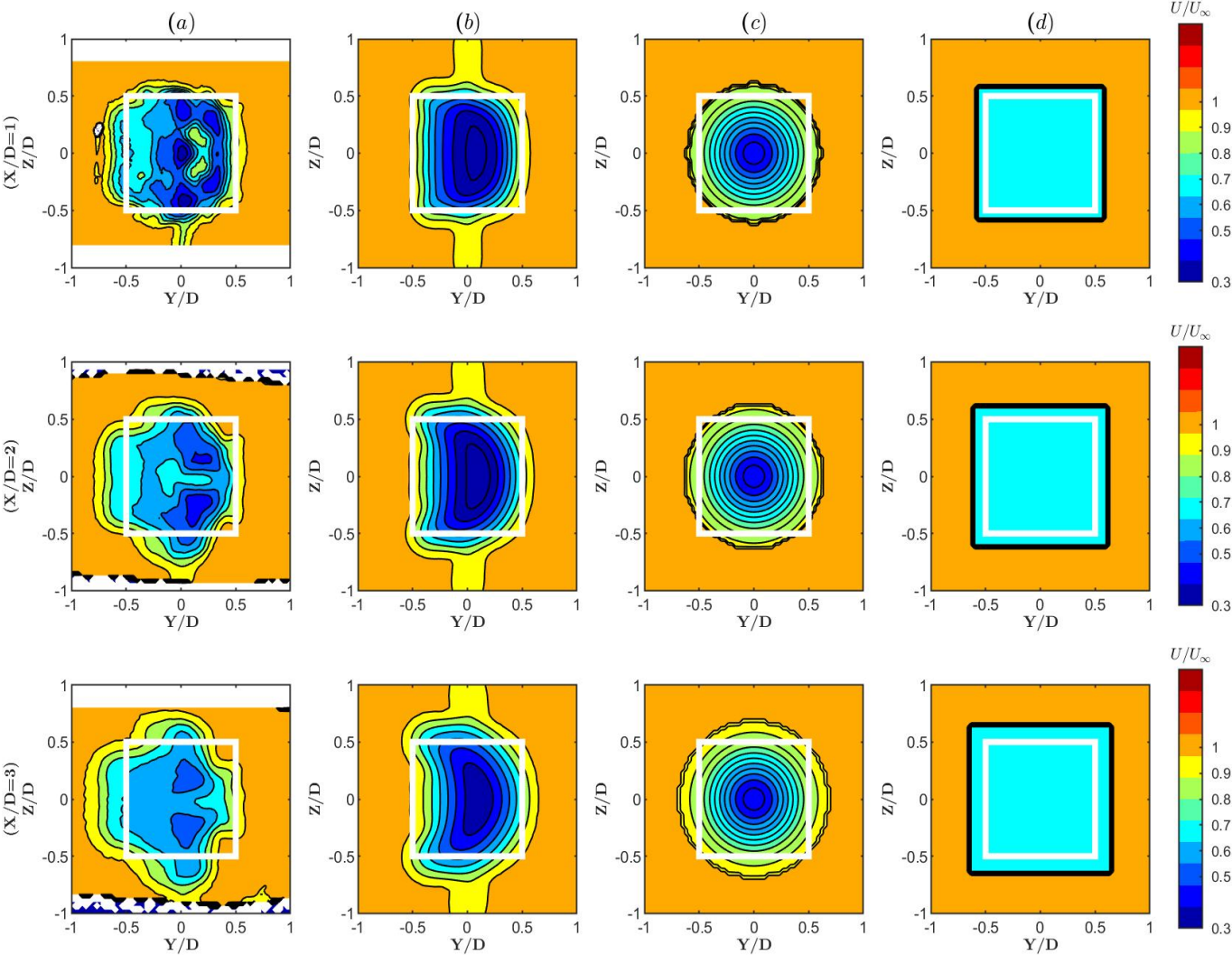


Figure 4.22: Contours of streamwise wake velocity at different downstream positions near wake ($X/D= 1,2,3$) normalized by the free stream velocity (U_∞) for negative 10° pitch angle

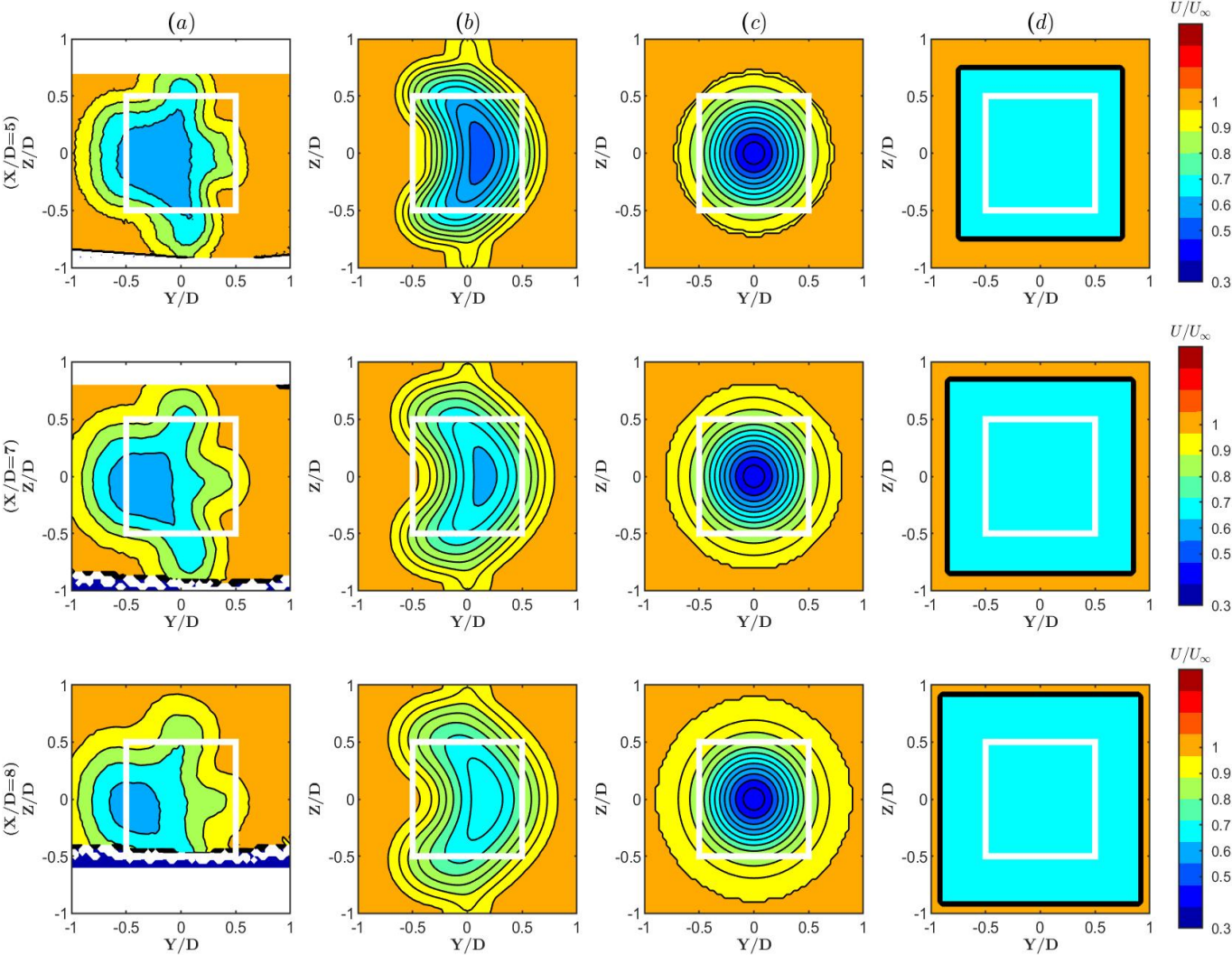


Figure 4.23: Contours of streamwise wake velocity at a different downstream position far wake ($X/D= 5,7,8$) normalized by the free stream velocity (U_∞) for negative 10° pitch angle

A similar comparison to the previous cases (P0) zero degree pitch angle and (P10) positive 10-degree pitch angle of time-averaged stream-wise velocity normalized by the U_∞ is shown above figure 4.22, 4.23: for (N10) negative 10 degrees pitch angle from left (a) experiment result , (b) CFD result ,(c) Gaussian model by Mahdi Abkar based on theoretical wake development work of M. Bastankhah, F. PortéAgel, and lastly the (d) Jensen wake model for near wake ($X/D = 1,2,3$), far wake ($X/D=5,7,8$) at tipspeed ratios of $\lambda= 2.513$. While the white outline is the projection of the small VAWT with a length of 300 mm and a width of 300 mm. The zero on both the X and Y-axis represents the absolute center of the VAWT. Here the parameters for the construction of theoretical models are the same as above mentioned for (P0) and (P10) case, only the Drag force and Drag force coefficient are used from measurements from the force balance, ($T_D= 0.8119 \text{ N}$ $C_D =0.5891$, for negative pitch angle on VAWT). With the comparison to see the effects of wake recovery of the 3-D structures of the near and far wake for the four presented models above, the topological, deflection of wake are different as well as interesting in the light of the previous cases.

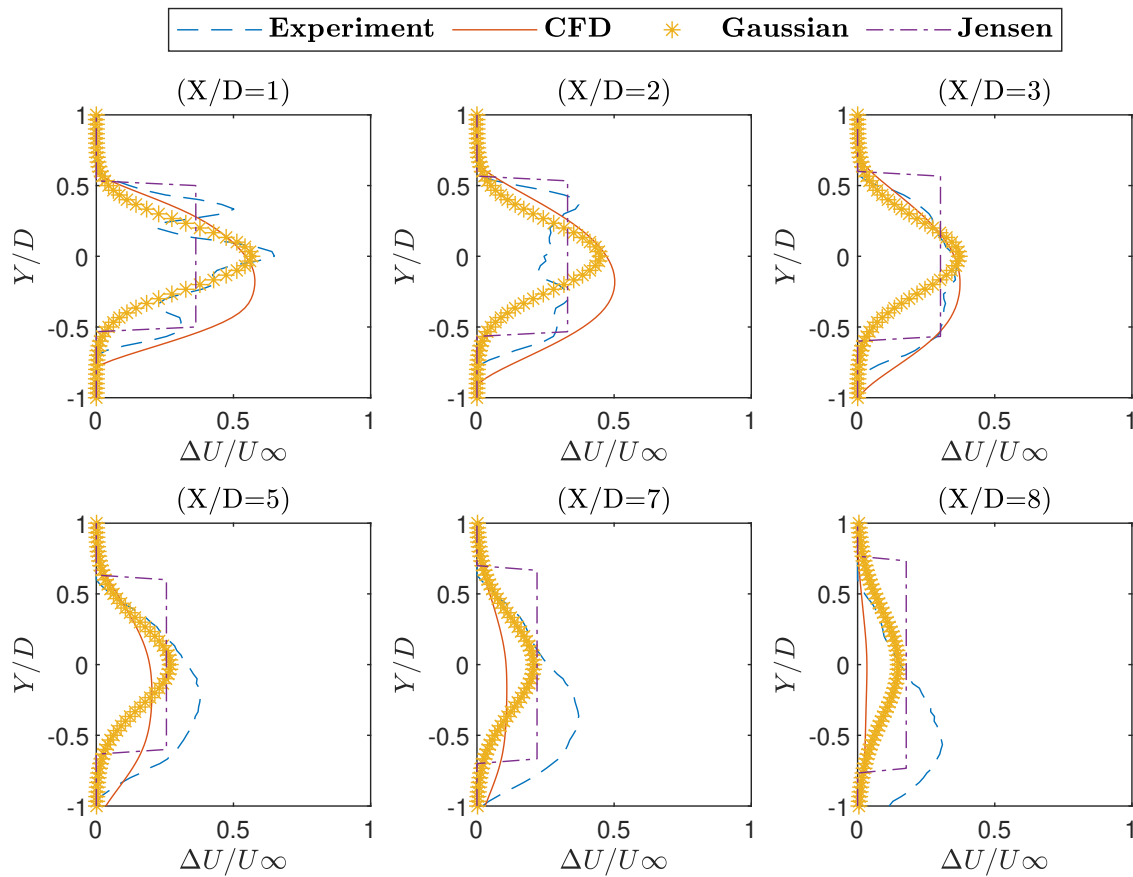


Figure 4.24: A comparison between Experiment data, CFD, Gaussian, Jensen wake model for downwind profile of centerline streamwise velocity deficit normalized by (U_∞) at ($X/D=1,2,3,5,7,8$) for negative 10° pitch angle

For the negative pitch case (N10) it can be observed the deflection in the cross-flow direction is been reduced when compared to the positive (P10) and zero pitch (P0), largely on the negative-Y direction, also the expansion of wake for (N10) case in cross-flow direction is less with respect to other two. The span-wise width of the N10 case is higher than the other two cases, In (N10) the wake expands more in the vertical direction. comparing the normalized wake velocity (U/U_∞) for three cases, the wake structure for the (N10) case is more compact, less expanding, and shows the least recovery in wake velocity in both near and far wake region. Seen in the contour plot With dark blue in the center of wake structure very slowly recovering with a color bar shift of chrome yellow in the edges. The CFD model here also can not predict the spatial distribution of the wake very well, as compared to the first and second cases. The CFD model shows inaccurate wake characteristics in far wake, with the wake de-

flecting towards the positive-Y direction, rather than the negative side. This is in disagreement with the experimental results, also the CFD contour shows faster recovery in wake compared to experimental results. The figure 4.26 shows contours of negative 10 degrees pitch case stream-wise velocity deficit at different downstream positions ($X/D=1,2,3,5,7,10$) normalized by the free stream velocity. In-plane velocity vectors are overlaid. The outline of the rotor is delineated by a black box. Looking closely at in-plane velocity vectors at $X/D=2,3,5,7$ show a sign of vortices in the wake structure. The Gaussian-based wake model produces the wake velocity in good agreement to the experimental results for this case, but cannot account for the topological characteristics, such as wake deflection and change of wake 3d structure. Whereas, the Jensen model is the least accurate one here, with no accounting for wake structure as well as correct wake velocity.

Figure 4.24 presents a detailed comparison for maximum stream-wise velocity deficit normalized by free stream velocity between theoretical wake models, the experimental data, and the CFD model. It can be observed, in the figure, that the maximum wake velocity deficit /center-line has been deflected towards the negative-Y direction in far wakes, for the experimental case (blue dotted line). The Gaussian model here (orange star) represents the wake velocity deficit with good agreement to the experimental data in near wakes, whereas in the far wake the same model slightly under-predicts the values. The CFD model over-predicts the deficit for all the near and far wake cases. The CFD model for the (N10) case is not in good agreement as compared to the previous cases where the CFD models were more explicate in representing the experimental results. The wake velocity deficit ($\Delta U/U_\infty$) for far wake are higher in the (N10) compared to the previous two cases. Which also again points to the slow recovery in the wake. Both the theoretical models as well as CFD model, in this case, do not take into account the wake deflection. The figure 4.25 shows a comparison of experimental results and Gaussian model, see how the Gaussian model is close in representing thfig:Vertical profiles of stream wise velocity normalized2Ne wake deficit, and performs quite better in near wake than in the far wake region, also it forgets to account for wake deflection. Finally, the vertical profile of the wake deficit can be seen in figure 4.27 the wake profile in span-wise width both the expansion as well as wake deficit are higher in (N10) compared to P0 and P10 cases.

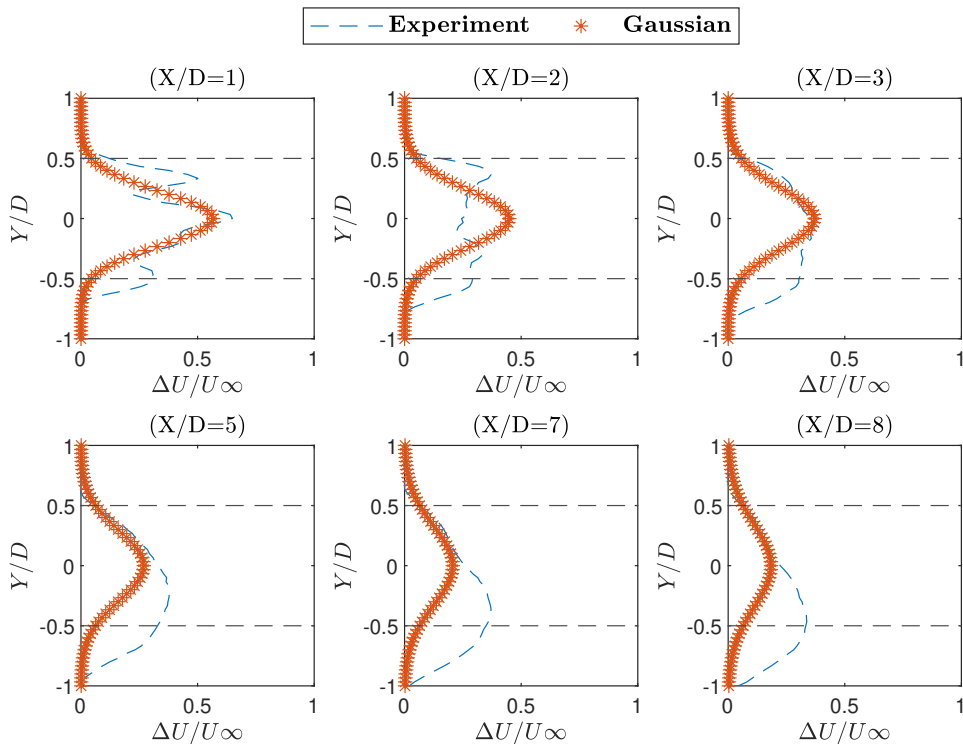


Figure 4.25: Crosswind profile of the centerline streamwise velocity deficit normalised by (U_∞) (at midspan). (Dotted line) experimental data (solid line) CFD data at ($X/D=1,2,3,5,7,8$) for negative 10° pitch angle

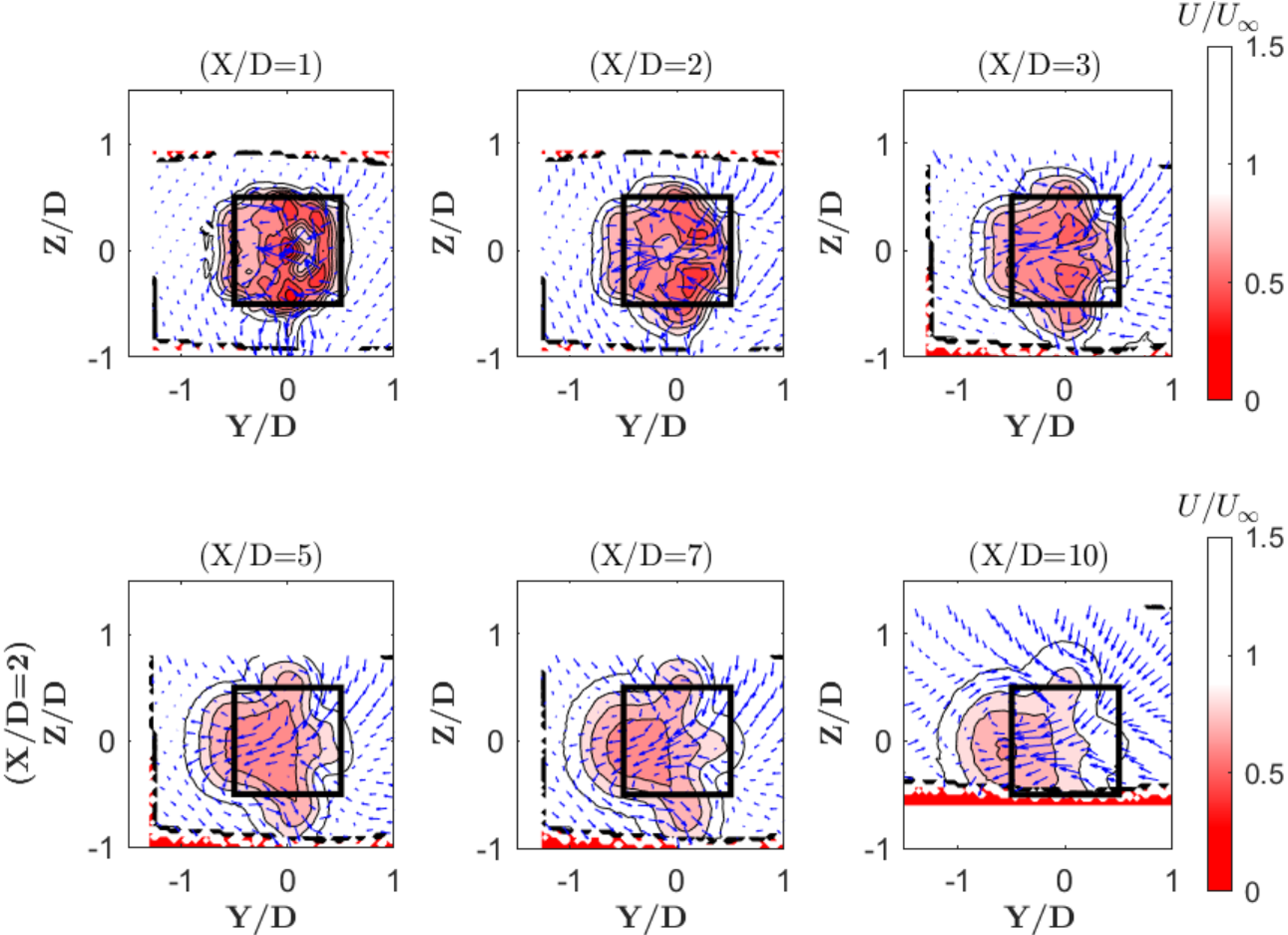


Figure 4.26: Contours of negative 10^0 pitch case streamwise velocity deficit at different downstream positions ($X/D=1,2,3,5,7,10$) normalized by the free stream velocity. In-plane velocity vectors are overlaid. The outline of the rotor is delineated by a black box.

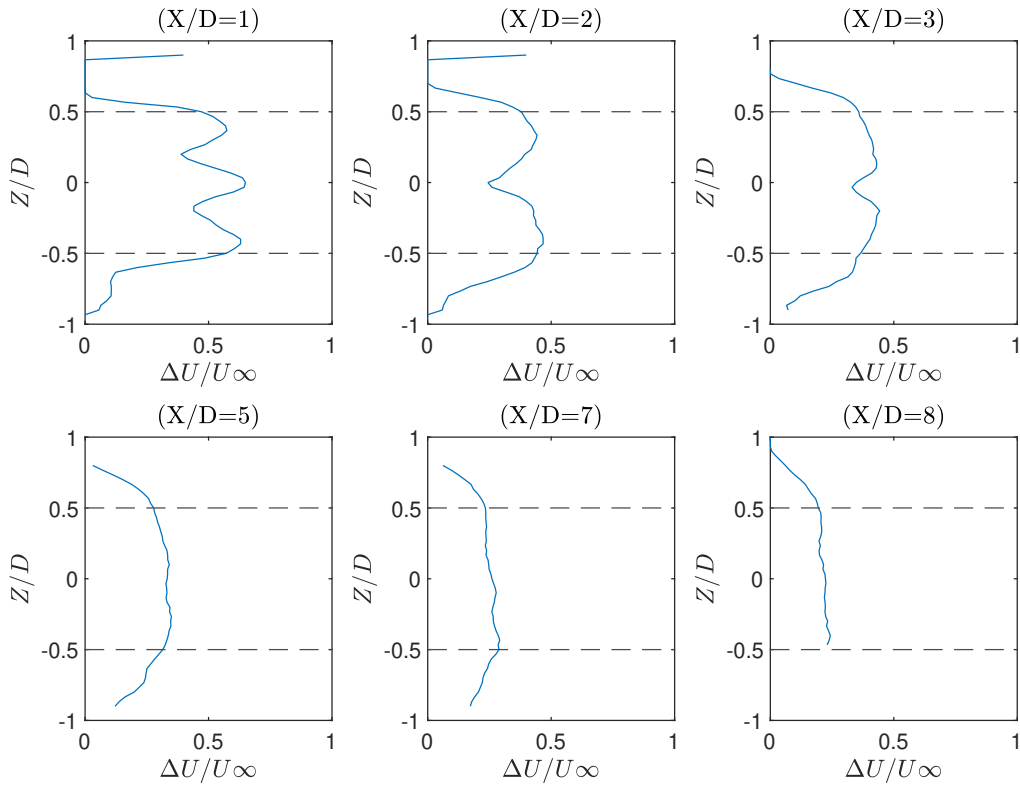


Figure 4.27: Vertical profiles of centerline streamwise velocity normalized by the (U/U_∞) wind-speed (at the midspan) for different rotor downwind distance ($X/D=1,2,3,5,7,8$) for negative 10° pitch angle

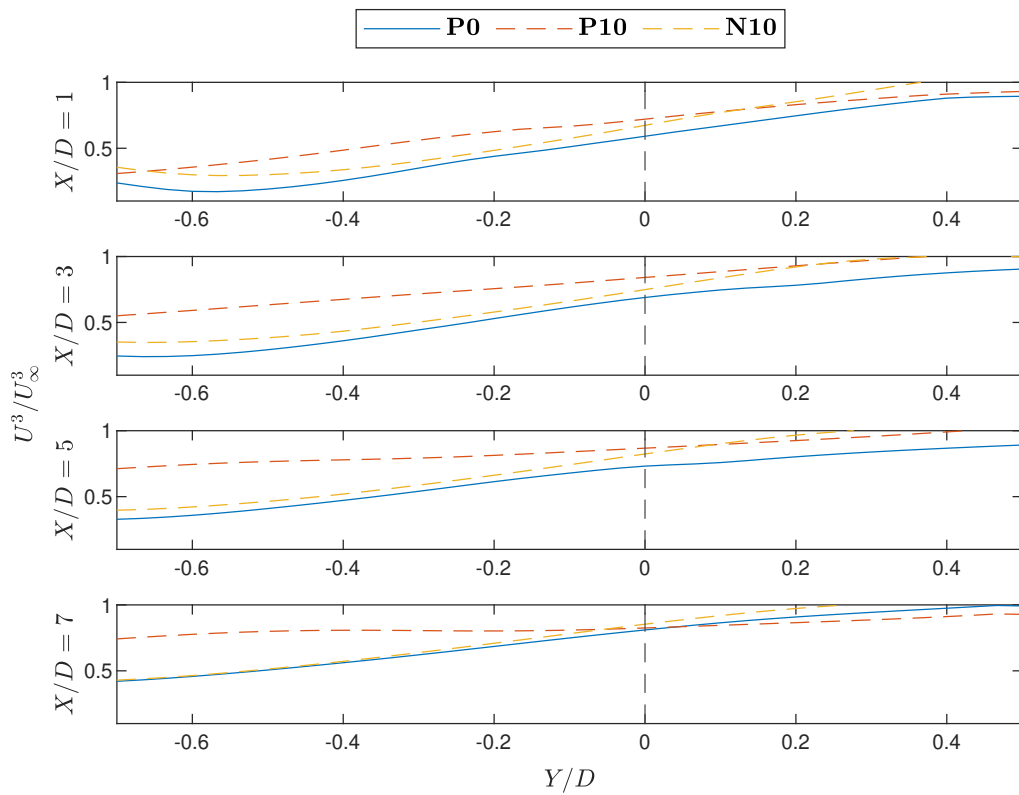


Figure 4.28: Available power distribution along with the crosswind profile at $X/D = 1, 2, 5, 7$ for baseline, positive 10° , negative 10° case for experimental results

4.3. Available Power for Hypothetical Downwind Turbines

To calculate the impact on available wind power (AP) distribution on a hypothetical turbine downwind of an upstream VAWT, in zero pitch, positive 10 degrees pitched and negative 10 degrees pitched conditions. A moving integration method is adopted here, thereby integrating the frontal area of a hypothetical downwind VAWT. The schematics of the method are shown in figure 4.29. The integration is given by :

$$f_{AP}(x_T, y_T, z_T) = \iint G^{u^3}(x_T, y', z')/U_\infty^3 dz' dy' \quad (4.4)$$

$$\text{where } G : |y' - y_T| \leq 0.5|z'| \leq 0.5 \quad (4.5)$$

The behind wake contour is the integrated quantity to be, in our case the normalized stream-wised wind power U^3/U_∞^3 the white square outline represents the upstream VAWT creating the wake contour. The other window (solid black line) represents the integration window, which has a similar dimension to the rotor of VAWT (length =300 mm and width=300 mm). The coordinate system, especially the horizontal axis Y, becomes negative when moved in left and visa-versa, as the zero on both the X and Y-axis represent the absolute center of the VAWT upstream. The integration is calculated by moving the window 0.03D every time and integrating the whole contour plane from extreme negative-Y to extreme positive-Y, in order to observe the change in available power, for four different positions downstream ($X/D=1,3,5,7$) and three different pitch angles. The C_T for each pitch case is calculated using the force balance measurement system described in the previous section.

The AP for the three different pitches, and downwind is seen in figure 4.28. For the first rotor diameter the P10, P0, and N10 show a similar trend showing a higher available power on the positive right side. Here the wake is at a stage where the large deformations and recovery have not yet taken place. The wake in the P10 case is deflected quickly and the recovery is faster than the other two pitch angles, so it can be observed that a recovery in the available power to almost above 0.5 at 3D and which keeps on increasing as the increase in downwind distance. The AP of P10 pitch reaches value of 0.70 at 5D compared 0.77 at 7D where it is seen to come to an almost plateau. Because the deflection is slowed down, due to an almost smeared out of stream-wise vorticity, and wake recovery at this position also the turbulence transport is dominant, just like the classical shear dominated turbulent wakes. Compared to the P10 case, a 0.40, 0.42 AP for the N10 case and 0.35 and 0.42 for the P0 case were observed at $X/D=5,7$ respectively. The zero on the x-axis marks the upstream turbine center, The available power for the P0 case is higher in the far wake as the AP jumps from 0.35 to 0.42 from 5D to 7D. The N10 shows a higher recovery in the positive Y direction because the wake expansion observed in the N10 case is least and the ends of the expanded wake almost reach the position(extreme positive-Y position).

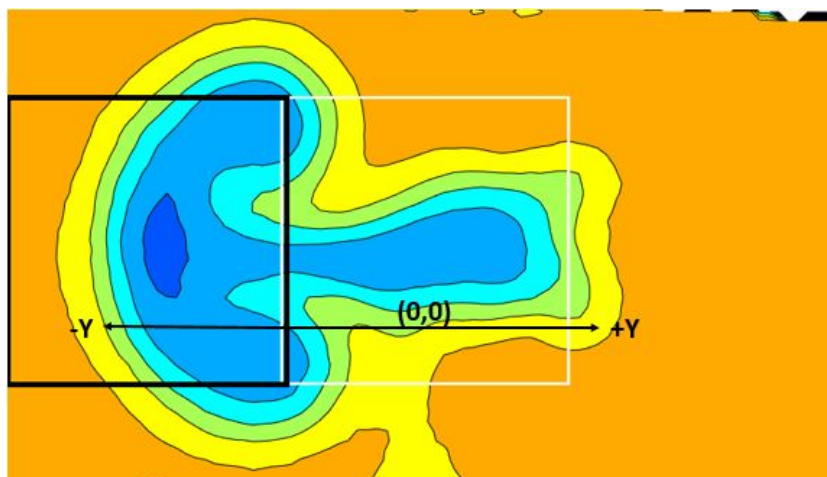


Figure 4.29: Moving integration window (solid black line), the outline of upstream VAWT (solid white line), Left negative Cross-flow width, and vice versa

A similar concept of moving integration window for determining the impact on available wind power (AP) distribution on a hypothetical turbine downwind of an upstream VAWT, been applied for the CFD simulations seen in figure 4.30. The integrated quantity, here is normalized stream-wise wind power U^3/U_∞^3 . Both the experimental and CFD simulations show similar trends for the three-pitch angles at different rotor downwind distances. At $X/D=1$ the wake is not completely matured/expanded and the major available power is seen in the leeward side the positive-Y direction for all the three-pitch angles. The P10 case recovers faster compared to the P0 and N10 case with rising in available power from 0.7 to 0.8 in the negative-Y direction from $X/D=5$ TO $X/D=7$, which is the highest seen recovery in the wake. The CFD simulation shows a higher recovery in available power for the P10 case compared to the experimental results. For the P0 and N10 cases, the recovery in AP is seen to be similar in both CFD simulation and experimental results. For the CFD simulations, a higher recovery rate for AP over the cross-flow width is seen in the P0 zero pitch case against the N10 negative pitch case. The important thing to note here is the CFD simulations account for the deflection in wake and associated available power with it.

The concept of moving integration window and available power downwind of an upstream VAWT, has

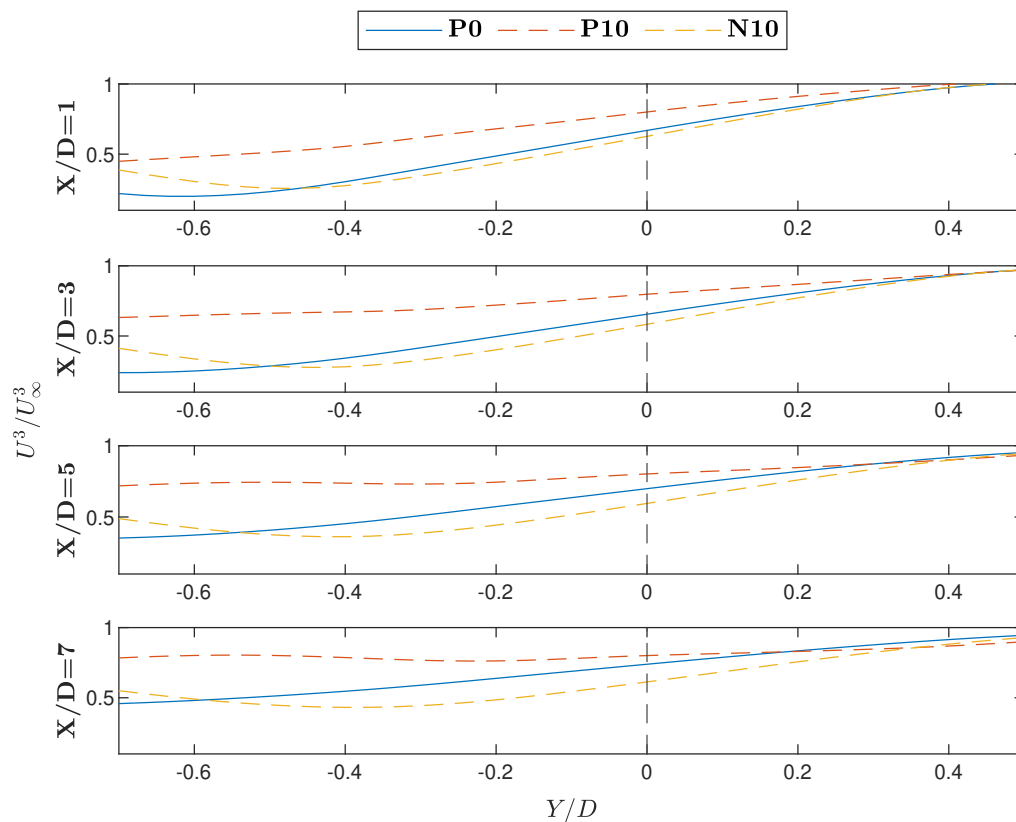


Figure 4.30: Available power distribution along the crosswind profile at $X/D = 1, 2, 5, 7$ for baseline, positive 10° , negative 10° case for CFD simulations

been applied for the Gaussian wake model for VAWT by M Abkar [1] and Jensen wake model [20]. For a zero pitch angle case, both the models will show a similar trend for VAWTs and HAWTs as well (when the wake expansion rate in both cross-flow direction and span-wise direction is considered to be the same for simplicity), as these models work on the actuator disk concept. The compared case in the figure 4.31 shows the AP for zero pitch angle case with a $C_T = 0.6828$. Both the models show alike trends in near and far wake, with a dip in AP immediately behind the rotor and a seen recovery in far wake. Jensen model under-predicts the recovery with respect to Gaussian based wake model (considering Gaussian wake model to be more accurate from above findings). The higher available power is seen to be almost 1 diameter in the cross-flow direction from the center of the upstream turbine, but the following models fail to account for deflection in the wake and associated AP with it.

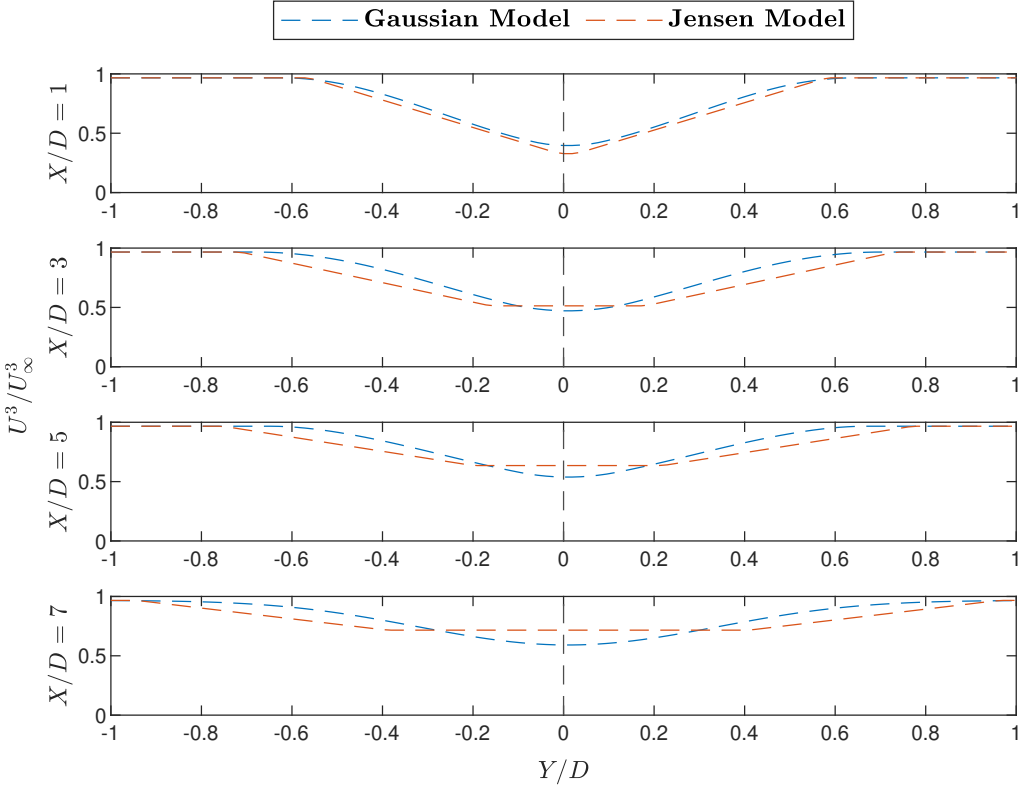


Figure 4.31: Available power distribution along with the crosswind profile at $X/D = 1, 2, 5, 7$ for Gaussian wake model by M Abkar, and Jensen wake model

5

Summary, Conclusions, and Future Work

5.1. Summary and Conclusion

Using stereo-PIV techniques in a wind tunnel, the wake behind a small VAWT with a free stream of 5 m/s is quantified and analyzed. The experimental results are used to compare a CFD simulated model, a Gaussian model for VAWT by Mahdi Abkar based on previous work on HAWT by M. Bastankhah, F. Porté-Agel, and lastly Top-Hat wake model by Jensen. A force balance measurement technique is developed to measure the accurate lift and drag forces on the rotor structure. Several interesting characteristics of the wake are observed. Possibly the most notable feature of the flow is the deflection of the wake towards the windward side (cross-flow width), negative-Y in this case. Three different pitch angles are introduced on the rotor blades P0 (zero pitch angle case), P10 (positive 10 degrees pitch angle case), and N10 (negative 10 degrees pitch angle case). The maximum amount of deflection in the wake towards the negative-Y direction was quantified for the P10 case. The wake shift in the negative-Y direction can be caused by the blade rotation, with the clockwise rotation of the vertical axis rotor, and the rear blade turning into the incoming flow of wind. Comparing the theoretical models, the Gaussian model represents the wake deficit in close agreement to the experimental results but fails to account for change in wake structure, deflection in the wake (and wake recovery especially the Jensen model).

The theoretical models fail to reproduce the wake characteristic of VAWT due to the fact that the VAWTs act as an actuator cylinder model rather than the actuator disk concept and is expected to exert lateral forces, during the rotation on the wind by conservation of momentum. Whereas the Jensen and Gaussian-based wake models are based on the classical actuator disc model. Jensen's model utilizes the mass conservation together with the one-dimensional momentum theory and considers a top-hat shape for the wake deficit. The Gaussian model, in which the mass and momentum are conserved, assumes that the velocity deficit has an elliptical Gaussian shape. The wake recovery for VAWT in the P10 and P0 case is far better than the N10 case, and an interesting wake mushroom-shaped cloud is observed in the wake P10 case. During the rotation, the blades of VAWTs exerts both a stream-wise and a lateral force on the wind by conservation of momentum due to continuity, this crosswind force introduces crosswind momentum to the flow, this is observed through the in-plane velocity vectors and as a result gives rise to the occurrence we have associated with the production of a CVP (counter-rotating vortices). This is also reported in previous studies [37]. Analyzing the in-plane velocity vectors, wake structure, and fluxes of momentum in the wake indicated that these CVPs are one of the important mechanisms in introducing momentum to the wake. The CVPs are also observed with the wakes of yawed HAWTs, including not only the production of CVPs but also the lateral deflection of the wake center in the same direction as the velocity induced by the rotor. The high-velocity gradient on the boundary of the wake behind the negative-Y sector of the rotor gives rise to peak turbulence levels

and encourages mixing in this region. For the vertical wake velocity in the span-wise direction, the wake recovers asymmetrically as more momentum is entered from the faster moving flow above the wake. Also, the wake in span-wise direction is found to be almost symmetrical on both halves of the plane,(considering the rotor center as the actual center for the plane).

Closely studying the work of Rolin, F. Porte-Agel[37], it is identified that turbulence plays a large role in mixing momentum and re-energizing the wake. It is also observed that the highest levels of turbulence mixing of the wake occur at the periphery of the wake. The CFD simulations are a very good representation for wake characteristic and are in good agreement with the experimental results for taking into account deflection in the wake, wake topography and wake recovery is far wake, with a slight discrepancy in the CFD models for the N10 case fail to reproduce the wake characteristics, whereas the wake deficit obtained are not in good agreements with the experimental results. The N10 case has the lowest seen recovery in the wake also has a lower wake expansion in cross-flow direction compared to other cases.

For the maximum velocity deficit normalized by free stream velocity ($\Delta U/U_\infty$) (center-line deficit) in the cross-flow direction in accordance to the experimental results the CFD model accounts in good agreements for the wake deflection, changes in wake structure, and maximum velocity deficit for P0 case and P10, but poorly represent this characteristic for N10. Also, the CFD model represents the wake characteristics well in the far wake region compared to the near wake. Regarding the top-hat model by Jensen, although this approach is not able to capture the spatial distribution of the wake correctly and under predicts in the near wake region and over predicts in the far region, it is still beneficial and useful due to its simplicity and its consistency with the widely used Jensen model for wind turbine wakes. The Gaussian based wake model by Mahdi Abkar based on theoretical work of M. Bastankhah, F. Porté-Agel represents the wake velocity deficit and expansion of wake in close agreements to P10 and N10 case in both near and far wake, whereas for the P0 case it mostly under-predicts these value shower higher recover than actual. But to note the Gaussian model does not account for the deflection caused in the wake, also it fails to produce the change in wake characteristics(related to wake geometry).

The available power for hypothetical downwind turbine for both experimental results and CFD simulations is observed to be higher for all cases on the positive-Y section, due to deflection in wake towards the windward side, a negative-Y section in our case. Also to note here the wake in the P10 case is deflected quickly and the recovery is faster than the other two pitch angles: and the available power at 7 rotor diameter is about 80% of free stream velocity compared to 45% recover for the other two cases. The N10 case recovers the slowest throughout the whole wake cross-flow width. The downstream available power for the analytical wake models is highest after 1 diameter offset to the upstream rotor in a Cross-flow direction. The force balance fabricated for this experiment gives an accurate estimation of drag and lift forces and their coefficients when compared to other similar literature and experimental campaigns.

It still remains unclear why there is such a discrepancy between VAWT wakes for span-wise width observed in the literature. In the case studied here, it seems clear that the wake velocity in span-wise direction propagates almost symmetrical in both halves of the time-averaged stream-wise wake cross-section plane (rotor center aligning the center of the plane). It may prove to be the case that the tip-speed ratio implemented in this study ($\lambda = 2.513$) results in a symmetrical aerodynamic behavior of the wake in span-wise width, whereas the literature studies are based on a lower tip-speed ratio, which results in highly asymmetric aerodynamic behavior, as the flow relative to the blade will fluctuate highly as the VAWT rotor spins. Also, in literature [37] the case of boundary layer effect causes the wake to be asymmetric for the referred above: compared to our experimental cases where there is no boundary layer effect present.

5.2. Future Scope

The following study addresses the wake characteristics and their effect on a single turbine (with three different pitch angles). The experiments carried out also contain cases with two turbines the first one

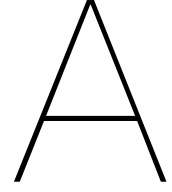
with pitch angles and the second turbine in inline and offset conditions to the first one. This experimental data can be used to realize the wake model for wake superposition and the validity of analytical methods can be explored. Also, a unique condition for wake superposition was created in the experiments where the free-stream wind velocity is adjusted according to the lift and drag forces experienced by the second turbine, when in inline with the first turbine, and similar conditions are achieved to understand the wake superposition. A check for available power downstream of the first (upstream) rotor can be done with the hypothetical study consideration in this thesis. This good resource of data can provide a good understanding of wake propagation and its characteristics for multi-turbine scale and its superposition effects, and the power available for the downstream turbines. Furthermore efforts can be taken to study the changes in wake with different rotor aspect ratios.

References

- [1] Mahdi Abkar and John O. Dabiri. "Self-similarity and flow characteristics of vertical-axis wind turbine wakes: an LES study". In: *Journal of Turbulence* 18.4 (2017), pp. 373–389. ISSN: 14685248. DOI: 10.1080/14685248.2017.1284327. URL: <http://dx.doi.org/10.1080/14685248.2017.1284327>.
- [2] J F Ainslie. "Journal of Wind Engineering and Industrial Aerodynamics, 27 (1988) 213-224". In: *Journal of Wind Engineering* 27.1-3 (1988), pp. 213–224. URL: <http://linkinghub.elsevier.com/retrieve/pii/0167610588900372>.
- [3] B. Akay et al. "Investigation of the root flow in a Horizontal Axis". In: *Wind Energy* May 2013 (2013), pp. 1–20. DOI: 10.1002/we.
- [4] Daniel B. Araya and John O. Dabiri. "A comparison of wake measurements in motor-driven and flow-driven turbine experiments". In: *Experiments in Fluids* 56.7 (2015), pp. 1–15. ISSN: 07234864. DOI: 10.1007/s00348-015-2022-7.
- [5] Peter Bachant, Anders Goude, and Martin Wosnik. "Actuator line modeling of vertical-axis turbines". In: (2016), pp. 1–20. arXiv: 1605.01449. URL: <http://arxiv.org/abs/1605.01449>.
- [6] Majid Bastankhah and Fernando Porté-Agel. "A new analytical model for wind-turbine wakes". In: *Renewable Energy* 70 (2014), pp. 116–123. ISSN: 09601481. DOI: 10.1016/j.renene.2014.01.002.
- [7] Majid Bastankhah and Fernando Porté-Agel. "Experimental and theoretical study of wind turbine wakes in yawed conditions". In: *Journal of Fluid Mechanics* 806 (2016), pp. 506–541. ISSN: 14697645. DOI: 10.1017/jfm.2016.595.
- [8] L. Battisti et al. "Aerodynamic measurements on a vertical axis wind turbine in a large scale wind tunnel". In: *Journal of Energy Resources Technology, Transactions of the ASME* 133.3 (2011), pp. 1–9. ISSN: 01950738. DOI: 10.1115/1.4004360.
- [9] Leonardo P. Chamorro and Fernando Porté-Agel. "Effects of Thermal Stability and Incoming Boundary-Layer Flow Characteristics on Wind-Turbine Wakes: A Wind-Tunnel Study". In: *Boundary-Layer Meteorology* 136.3 (2010), pp. 515–533. ISSN: 00068314. DOI: 10.1007/s10546-010-9512-1.
- [10] Gunner Chr et al. "Wake modeling and simulation". In: (2008).
- [11] Longhuan Du, Grant Ingram, and Robert G. Dominy. "A review of H-Darrieus wind turbine aerodynamic research". In: *Proceedings of the Institution of Mechanical Engineers, Part C: Journal of Mechanical Engineering Science* 233.23-24 (2019), pp. 7590–7616. ISSN: 20412983. DOI: 10.1177/0954406219885962.
- [12] Sten Frandsen. "On the wind speed reduction in the center of large clusters of wind turbines". In: *Journal of Wind Engineering and Industrial Aerodynamics* 39.1-3 (1992), pp. 251–265. ISSN: 01676105. DOI: 10.1016/0167-6105(92)90551-K.
- [13] Xiaoxia Gao et al. "Wind turbine layout optimization using multi-population genetic algorithm and a case study in Hong Kong offshore". In: *Journal of Wind Engineering and Industrial Aerodynamics* 139 (2015), pp. 89–99. ISSN: 01676105. DOI: 10.1016/j.jweia.2015.01.018.
- [14] Ananda Krishnan Gavin Kumar. "c 2012 by Gavin Kumar Ananda Krishnan. All rights reserved." In: (2012).
- [15] Seyed Hossein Hezaveh et al. "Increasing the Power Production of Vertical-Axis Wind-Turbine Farms Using Synergistic Clustering". In: *Boundary-Layer Meteorology* 169.2 (2018), pp. 275–296. ISSN: 15731472. DOI: 10.1007/s10546-018-0368-0. URL: <https://doi.org/10.1007/s10546-018-0368-0>.
- [16] Bo Hu. "Design of a Simple Wake Model for the Wind Farm Layout Optimization Considering the Wake Meandering Effect". In: (2016).

- [17] M. Huang et al. "Experimental Comparison of the Wake of a Vertical Axis Wind Turbine and Planar Actuator Surfaces". In: *Journal of Physics: Conference Series* 1618.5 (2020), pp. 0–10. ISSN: 17426596. DOI: 10.1088/1742-6596/1618/5/052063.
- [18] Focus O N Imaging. "FlowMaster". In: ().
- [19] Focus O N Imaging. "Imager sCMOS". In: ().
- [20] N O Jensen. "A note on wind generator interaction". In: *Risø-M-2411 Risø National Laboratory Roskilde* (1983), pp. 1–16. ISSN: 01676105. arXiv: arXiv:1011.1669v3. URL: <http://www.risoe.dk/rispubl/VEA/veapdf/ris-m-2411.pdf>.
- [21] Peter B V Johansson et al. "Equilibrium similarity, effects of initial conditions and local Reynolds number on the axisymmetric wake Equilibrium similarity, effects of initial conditions and local Reynolds number on the axisymmetric wake". In: 603.2003 (2015). DOI: 10.1063/1.1536976.
- [22] Hawwa Kadum et al. "Development and scaling of a vertical axis wind turbine wake". In: *Journal of Wind Engineering and Industrial Aerodynamics* 174. September 2017 (2018), pp. 303–311. ISSN: 01676105. DOI: 10.1016/j.jweia.2018.01.004.
- [23] I. Katic, J. Højstrup, and N.O. Jensen. "A Simple Model for Cluster Efficiency Publication date : Publisher ' s PDF , also known as Version of record Link to publication". In: *European wind energy association conference and exhibition 1* (1987).
- [24] Matthias Kinzel, Quinn Mulligan, and John O. Dabiri. "Energy exchange in an array of vertical-axis wind turbines". In: *Journal of Turbulence* 14.6 (2013), pp. 38–39. DOI: 10.1080/14685248.2013.825725.
- [25] Rob Kriegsman and Barry Reede. "Aerospace Engineering: The Open Jet Facility". In: (2016). URL: <http://www.lr.tudelft.nl/nl/organisatie/afdelingen/aerodynamics-wind-energy-flight-performance-and-propulsion/facilities/wind-tunnel-lab/open-jet-facility-hsl/>.
- [26] Kualo. "Global Wind Report Annual m ark et updat e 2012". In: (2012). URL: http://www.gwec.net/wp-content/uploads/2012/06/Annual%7B%5C_%7Dreport%7B%5C_%7D2012%7B%5C_%7DLowRes.pdf.
- [27] Qing'an Li et al. "Investigation of power performance and wake on a straight-bladed vertical axis wind turbine with field experiments". In: *Energy* 141 (2017), pp. 1113–1123. ISSN: 03605442. DOI: 10.1016/j.energy.2017.10.009. URL: <https://doi.org/10.1016/j.energy.2017.10.009>.
- [28] L. E.M. Lignarolo et al. "Experimental analysis of the wake of a horizontal-axis wind-turbine model". In: *Renewable Energy* 70 (2014), pp. 31–46. ISSN: 09601481. DOI: 10.1016/j.renene.2014.01.020. URL: <http://dx.doi.org/10.1016/j.renene.2014.01.020>.
- [29] P. B.S. Lissaman. "Energy Effectiveness of Arbitrary Arrays of Wind Turbines." In: *Journal of energy* 3.6 (1979), pp. 323–328. ISSN: 01460412. DOI: 10.2514/3.62441.
- [30] Grigorios Marmidis, Stavros Lazarou, and Eleftheria Pyrgioti. "Optimal placement of wind turbines in a wind park using Monte Carlo simulation". In: *Renewable Energy* 33.7 (2008), pp. 1455–1460. ISSN: 09601481. DOI: 10.1016/j.renene.2007.09.004.
- [31] Victor Mendoza et al. "Near-wake flow simulation of a vertical axis turbine using an actuator line model". In: *Wind Energy* 22.2 (2019), pp. 171–188. ISSN: 10991824. DOI: 10.1002/we.2277. URL: <https://doi.org/10.1002/we.2277>.
- [32] L D M Norante. "Advances and assessment 1.5mm of the Ring of Fire concept for on-site cycling aerodynamics". In: (2017).
- [33] Søren Ott, Jacob Berg, and Morten Nielsen. "Linearised CFD Models for Wakes". In: (2011).
- [34] Leonardo P Chamorro Fernando Porté-agel. "A Wind-Tunnel Investigation of Wind-Turbine Wakes : Boundary-Layer Turbulence Effects". In: (2009), pp. 129–149. DOI: 10.1007/s10546-009-9380-8.
- [35] General Remarks, Hardware Setup, and Parameter Configuration. "maxon motor control EPOS4 Gateway / CAN Configuration EPOS4 CAN Network with Gateway functionality EPOS4 Gateway / CAN Configuration". In: (2018), pp. 1–6.
- [36] Abdolrahim Rezaeiha et al. "Effect of the shaft on the aerodynamic performance of urban vertical axis wind turbines". In: *Energy Conversion and Management* 149. July (2017), pp. 616–630. ISSN:

01968904. DOI: 10.1016/j.enconman.2017.07.055. URL: <https://doi.org/10.1016/j.enconman.2017.07.055>.
- [37] Vincent F.C. Rolin and Fernando Porté-Agel. "Experimental investigation of vertical-axis wind-turbine wakes in boundary layer flow". In: *Renewable Energy* 118 (2018), pp. 1–13. ISSN: 18790682. DOI: 10.1016/j.renene.2017.10.105.
- [38] Sina Shamsoddin and Fernando Porté-Agel. "Large eddy simulation of vertical axis wind turbine wakes". In: *Energies* 7.2 (2014), pp. 890–912. ISSN: 19961073. DOI: 10.3390/en7020890.
- [39] Carlos Sim and Gijs Van Kuik. "Visualization by PIV of dynamic stall on a vertical axis wind turbine". In: *Experiments in Fluids* 46.1 (2009), pp. 97–108. ISSN: 07234864. DOI: 10.1007/s00348-008-0543-z.
- [40] Jens Nørkær Sørensen and Wen Zhong Shen. "Numerical modeling of wind turbine wakes". In: *Journal of Fluids Engineering, Transactions of the ASME* 124.2 (2002), pp. 393–399. ISSN: 00982202. DOI: 10.1115/1.1471361.
- [41] Richard J.A.M. Stevens and Charles Meneveau. *Flow Structure and Turbulence in Wind Farms*. Vol. 49. 2017, pp. 311–339. ISBN: 0108160602. DOI: 10.1146/annurev-fluid-010816-060206.
- [42] G. Tescione et al. "Near wake flow analysis of a vertical axis wind turbine by stereoscopic particle image velocimetry". In: *Renewable Energy* 70 (2014), pp. 47–61. ISSN: 09601481. DOI: 10.1016/j.renene.2014.02.042.
- [43] M. Tzimas and J. Prospathopoulos. "Wind turbine rotor simulation using the actuator disk and actuator line methods". In: *Journal of Physics: Conference Series* 753.3 (2016). ISSN: 17426596. DOI: 10.1088/1742-6596/753/3/032056.
- [44] R Veena et al. "Wake Induced Power Losses in Wind Farms". In: *International Journal of Engineering and Advanced Technology* 9.3 (2020), pp. 2175–2180. DOI: 10.35940/ijeat.c5611.029320.
- [45] L. J. Vermeer, J. N. Sørensen, and A. Crespo. "Wind turbine wake aerodynamics". In: *Progress in Aerospace Sciences* 39.6-7 (2003), pp. 467–510. ISSN: 03760421. DOI: 10.1016/S0376-0421(03)00078-2.
- [46] PEJ Vermeulen. "An experimental analysis of wind turbine wakes". In: *3rd International Symposium on Wind Energy Systems* BHR Fluid Engineering, Lyngby, Denmark.3 (1980), pp. 50–431.
- [47] Christopher R. Vogel and Richard H.J. Willden. "Investigation of wind turbine wake superposition models using Reynolds-averaged Navier-Stokes simulations". In: *Wind Energy* 23.3 (2020), pp. 593–607. ISSN: 10991824. DOI: 10.1002/we.2444. URL: <https://doi.org/10.1002/we.2444>.
- [48] "Wind speed deficit, Introduction to Wind Turbines: Physics and Technology (AE4W02TU), TU DELFT". In: (), pp. 1–3.
- [49] *Wind-Turbine and Wind-Farm Flows: A Review*. Vol. 174. 1. Springer Netherlands, 2020, pp. 1–59. ISBN: 1054601900473. DOI: 10.1007/s10546-019-00473-0. URL: <https://doi.org/10.1007/s10546-019-00473-0>.
- [50] Yu-ting Wu and Fernando Porté-Agel. "Atmospheric Turbulence Effects on Wind-Turbine Wakes: An LES Study". In: (2012), pp. 5340–5362. DOI: 10.3390/en5125340.
- [51] Gao Xiaoxia, Yang Hongxing, and Lu Lin. "Optimization of wind turbine layout position in a wind farm using a newly-developed two-dimensional wake model". In: *Applied Energy* 174. July 2016 (2017), pp. 192–200. ISSN: 0306-2619. DOI: 10.1016/j.apenergy.2016.04.098. URL: <http://dx.doi.org/10.1016/j.apenergy.2016.04.098>.



Appendix-A

A.1. Wake superposition Methods

Wake superposition, where the wind profile and wake deficit behind a single wind turbine can be combined with a superposition method. There are different superposition methods proposed in literature to calculate the wind profile at a wind turbine, influenced by multiple wakes. Based on the free stream velocity and wind speed used to calculate the individual wakes and the approaches adopted to combine the wakes either by summing the wake velocity deficits, or summing the squares of the wake velocity deficits, the literature presents with four wake superposition methods [41] [49], as follows.

A.1.1. Simple Empirical Wake Superposition Methods

Lissaman [29] considered a large wind turbine spacing with weak wake interaction and assumed, that the inflow velocity of the wind farm ($u_0^i \approx U_\infty$). Further the wake velocity deficit term is small, the momentum deficit is $(U_\infty - u_s^i)$. u_s^i can be approx to $U_\infty \cdot u_w^i$. Therefore, to conserve the total momentum in the deficits of the wake, the deficits are summed up linearly to give:

$$U_w(x, y, z) = U_\infty - \sum_i (U_\infty - u_w^i(x, y, z)) \quad (\text{A.1})$$

Katic, Højstrup & Jensen [20] also made a similar assumption of $u_0^i \approx U_\infty$ for the calculation for individual wakes, where the wake superposition is realized by summing the squares of the wake velocity deficits. Where the mean kinetic energy deficit for the total wake interaction is conserved, which is disagreeable as mean kinetic energy is not really conserved due to some significant turbulent dissipation. this is given by the following expression:

$$U_w(x, y, z) = U_\infty - \sqrt{\sum_i (U_\infty - u_w^i(x, y, z))^2} \quad (\text{A.2})$$

The equation A.3 and A.4 were proposed as counter-parts of A.1 and A.2 by Niayifar & Porté-Agel [7] and Voutsinas, Rados & Zervos [43] respectively. In these two equations, similar operations of linear sum and square sum are accepted to combine the individual wake velocity deficits. But a change is made where the approximation of $u_0^i \approx U_\infty$ is removed, and the mean wind velocity recognised by the wind turbines is u_0^i , where ($i = 0, 1, 2, 3, \dots$) from upstream turbine to downstream ones. Therefore equations A.3, A.4 will give a more accurate results than their counterparts.

$$U_w(x, y, z) = U_\infty - \sum_i (U_0^i - u_w^i(x, y, z)) \quad (\text{A.3})$$

$$U_w(x, y, z) = U_\infty - \sqrt{\sum_i (U_0^i - u_w^i(x, y, z))^2} \quad (\text{A.4})$$

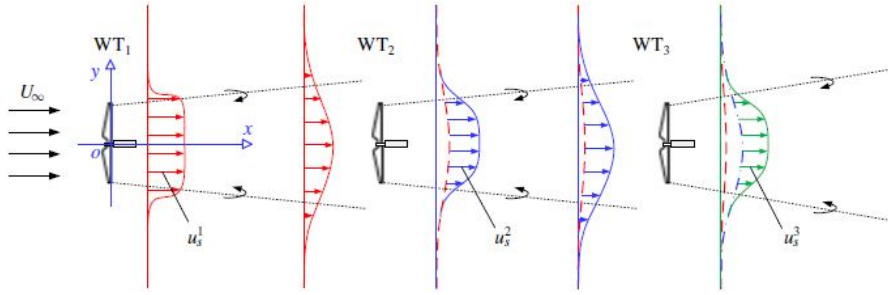


Figure A.1: Wake superposition for three inline wind turbines[49]

where the figure A.1, u_0^i is the mean wind velocity received by the rotor of the i^{th} turbine, u_w^i is the wake induced by the i^{th} turbine in a stand alone conditions. $u_s^i = u_0^i - u_w^i$ (individual wake deficit) is given by the difference between the wind velocity at the rotor of i^{th} turbine and the wake velocity. To, summarize, all the above wake superposition methods are all empirical relations without a solid theoretical foundation. When the individual wakes are combined, they are highly unlikely to conserve the total momentum deficit. Hence a new novel wake superposition method by [] is studied further, it is derived specifically from law of conservation of momentum and has shown high reliability when compared against existing above methods, experimental data and large-eddy simulations (LES data).

A.1.2. Theoretical Wake Superposition Method based on Law of Conservation of Momentum

For the wake flow, the law of conservation of momentum states that the total momentum deficit flow across the wake cross-section has to be conserved, which will be equal to total amount of drag force imposed by the flow.

A mean convection velocity (u_c^i) is used here, to represent the spatial dependency of wake velocity in the entire wake cross-section region. Also, it is important to linearize the momentum deficit, is a weighted average of the wake velocity: were the selected weights are based on corresponding wake velocity deficits.

$$u_c^i(x) = \frac{\iint u_w^i(x, y, z) dy dz}{\iint u_s^i(x, y, z) dy dz} \quad (\text{A.5})$$

For the wake superposition, a single isolated wake model need to be considered, which is also derived strictly from law of conservation of momentum, to archive the expression for u_c^i and give more precise results. Therefore, Bastankhah & Porté-Agel [6] is chosen also it fits well with our motive. Substituting 2.27 in to the above expression A.5 the mean convection velocity is obtained:

$$\frac{u_c^i(x)}{u_0^i} = \frac{1}{2} + \frac{1}{2} \sqrt{1 - \frac{C_t^i}{8\sigma_y\sigma_z/D}} \quad (\text{A.6})$$

Here, the mean convection velocity is between limits $0.5u_0^i$ and u_0^i , increasing with wake width and decreasing with the thrust coefficient. to conserve the total momentum deficit during a wake superposition, the combined wake velocity U_w , where as U_s is the total wake velocity deficit given by $(U_\infty - U_w)$. similar to equation A.5 a mean conservation velocity for the combined wake (U_c) can be defined:

$$U_c(x) = \frac{\iint U_w(x, y, z) \cdot U_s(x, y, z) dy dz}{\iint U_s(x, y, z) dy dz} \quad (\text{A.7})$$

$$\iint U_s(x, y, z) dy dz = \sum_i \frac{u_c^i(x)}{U_c(x)} \iint U_s^i(x, y, z) dy dz \quad (\text{A.8})$$

from the above equation a single equation is introduced for the total wake velocity deficit.

$$U_s(x, y, z) = \sum_i \frac{u_c^i(x)}{U_c(x)} \cdot U_s^i \quad (\text{A.9})$$

The equation above A.9 states that the total wake velocity deficit equals a weighted sum of the individual wake velocity deficits, where the weights are determined by the ratio of u_c^i to U_c . Since the mean convection velocity for the combined wake is unknown before the wake superposition, an iterative method is to be carried out to solve the combined wake velocity. To be precise, U_c is logged in to be the maximum value of u_c^i and substituted into A.9 to get an estimated total wake velocity deficit. The estimated total wake velocity deficit is further put into A.7 to get a corrected convection velocity for the combined wake U_c . This iterative process repeats, until a certain accuracy is achieved.

A.2. Determination of the Synchronisation System Delay

In the section 3.6.3 the implementation of a synchronisation system between the image acquisition and the rotor movement over the trigger sensor for phase lock measurement was discussed. The aim of the synchronisation system is to ensure a similar relative location between the rotor position and the acquired wakes, when comparing different cases during the experiment campaign. As stated in the above mentioned section the mode 1 has a fallacy in locating the initial position of the rotor. So here a subsequent experiment campaign was conducted in order to locate and predict the initial position of the rotor in different conditions. Also a mode 2 was developed from this experimental campaign where the system delay was recognised and used to pin point the accurate location of rotor at various RPM and angular positions of the rotor.

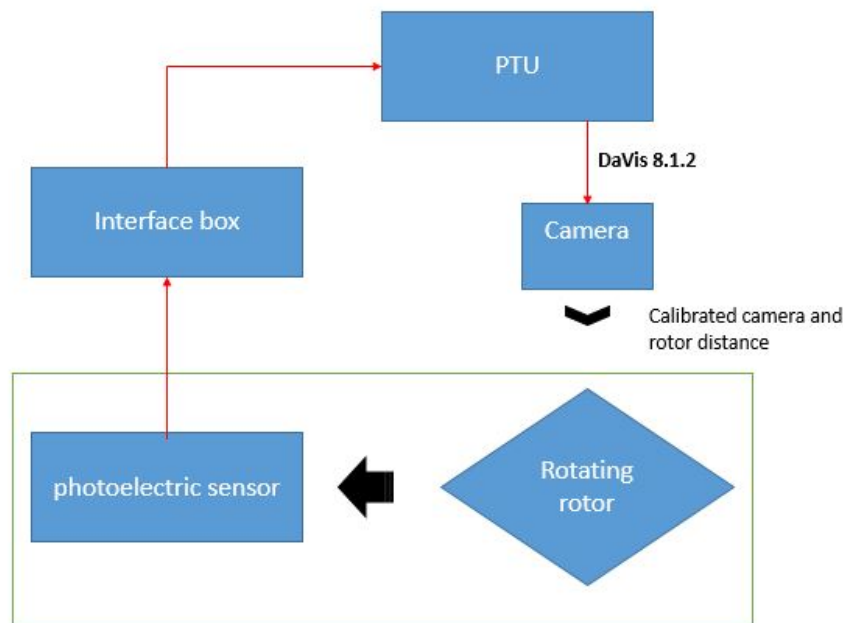


Figure A.2: Experiment setup schematic

For the synchronisation of the system a schematics in figure A.2 was used, and the actual setup can be viewed in figure A.3. Here a photoelectric sensor was used as a trigger mechanism, which was triggered using a small thin light weight disk with an attached magnetic sensor. Given the photo detector delay being lower than 0.2 ms. This potentiality could be spoiled by a non-constant initial delay of the triggering system, hence it was of the prime importance to calculate this time delay precise and then added to the Davis system. At a fixed position of the rotor during every rotation a signal from the

photoelectric sensor is passed to the interface box. The interface box is connected to the trigger input port of the PTU (Programmable Timing Unit) through a trigger connection. where in the Davis software the following commands are specified: trigger mode to be external cyclic, the camera recording rate is automatically adjusted to 13.323 Hz and the exposure to clearly observe the image we set to be 1000 μ s. The rotor was dismantled and a empty cup holder was attached with a 360 degree protractor and this was fixed to the outer non rotating part of the shaft. the rotating shaft was fixed with an another thin fiber disk and a marking arrow was made over this disk. The camera (specifications yet to be written) was aligned accurately 90 degrees over this turbine without the shaft. This was done using a setup made from X beams and position holders, the alignment and correct positioning was done using a spirit level instrument.

The working for this campaign to find the accurate system delay was as follows: A set position of 0 degrees was aligned with the photo sensor and the rotating disk marker on the shaft. Signal passed by the photoelectric sensor was recorded by the PTU, further used by the Davis system to capture a set of images (eg: 10 images in this case), now the rotating part of the shaft and the disk marker on it would act as the position marker for the images taken and the stationary protractor with the cup holder would measure the delay in angle for different RPM. As we have aligned the rotating disk marker and the photoelectric sensor at zero degree position the delay in degrees for different RPM can be found easily. The table A.1 below shows a delay in degrees for RPM 10, 300, 600 and 800 as the RPM increases the rotation speed increases and the delay angle also increases for the camera acquisition system. Here the rotation speed of the rotor is constant and hence the time required for rotation per degree is also constant which can be easily calculated for different RPM. The image acquired by the camera records the delay in angle and this can then be converted into time further, this time delay can be added to the Davis system to accurately capture the image at a particular position. ex: for the original test conditions the phases lock measurements are to be conducted at 800 rpm see table A.1 the delay measured by the camera acquisition system is found to be 45 degrees. Time required by the rotor to complete one degree is 0.00020833 sec, hence to capture the data at correctly zero degrees the following equation is used:

$$[System_{delay}(s) = (360 - delay)degrees \times time_{1degree}(s)] \quad (A.10)$$

which gives a time delay to be added in David as 0.065625 sec. The table A.1 shows the calculated time delay to be added in μ s for different degrees and various RPM.

		Phase angle						
RPM	Delay angle [deg]	RPS	DPS	second per degree	t [μ s]	t [μ s]	t [μ s]	t [μ s]
10	0	0.166666667	60	0.016666667	6000000	750000	1500000	2250000
300	15	5	1800	0.000555556	191666.7	16666.67	41666.67	66666.67
600	35	10	3600	0.000277778	90277.78	2777.778	15277.78	27777.78
800	45	13.33333333	4800	0.000208333	65625	0	9375	18750

Table A.1: Phase lock system time delay measurements

A.3. Experiment Planned Cases

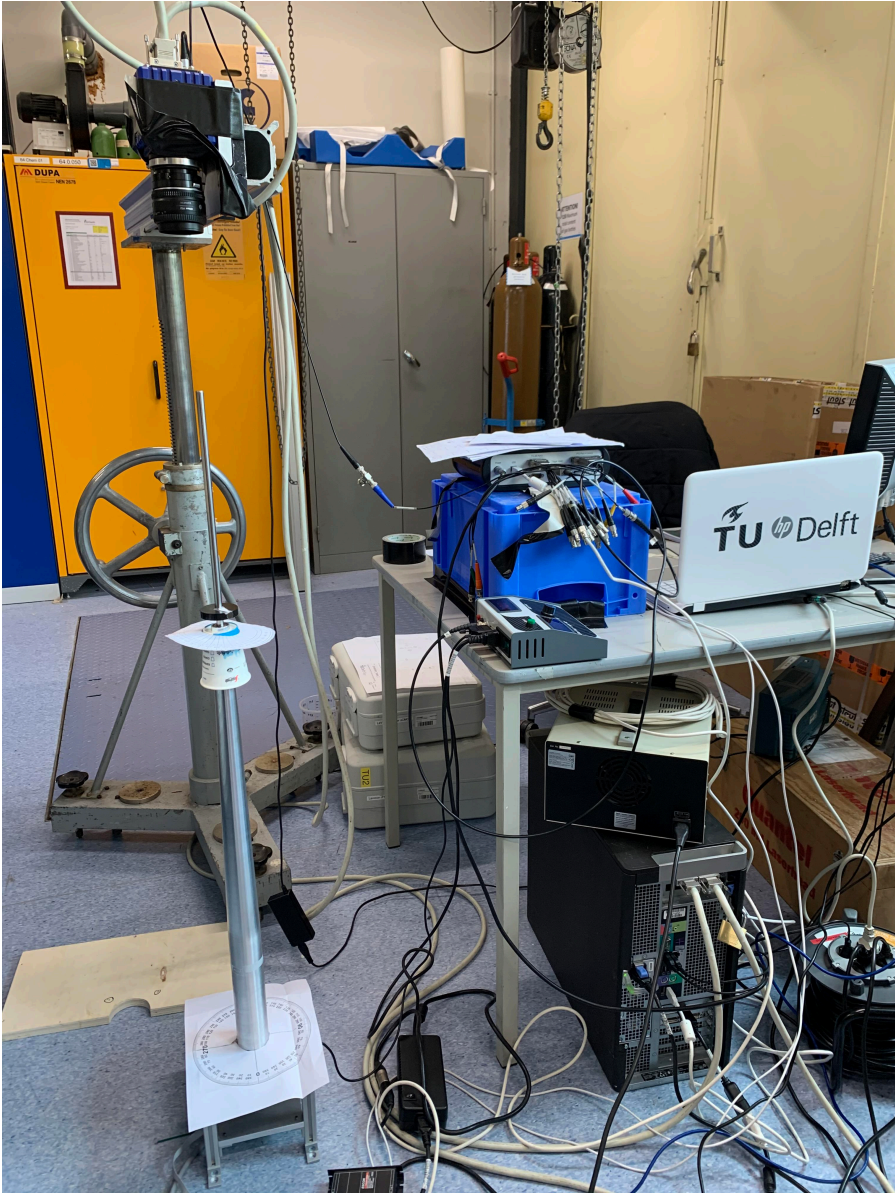


Figure A.3: Experiment setup for phase lock

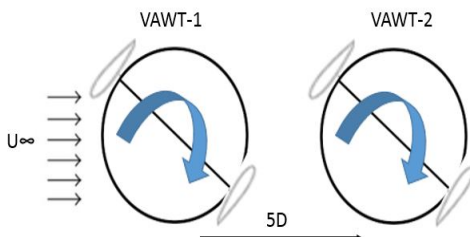
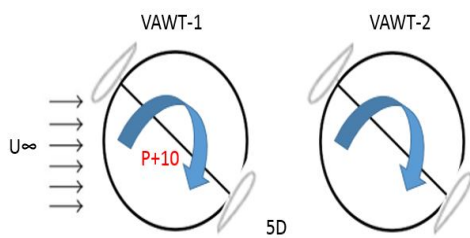
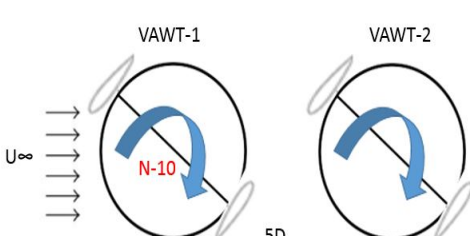
Case description		
Case no	Case	Description
Phase lock 1 (Both the rotor inline, zero angle of deflection on both)	<ul style="list-style-type: none"> • $x/D = 4.4$ w.r.t rotor 1 • $x/D = 5.06$ w.r.t rotor 1 • $x/D = 5.5$ w.r.t rotor 	Phase lock measurements were achieved at particular fixed rotation phase of rotor (0, 45, 90, 135 degrees of rotation) at three different downwind planes (x/D)
Phase lock 2 (Both the rotor inline, positive angle of deflection on rotor 1)	<ul style="list-style-type: none"> • $x/D = 4.4$ w.r.t rotor 1 • $x/D = 5.06$ w.r.t rotor 1 • $x/D = 5.5$ w.r.t rotor 1 	Phase lock measurements were achieved at particular fixed rotation phase of rotor (0, 45, 90, 135 degrees of rotation) at three different downwind planes (x/D)
4		Inline Base Case: Two rotor's with straight blades (Zero angle deflection on blades) and inline, Wake measurement till $10 x/D$
5		Inline two rotor Case (+P10): Two rotor inline with blades deflected to a positive 10 degree angle on rotor 1 and zero deflection on rotor 2, Wake measurement till $10 x/D$
6		Inline two rotor Case (-N10): Two rotor's inline with blades deflected to a negative 10 degree angle on rotor 1 and zero deflection on rotor 2, Wake measurement till $10 x/D$

Table A.2: Case description

Case description		
Case no	Case	Description
7		<p>Offset Base Case: Two rotor's with straight blades (Zero angle deflection on blades) and Rotor 2 offset from rotor 1 by $1(x/D)$, Wake measurement till $10 x/D$</p>
8		<p>Offset two rotor Case (+P10): Two rotor's with blades deflected to a positive 10 degree angle on rotor 1 and zero deflection on rotor 2 and Rotor 2 offset from rotor 1 by $1(x/D)$, Wake measurement till $10 x/D$</p>
9		<p>Offset two rotor Case (-N10): Two rotor's with blades deflected to a negative 10 degree angle on rotor 1 and zero deflection on rotor 2 and Rotor 2 offset from rotor 1 by $1(x/D)$, Wake measurement till $10 x/D$</p>
10		<p>Superposition Case: The free stream wind velocity (3.84) is adjusted according to the thrust force experienced by the second turbine in inline base case (4) and similar condition are achieved to understand the wake superposition.</p>

Table A.3: Case description

A.4. Force measurement by Force Balance System for Pitch Angle Case

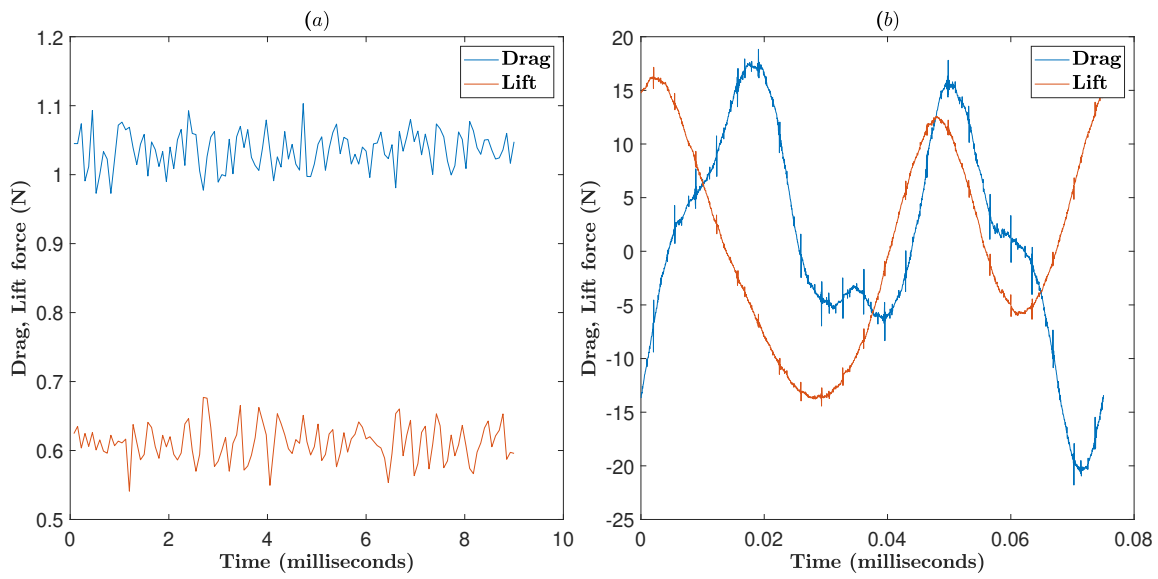


Figure A.4: Force measurements for positive pitch case

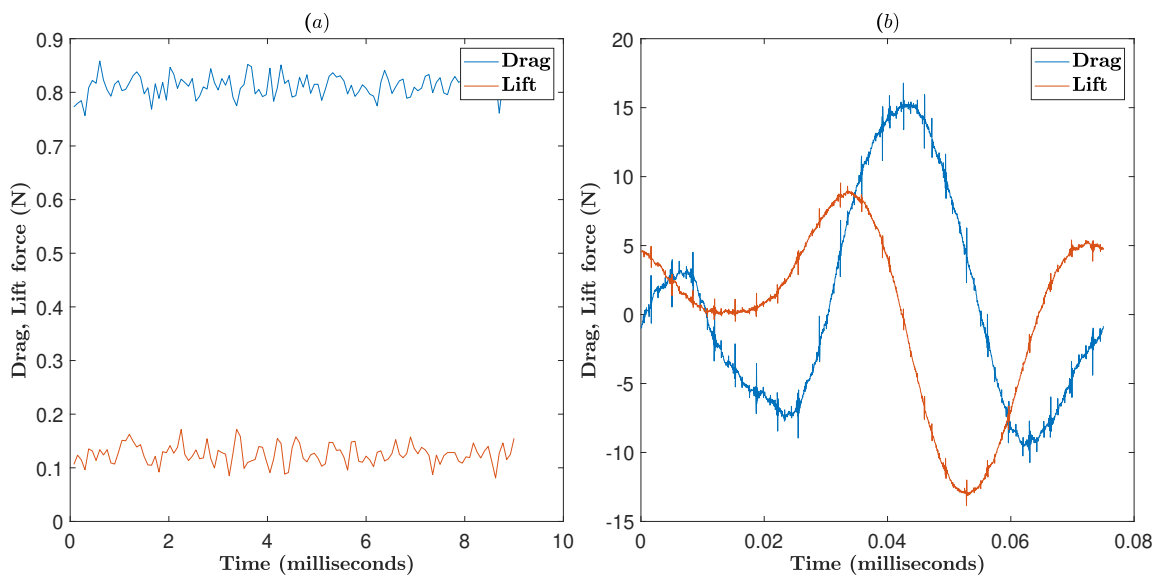


Figure A.5: Force measurements for negative pitch case

A.5. VAWT Cover Specifications

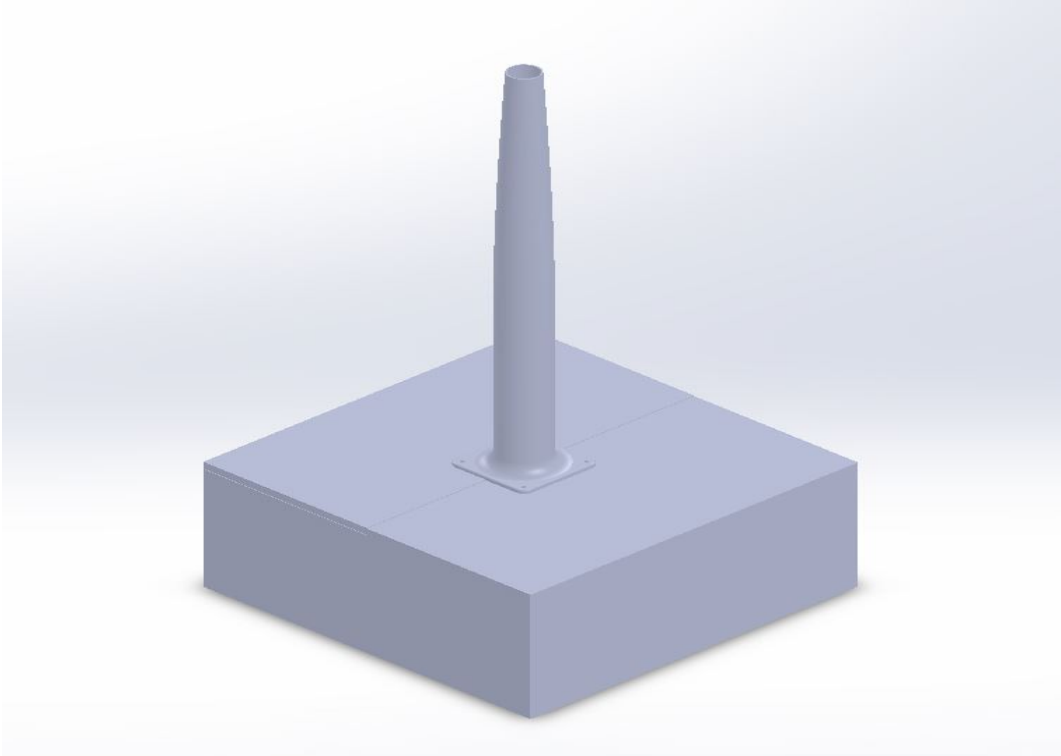


Figure A.6: VAWT cover Specifications

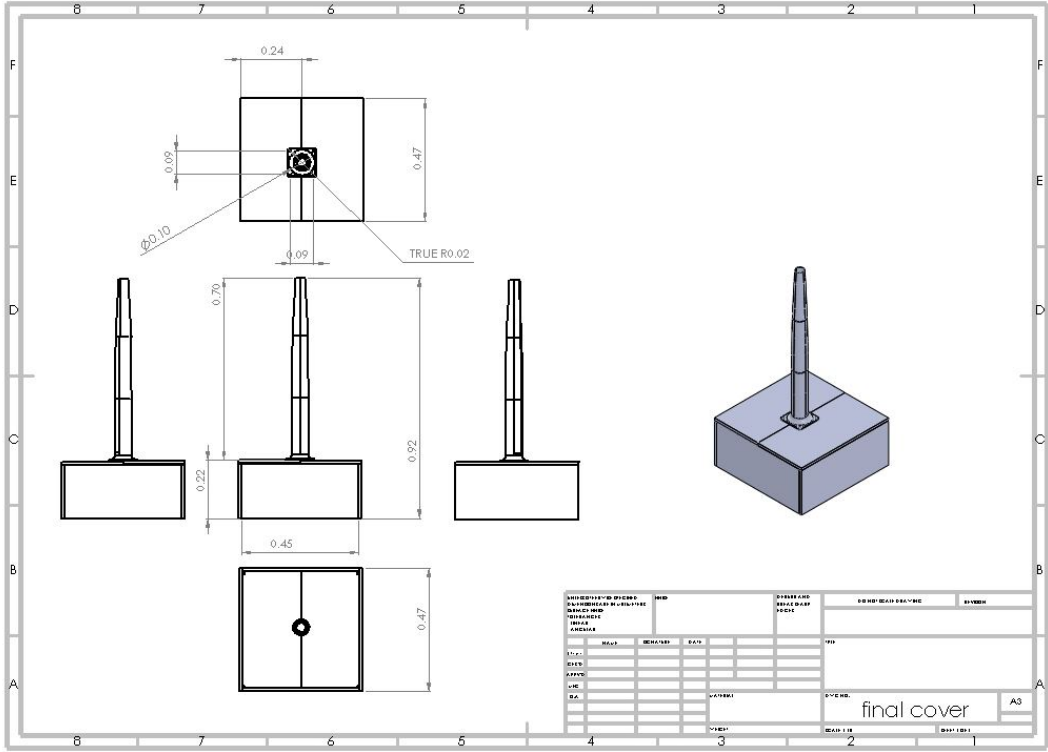


Figure A.7: VAWT cover Specifications

A.6. Blue Table Attachment Specifications

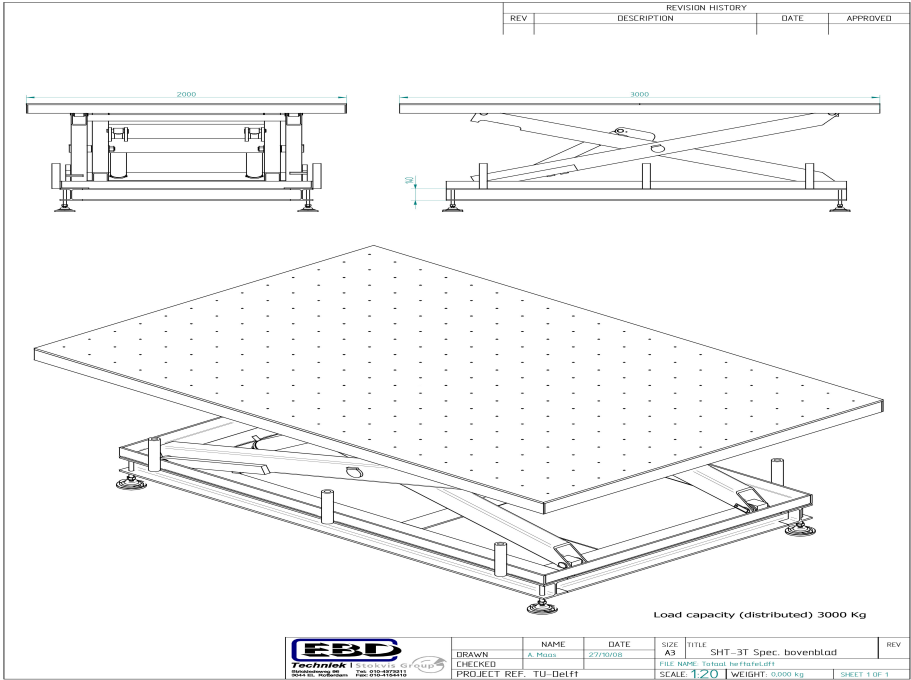


Figure A.8: Blue table specifications

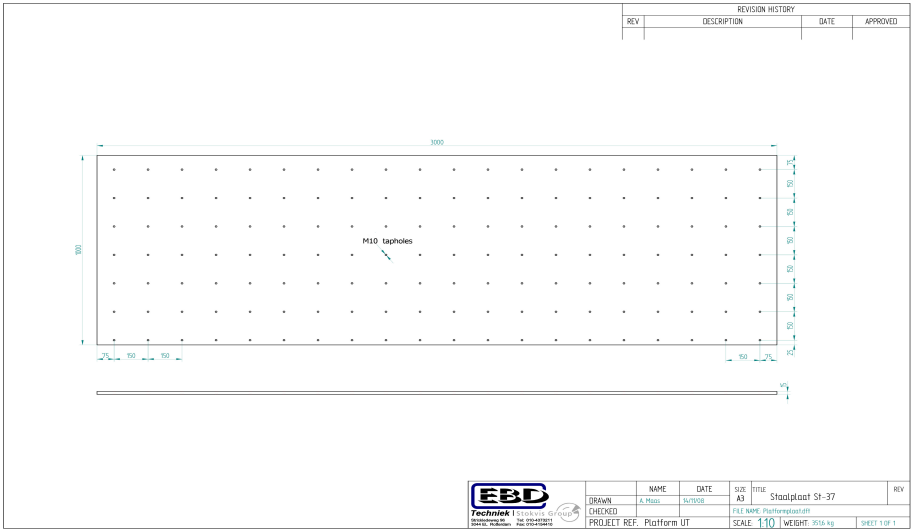


Figure A.9: Blue table specifications

A.7. Guidance for Transverse System

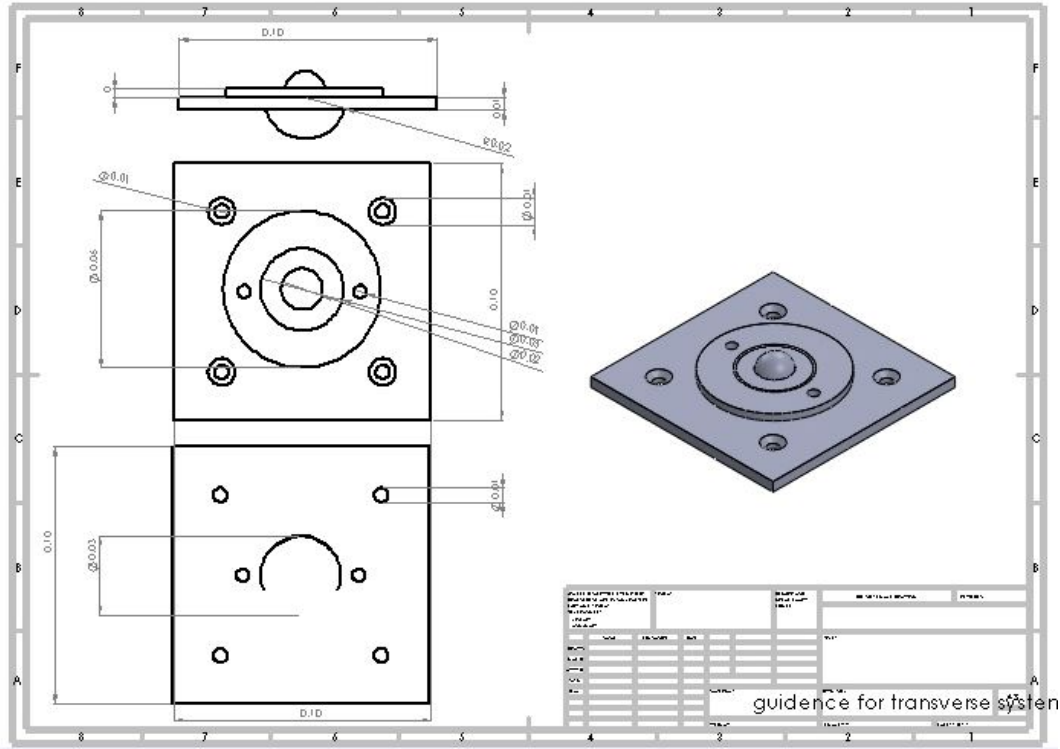


Figure A.10: Guidance for Transverse System

महादेव सर्वाचं भलं करो.....

All hail lord mahadev....